








Review

A Review of the MSCA ITN ECOSTORE—Novel Complex Metal Hydrides for Efficient and Compact Storage of Renewable Energy as Hydrogen and Electricity

Efi Hadjixenophontos ^{1,2}, Erika Michela Dematteis ^{3,4}, Nicola Berti ^{3,4}, Anna Roza Wołczyk ⁴, Priscilla Huen ^{5,6}, Matteo Brighi ⁷, Thi Thu Le ⁸, Antonio Santoru ⁸, SeyedHosein Payandeh ^{5,9}, Filippo Peru ¹⁰, Anh Ha Dao ^{3,11,12}, Yinzhe Liu ^{13,14} and Michael Heere ^{15,16,*}

- ¹ Institut für Materialwissenschaft, Lehrstuhl Materialphysik (IMW), University of Stuttgart, Heisenbergstrasse 3, 70569 Stuttgart, Germany; Efi.Hadjixenophontos@dlr.de
 - ² High Temperature Systems and Process Development, German Aerospace Center Stuttgart (DLR), Pfaffenwaldring 38–40, 70569 Stuttgart, Germany
 - ³ Institut de Chimie et des Matériaux Paris Est, ICMPE, CNRS-UPEC, F-94320 Thiais, France; erika.dematteis@gmail.com (E.M.D.); nicola.berti.86@gmail.com (N.B.); DAOHAANH1988@gmail.com (A.H.D.)
 - ⁴ Chemistry Department and NIS, University of Turin, Via Pietro Giuria, 7, 10125 Torino, Italy; aniaw4@o2.pl
 - ⁵ Interdisciplinary Nanoscience Center (iNANO) and Department of Chemistry, University of Aarhus, Langelandsgade 140, DK-8000 Aarhus C, Denmark; priscillahuen@yahoo.com.hk (P.H.); Seyedhosein.Payandeh@empa.ch (S.P.)
 - ⁶ Department of Physics, Chemistry and Pharmacy, University of Southern Denmark, Campusvej 55, 5230 Odense M, Denmark
 - ⁷ Department of Quantum Matter Physics, Laboratory of Crystallography, University of Geneva, Quai Ernest-Ansermet 24, CH-1211 Geneva, Switzerland; Matteo.Brighi@unige.ch
 - ⁸ Nanotechnology Department, Helmholtz-Zentrum Geesthacht, 21502 Geesthacht, Germany; Thi.Le@hzg.de (T.T.L.); antonio4.santoru@gmail.com (A.S.)
 - ⁹ Empa, Swiss Federal Laboratories for Materials Science and Technology, 8600 Dübendorf, Switzerland
 - ¹⁰ Institute of Nanoscience and Nanotechnology, NCSR “Demokritos”, Ag. Paraskevi Attikis, 15341 Athens, Greece; filippoperu@gmail.com
 - ¹¹ Prospective Research Group—Saft Batteries, 33300 Bordeaux, France
 - ¹² Warwick Manufacturing Group, University of Warwick, Coventry CV4 7AL, UK
 - ¹³ School of Metallurgy and Materials, University of Birmingham, Birmingham B15 2TT, UK; yinzhe-liu@geidco.org
 - ¹⁴ Global Energy Interconnection Group Company Limited, Beijing 100031, China
 - ¹⁵ Department for Neutron Materials Characterization, Institute for Energy Technology, NO-2027 Kjeller, Norway
 - ¹⁶ Institute for Applied Materials – Energy Storage Systems (IAM-ESS), Karlsruhe Institute of Technology (KIT), Hermann-von-Helmholtz-Platz 1, 76344 Eggenstein-Leopoldshafen, Germany
- * Correspondence: michael.heere@kit.edu

Received: 4 December 2019; Accepted: 18 February 2020; Published: 2 March 2020



Abstract: Hydrogen as an energy carrier is very versatile in energy storage applications. Developments in novel, sustainable technologies towards a CO₂-free society are needed and the exploration of all-solid-state batteries (ASSBs) as well as solid-state hydrogen storage applications based on metal hydrides can provide solutions for such technologies. However, there are still many technical challenges for both hydrogen storage material and ASSBs related to designing low-cost materials with low-environmental impact. The current materials considered for all-solid-state batteries should have high conductivities for Na⁺, Mg²⁺ and Ca²⁺, while Al³⁺-based compounds are often marginalised due to the lack of suitable electrode and electrolyte materials. In hydrogen storage materials, the

sluggish kinetic behaviour of solid-state hydride materials is one of the key constraints that limit their practical uses. Therefore, it is necessary to overcome the kinetic issues of hydride materials before discussing and considering them on the system level. This review summarizes the achievements of the Marie Skłodowska-Curie Actions (MSCA) innovative training network (ITN) ECOSTORE, the aim of which was the investigation of different aspects of (complex) metal hydride materials. Advances in battery and hydrogen storage materials for the efficient and compact storage of renewable energy production are discussed.

Keywords: lithium ion conductor; anode materials; metal hydrides; solid-state conductors; solid-state electrolyte; Na-based *closo*-borates; all-solid-state batteries; beyond Li-ion; post Li-ion; hydrogen storage; amides; imides; eutectic borohydride; reactive hydride composites; rare earth; borohydrides; kinetics tailoring; Ti-based catalyst; nanoconfinement

Table of Content

1. Introduction	3
2. Promising Metal Hydrides for Battery Application	4
2.1. Metal Hydrides for Li-ion and Post Li Batteries	4
2.1.1. Metal Hydrides as Negative Electrode Material with Liquid Electrolyte	5
2.1.2. Promising Complex Metal Hydrides as Solid-State Electrolytes	8
Lithium Borohydride	9
Lithium Nitride and Lithium Hydride	9
Binary Phases of Hydrides with Lithium Halides	11
LiBH ₄ -Li ₂ NH: Li ₅ (BH ₄) ₃ NH—thorough characterization of a cluster complex hydride	11
Argyrodite Structure Materials	12
2.1.3. Application of Metal Hydrides in Solid-State Cells	13
Solid-State Half-Cell	13
A Full Solid-State Li-ion Cell	15
2.1.4. Conclusions	15
2.2. Na-Based <i>Closo</i>-Borates for Na Batteries	16
2.2.1. Na-Based <i>Closo</i> -Borates Solid Electrolyte	16
The Na ₂ B ₁₂ H ₁₂ Polymorphism	16
Na _{x+2y} (CB ₁₁ H ₁₂) _x (B ₁₂ H ₁₂) _y Solid Electrolyte	17
2.2.2. Conclusions	20
3. Advances in Hydrogen Storage Materials	20
3.1. Pure Metal Hydrides (Mg, Pd, Ti)	21
3.2. Amide and Imide Based Systems for H₂ Storage	22
3.2.1. Insights into Alkali-Based Amides and Imides Including Boron	23
LiBH ₄ -LiNH ₂	23
LiNH ₂ -Li ₂ NH	25
3.2.2. Insights into the Structure and Reaction Mechanism of Metal Amide—Metal Hydride Composite Systems	25
Ammonolysis of Alkali and Alkaline-Earth Metal Amides	26
K-Mg-N-H System	26
KNH ₂ -KH System	27
Rb-Mg-N-H and Rb-N-H Systems	27
3.2.3. Conclusions	27

3.3. Eutectic Metal Borohydride Systems	28
3.3.1. Experimental Study and Assessment of Eutectic Borohydride Systems	29
LiBH ₄ -NaBH ₄	29
LiBH ₄ -KBH ₄	30
NaBH ₄ -KBH ₄	30
LiBH ₄ -NaBH ₄ -KBH ₄	30
Other Systems	31
3.3.2. Thermodynamic Properties of Eutectic Borohydride Systems	31
3.3.3. Hydrogen Storage Properties of Eutectic Metal Borohydride Systems	33
3.3.4. Conclusions	33
3.4. Kinetic Tailoring of 2LiBH₄ + MgH₂/2LiH + MgB₂ with Cost Effective 3TiCl₃·AlCl₃	34
3.5. Role of Nanoconfinement in Enhancing the Properties of Hydrogen Storage Materials	39
3.5.1. Nanoconfinement Approaches	40
3.5.2. Confined Borohydrides	41
3.5.3. Conclusions	43
3.6. Rare Earth Borohydrides	43
3.6.1. Synthesis of Rare Earth Borohydrides (<i>REB</i>)	44
Solvent Free Synthesis of <i>REB</i>	44
Solvent-Based Synthesis of <i>REB</i>	44
3.6.2. Crystal Structures of Monometallic <i>REB</i>	45
3.6.3. Crystal Structures of Bimetallic <i>REB</i>	46
3.6.4. Reactive Hydride Composites with <i>REB</i>	49
3.6.5. Conclusions	51
4. Final Conclusion and Outlook	51
References	53

1. Introduction

The development of materials for energy storage applications is one of the great challenges of our generation. To reduce the carbon footprint and to extend the use of renewable energy sources, it is necessary to store energy for times of great demand. Over recent years, energy production from renewables has increased worldwide. This results in a demand for sustainable energy storage systems for intermittent sources.

Metal hydrides, or in general, the energy carrier hydrogen, are ideal for sustainable storage systems and current products already show their potential in practical applications. Implementations can be found in the form of metal hydride as chemical energy storage in the case of power and heat distribution of the Henn-Na hotel in Japan (H2one from Toshiba), as well as in the 700-bar hydrogen storage tanks of several electric vehicles, such as the Toyota Mirai, Honda Clarity or Hyundai Nexa [1]. An electrochemical storage character is applied already in nickel-metal hydride batteries (Ni-MH), with over 1 billion cells sold in 2015 (vs. 6 billion lithium (Li) ion battery cells) [2]. Furthermore, a recent study suggests implementing metal hydrides as a thermal battery for concentrated solar power plants [3].

Nonetheless, not only efficient and compact storage of renewable energy are needed for the future. As the energy consumption as well as performance of portable electronic devices, such as laptops, cameras and smartphones have tremendously increased over the past decades, high-energy-density power supply systems are also required. In this context, a vast amount of research is still being conducted to improve electrochemical systems such as the Li-ion battery. Further efforts concentrate on so-called “post Li-batteries” which describe materials for all-solid-state Li-ion batteries, or even batteries with alternative working ions including sodium (Na⁺), magnesium (Mg²⁺) and calcium (Ca²⁺), while aluminium (Al³⁺)-based compounds are not considered due to the unavailability of suitable electrode and electrolyte materials [4–6].

The aforementioned materials are considered as cheaper and more abundant. With respect to multivalent ions, higher energy densities are potentially achievable compared to current state-of-the-art

technology. Nevertheless, transport properties of larger ions are challenging and directly correlated to the underlying crystal structure. Understanding the associated structural as well as dynamic changes during ion insertion and ion extraction is crucial for the improvement of the electrode materials for “post Li-batteries”.

This review focusses on eight major points of interest, starting from describing the use of metal and complex hydrides for secondary batteries including Li-ion, post Li and all-solid-state batteries based on Li. Half and full-cell performance are introduced at the end of the Section 2.1. Section 2.2. turns the focus on the electrochemical performance of *closo*-borates, an interesting class of complex hydrides in Na-based batteries. Moving from batteries to hydrogen storage in metals, Section 3.1 examines the latest reports on pure metal hydrides while concentrating on one of the most promising metals, magnesium. In Section 3.2, the chemically bounded storage of hydrogen is discussed with an emphasis on amide-based systems. Section 3.3 draws attention to the eutectic metal borohydride systems that show interesting behaviour while Section 3.4 presents the kinetic tailoring of LiBH_4 with effective additives. In Section 3.5, the authors consider the role of nanoconfinement in enhancing hydrogen storage capacities, while in Section 3.6, the synthesis and performance of rare earth borohydrides (monometallic, bimetallic and composites) are presented. The table of content presented hereafter gives further details on the sub-chapters and each chapter ends with a short conclusion on the key achievements on the progress of hydrogen used as a versatile energy storage material.

2. Promising Metal Hydrides for Battery Application

2.1. Metal Hydrides for Li-ion and Post Li Batteries

Secondary lithium-ion batteries (LiBs), as a feasible solution for energy storage of intermittent energy production, are currently one of the most effective battery systems [7]. With high performance, LiB systems exhibit an impressive energy density up to 210 Wh kg^{-1} (650 Wh L^{-1}) compared to other battery technologies and take a vital role in markets as the most attractive electrical energy storage system [8]. Since their commercialisation by Sony in 1991 [9], significant progress has been achieved in increasing the performance of LiBs by using new cathodes. The latter were first based on lithium iron phosphate (LiFePO_4), while nanostructuring and nanoconfinement also played a role in increasing performance. Nowadays, nickel-rich layered cathode materials are a focus for automotive applications [10–15]. For the anode, a material with higher capacity is still under investigation as a replacement for commercial graphite whose capacity only reaches 375 mAh g^{-1} (840 Ah L^{-1}). Metal hydrides have recently been proposed as a potential candidate for anode replacement in LiBs due to their high intrinsic specific energy capacity; i.e., up to 2038 mAh g^{-1} for MgH_2 and 1074 mAh g^{-1} for TiH_2 [16,17]. Through a conversion reaction with lithium, metal hydrides are evidenced to possess remarkable properties compared to other conversion materials, such as low reaction potential, small hysteresis and high theoretical capacity.

Safety is another important request for LiBs. The concept of all-solid-state lithium-ion-batteries (ASS-LiBs) has been developed to solve vital drawbacks of conventional LiBs with liquid electrolyte. These challenges include electrolyte leakage, the narrow range of temperature operation, causing the evaporation of the solvent at higher temperatures, decomposition of the liquid electrolyte at the electrodes surface to form a solid electrolyte interphase (SEI), and expansion and explosion of the solvent upon heating. The solid electrolyte reduces the associated explosion risks and it facilitates the manufacture process, allowing smaller cells with a higher specific energy capacity and preserving contact between components [18,19]. The main challenge is to find a lithium ionic conductor with sufficient ionic conductivity (at least $10^{-4} \text{ S cm}^{-1}$ under working conditions), low electronic conductivity ($<10^{-10} \text{ S cm}^{-1}$), and good electrochemical stability. It should also be compatible with lithium and electrode materials and have low weight density. Complex metal hydrides, such as LiBH_4 , LiNH_2 and their combinations with other compounds, e.g., LiX (where X is a halide), phosphorous compounds,

sulphurous compounds, etc., meet most of the requirements listed above, while the sensitivity to air is non-negligible and requires a compromise between performance and safety in future applications.

Starting with the possibilities of metal hydrides as battery materials, the following chapters will explore the potential of hydrides in a battery cell not only as electrodes but also as electrolytes.

2.1.1. Metal Hydrides as Negative Electrode Material with Liquid Electrolyte

In 2008, Oumellal et al. [16] proposed, for the first time, the use of metal hydrides as a negative electrode for Li-ion batteries. While the state-of-the-art technology in commercial Li-ion batteries is based on an intercalation/deintercalation reaction in the graphite electrode, metal hydrides undergo a conversion reaction with the lithium ion, following the general Equation (1):



During the lithiation reaction, the metal hydride undergoes a reduction to its metal and lithium hydride is formed. The lithiation can be completed in one or more steps, depending on the nature of the hydride. This reaction is favorable for all the metal hydrides with Gibbs free energy of formation less negative than that of LiH. The main advantage in using metal hydrides as electrode material is their high gravimetric capacity compared to graphite. Per hydrogen atom exchanged during the reaction, one Li is stored within the electrode, meaning that the minimum quantity stored is one Li per formula unit in the case of monohydrides. On the other hand, only one Li atom is intercalated per six C atoms in a commercial graphite electrode. Therefore, as shown in Figure 1, several metal hydrides exhibit a theoretical capacity that is much higher than graphite. Furthermore, the thermodynamic potential of metal hydrides is in the range of 0.1–1 V vs. Li^+/Li , allowing a high energy density.

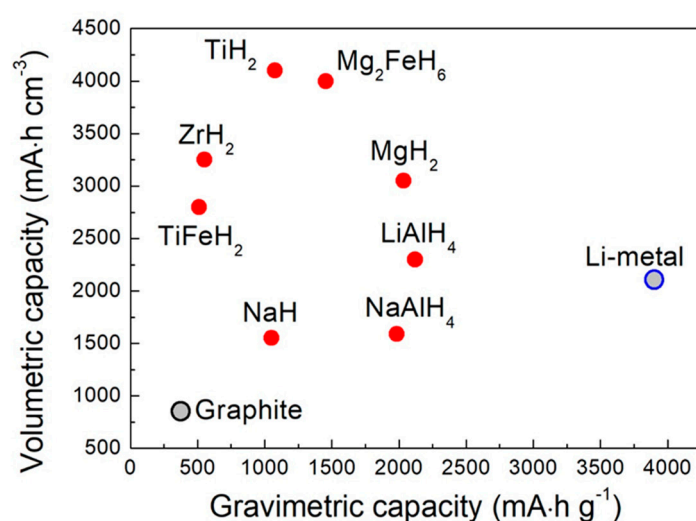


Figure 1. Volumetric and gravimetric specific capacities of metal and complex hydrides compared with those of graphite and lithium metal. The figure was created with the help of [20] and shows the most important values for this chapter.

With a theoretical gravimetric capacity of 2038 mA h g^{-1} , magnesium hydride (MgH_2) was the first hydride investigated as negative electrode and even though a high experimental capacity during lithiation was reached, the MgH_2 electrode exhibited a poor reversibility already within the first discharge/charge cycle [17,21–23]. This drawback was shown for several other metal hydrides [21–25] and despite the strategies suggested in the literature, poor reversibility still hinders practical application of metal hydrides as electrode materials. Several reports [18,20,21,25–27] have tried to elucidate this poor reversibility, highlighting the fact that during lithiation/delithiation, the electrode undergoes severe volume changes which might lead to cracks and a loss of contact between particles. Moreover,

the formation of LiH could decrease the electronic conductivity, hindering the extraction of Li from the electrode [27]. Finally, the conversion reaction is a solid-solid reaction occurring at room temperature (RT) involving complex reactions such as hydride decomposition, phase nucleation and growth, and the diffusion of atoms within the electrode. Therefore, mass transport issues could affect the reversibility as well.

With the aim of better understanding the issues related to the poor reversibility of metal hydrides, **Berti et al.** [28] used MgH₂ thin films deposited on Cu current collectors as a model system to investigate the mechanism occurring during lithiation and delithiation, focusing on the effect of this mechanism on electrode performance. Similarly to powder-electrodes, MgH₂ thin films can be fully lithiated during the first discharge but show poor reversibility during delithiation. Thanks to transmission electron microscope (TEM) microscopy, the structure and phase distribution within the electrode during discharge/charge were investigated and analysed. As displayed in Figure 2, the focused ion beam (FIB) cross sections of the film grow in thickness because of the conversion of MgH₂ to Mg and LiH. During delithiation, they shrink due to partial reformation of MgH₂. However, no voids or cracks are noticed along the cross section, implying that no severe structural damage or loss in contact occurred within the first cycle, which contradicts the above-mentioned initial hypothesis. Volume changes are not the main issue of poor reversibility.

Berti et al. (authors mentioned in bold belong to the MSCA ITN ECOSTORE) performed additional electrochemical impedance spectroscopy (EIS) at different steps and showed that the resistance of the lithiated electrode is indeed lower than the pristine, thus indicating that the electrons are not blocked by the presence of LiH. Their result is supported by the fact that in the TEM images (Figure 2), the lithiated zones are always intimate mixtures of Mg within the LiH matrix; thus, the formation of the metal already provides a path for the electrons. After eliminating mechanical and conductivity issues, the authors suggested that the main cause for the poor reversibility is probably the mass transport within the electrode. Since Li can easily diffuse inside the electrode converting all MgH₂, it is likely that atomic hydrogen transport is the main cause. Indeed, the diffusion coefficient of hydrogen in MgH₂ is known to be low at RT, as described by **Huen et al.** and others [27,29]; hence, it is assumed that the reformation of MgH₂ begins on the surface of the particles and proceeds through the center, which could explain its partial reformation. Consequently, in order to enhance the reversibility, high mobility and short diffusion paths for hydrogen are desirable.

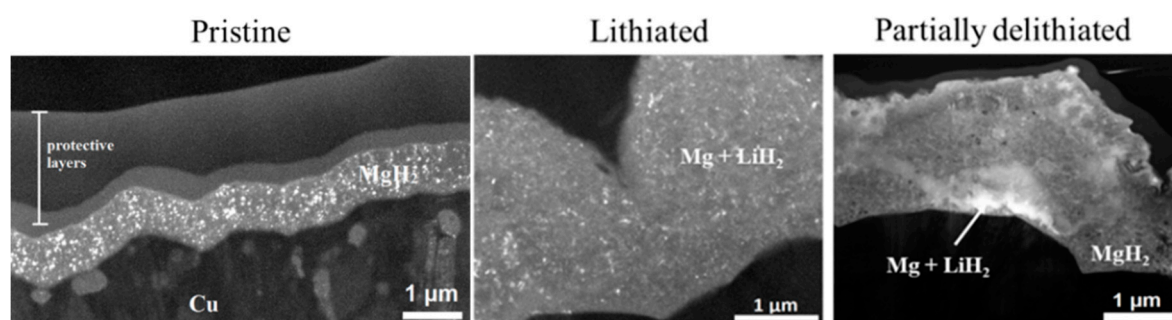


Figure 2. TEM dark field images of FIB cross sections of MgH₂ thin films on Cu, at different reaction steps. The scale indicates 1 μm showing thin film growth and shrinkage during the process of the first cycle.

The mobility of species can be enhanced mainly in two ways, either by working at a higher temperature or by providing preferential pathways (i.e., adding a phase with a higher diffusion coefficient), whereas short diffusion pathways could also be provided by the nanostructuring of the electrode.

With the purpose of improving the electrochemical properties of MgH₂, Huang et al. [30] studied the effect of adding TiH₂ to MgH₂, preparing a 0.7MgH₂ + 0.3TiH₂ composite by means of reactive

ball milling. Indeed, TiH_2 is known for its good electrical conductivity [31] and hydrogen diffusion coefficient [32], which might improve the overall electrode reaction. The electrode prepared by Huang et al. showed improved electrochemical properties compared to MgH_2 - [16] and TiH_2 - [23] based electrodes in terms of reversible capacity and polarization, highlighting a cooperative effect between these two hydrides in a conversion reaction. During lithiation, both hydrides were reduced to Mg and Ti, forming LiH, and after de-lithiation, the partial reformation of both hydrides was observed. It was demonstrated by the authors that the presence of TiH_2 enhances the kinetics of the conversion of MgH_2 , whereas MgH_2 enables the partial reformation of TiH_2 . Expanding the work of Huang, **Berti et al.** [33] prepared different mixtures of $y\text{MgH}_2 + (1 - y)\text{TiH}_2$ (with molar ratio $0.2 \leq y \leq 0.8$) by means of ball milling to investigate the ratio effect on the conversion reaction.

In agreement with Huang et al. [30] **Berti et al.** [33] also found the partial reformation of both MgH_2 and TiH_2 in a MgH_2 -rich composite electrode. However, **Berti et al.** showed that the reformation of these hydrides does not always appear in all the mixtures, but strongly depends on the molar ratio. Indeed, for TiH_2 -rich composite ($y = 0.2$) neither MgH_2 nor TiH_2 were observed during the first de-lithiation of the electrode. For the equimolar composite ($y = 0.5$), only the partial reformation of TiH_2 was clearly observed, and finally, in MgH_2 -rich electrode ($y = 0.8$) both hydrides were reformed.

Additional studies by **Berti et al.** [34] showed that the highest reversibility (75%) is obtained for $0.7\text{MgH}_2 + 0.3\text{TiH}_2$. As better shown in Figure 3a, the TiH_2 phase exhibits a higher reversibility than MgH_2 in this composite, with 90% vs. 40%, respectively, within the first cycle. Further investigation of the reversibility of the TiH_2 phase in this composite showed that when the conversion reaction is limited to this hydride (between 0.1 and 0.45 V, as shown in Figure 3b, in order to avoid both the contribution of MgH_2 and Mg-Li alloy reactions), a high initial reversibility and good capacity retention in the subsequent cycles were achieved. This improvement of the performance for the TiH_2 phase was attributed to the intimate mixtures and short diffusion pathways provided by the mechanochemical synthesis, which also offers a high density of Ti/LiH interfaces. This latter hypothesis is also supported by the work of Oumellal et al. [35], in which intimate mixtures of $\text{LiH} + \text{M}$ (where $\text{M} = \text{Mg}$ and Ti) were prepared by mechanochemical synthesis. Interestingly, when a mixture of $\text{Ti} + 2\text{LiH}$ prepared by ball milling is de-lithiated, the reformation of TiH_2 is partially observed (around 40%). This fully supports the hypothesis that good M/LiH interfaces and short diffusion paths are needed in order to extract lithium from the electrode and reform the hydride. Moreover, these latter conclusions clearly show that the preparation of the electrode is key to improving the overall conversion reaction. A direct comparison between the $0.7\text{MgH}_2 + 0.3\text{TiH}_2$ electrodes of **Berti et al.** [34] and Huang et al. [30], cycled without the contribution of the alloying reaction, shows differences in the contribution of the hydrides. Berti achieved a reversible capacity for MgH_2 of 0.56Li (i.e., 40%) and 0.54Li for TiH_2 (90%), whereas Huang obtained 1.1Li (78%) and 0.4Li (67%), respectively. These results might be due to the different electrode preparations in these works. Indeed, the composites were prepared with different mechanochemical procedures, also adding different additives to the composites. Moreover, the electrodes were cycled at different C-rates, and as clearly shown by Huang, a faster discharge/charge rate leads to a decrease in the reversible capacity and to an increase in the polarization, highlighting the importance of an appropriate C-rate on the overall performance. The fact that preparation plays a key role was also shown by Oumellal et al. [16], who cycled two MgH_2 electrodes prepared in different ways under the same conditions (C/20 between 3 and 0.15 V). The electrode prepared with MgH_2 , ball milled for a longer period, exhibited a better performance, achieving a reversibility of 1.5Li, with an increase of 20% compared to the electrode ball milled for a shorter time (1.1Li). In light of these facts, it is clear that not only the composition of the electrode is relevant for the sake of the performance, but also its preparation and working conditions must be taken into account with the purpose of further improving the reversibility and cycle-life of metal hydride-based electrodes.

Apart from mechanochemical synthesis, the cycling performance of metal hydride electrodes has shown to be improved by nanoconfinement using carbonaceous scaffolds [36–39]. Prior to application in Li-ion batteries, nanoconfinement was shown to modify both the thermodynamic and kinetic

properties of metal hydrides for hydrogen storage (Section 3.5. and Refs. [40,41]). Therefore, several research groups have implemented this bottom-up approach. Oumellal et al. [36] reported that MgH_2 infiltrated in high surface area graphite can achieve a high reversible capacity of 500 mAh g^{-1} . Similarly, Huen et al. [37] showed that it is possible to enhance the reversibility of sodium alanate (NaAlH_4) by nanoconfinement from 30% up to 70%. Using *operando* X-ray powder diffraction (XPD) to investigate the conversion reactions of NaAlH_4 during discharge, it was found that the formation of intermediate $\text{LiNa}_2\text{AlH}_6$ is dominant in the ball-milled sample. However, in the nanoconfined sample, the formation of another intermediate Na_3AlH_6 phase occurs and competes with the formation of $\text{LiNa}_2\text{AlH}_6$. In general, the confinement within a scaffold improves the reactivity of metal hydrides not only by shortening the diffusion path, but also by altering the conversion mechanism.

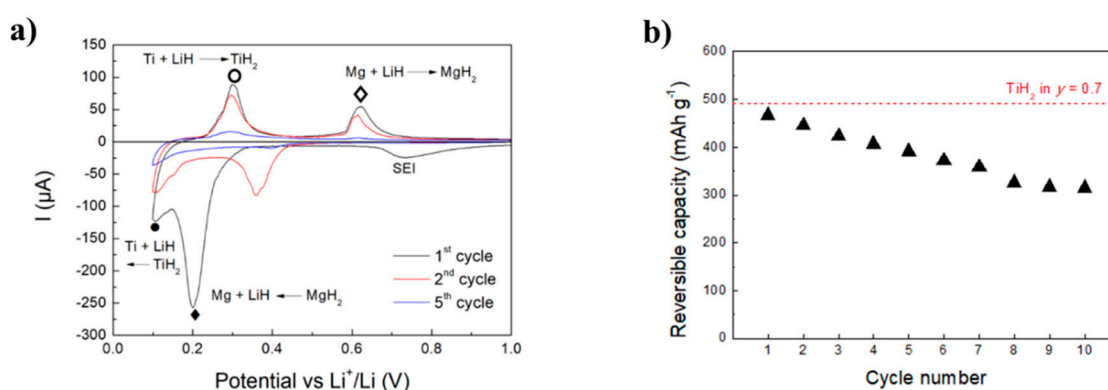


Figure 3. (a) Cyclic voltammetry of $0.7\text{MgH}_2 + 0.3\text{TiH}_2$. (b) Reversible capacity of the TiH_2 phase in the composite cycled in the range 0.1–0.45 V.

Additionally, carbonaceous scaffolds are similar to graphite and allow intercalation of Li ions [37,42–44]. Since the reaction potential of some metal hydrides and carbon are in the same range, it is difficult to separate and avoid the intercalation of Li into carbon. Therefore, in order to further enhance the performance of nanoconfined metal hydride electrodes, novel scaffolds that are electrically conductive but inert to Li ought to be explored.

2.1.2. Promising Complex Metal Hydrides as Solid-State Electrolytes

Since the discovery of the first ionic conductor PbF_2 and Ag_2S by Michael Faraday in the 19th century, further conductors have been described throughout the centuries [45,46] and material scientists have achieved great progress in novel ionic conductors with a higher conductivity and better applicable properties. These compounds are also promising for all-solid-state batteries (ASSBs). There are many different families of ionic conductors for ASSBs which may offer high ionic conductivity near RT: Lithium Super Ionic CONductor (LISICON), argyrodites, lithium-nitrides, lithium-hydride family, garnet type, perovskites, etc. [47]. Generally, the ionic conductivity of Li^+ in the materials can be improved by chemical substitution and material design [48]. The transportation mechanism of Li-ion in super ionic conductors has been reported as well [49–54]. Though the general understanding of the fundamental mechanism leading to high Li-conductivity is not well established, it is clear that for a specific material with high ionic conductivity, the availability of ion diffusion channels or conduction channels is a vital prerequisite. Metal hydrides and hydride complexes exhibit high hydrogen mobility. Therefore, they possess diffusion channels, which might be used to transport other ions, such as alkaline-earth cations, finding possible application as super ionic lithium conductors [55–60].

Lithium Borohydride

In the field of energy applications, LiBH_4 with its high gravimetric hydrogen content was originally studied as a material suitable for solid-state hydrogen storage (see Section 3.2 and Reference [56]).

Due to the high mobility of hydrogen in LiBH_4 , it was suggested that lithium mobility could also be promoted, which makes the material act as a Li ionic conductor. The advanced mobility of lithium ion in LiBH_4 was first confirmed by Matsuo et al. in 2007 [59]. The crystal structure of LiBH_4 is shown in Figure 4. It transforms from a low-temperature (LT), orthorhombic phase to a high-temperature (HT) hexagonal phase at $\sim 117^\circ\text{C}$. The LT-orthorhombic and HT-hexagonal phases exhibit conductivities of 8.6×10^{-8} and $10^{-3} \text{ S cm}^{-1}$ at 20 and 120°C , respectively [59]. An explanation can be found in the LT phase, where it was reported that Li^+ ions are blocked by $[\text{BH}_4]^-$ tetrahedral anions. The diffusion of Li^+ ions needs to be facilitated by the rotation of $[\text{BH}_4]^-$ tetrahedrons, which needs a high activation energy. On the other hand, in the HT phase, Li^+ ions are not blocked by the tetrahedrons. Li^+ ions diffuse along the crystallographic axes *a* and *b* easily while rotation of the tetrahedrons also facilitates the migration of Li^+ [61–63]. While transforming from the LT to the HT phase, the activation energy for the Li^+ ion mobility decreases from 0.69 to 0.53 eV [62]. Moreover, LiBH_4 is an electronic insulator in both structures. Theoretical calculations show a large band gap of $\sim 6.7 \text{ eV}$ [60]. While powders are most commonly used for such investigations, a similar behaviour is reported for LiBH_4 melt-frozen films. Trück et al. [64] described an auspicious method of film preparation by spin coating and investigating the ionic conductivity of crystalline LiBH_4 films. The authors have reported the phase change from LT to HT modification at 110°C with an ionic conductivity of the HT phase of $10^{-3} \text{ S cm}^{-1}$.

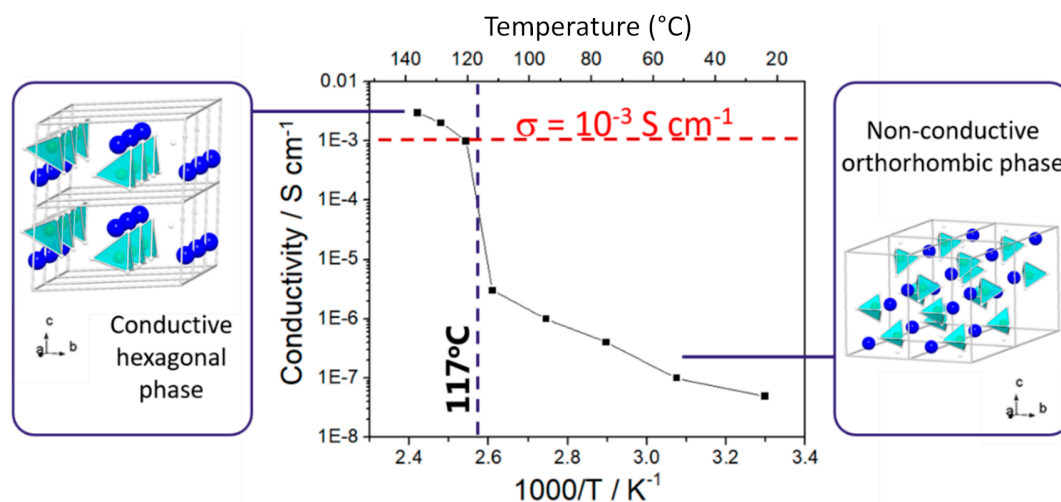


Figure 4. Conductivity of LiBH_4 at non-conductive low temperature phase (orthorhombic structure) and at conductive high temperature phase (hexagonal structure). The blue spheres are lithium ions and the light blue tetrahedrons are BH_4 anions with a yellow sphere (boron) inside them.

With such high lithium conductivity for the HT phase, the electronic insulator LiBH_4 becomes a very interesting candidate for solid electrolytes in ASSBs. Several successful achievements have been attained using different electrode materials combined with LiBH_4 as solid electrolyte [65,66].

Lithium Nitride and Lithium Hydride

The interest in Li_3N as an ionic conductor was based on its hexagonal crystalline structure made of a Li_2N^- layer and a pure Li^+ ionic layer, resulting in the free movement of Li^+ ions in a two-dimensional pathway within the lattice [67,68]. Thus, the ionic conductivity of Li_3N reaches $1.2 \times 10^{-4} \text{ S cm}^{-1}$ at 27°C [67]. However, this compound decomposes at low potential of 0.44 V limiting its application in ASSBs [68,69]. Nevertheless, when Li is partially replaced by hydrogen, forming lithium imide Li_2NH , the electrochemical stability of the compound is improved compared to Li_3N [68]. It was shown experimentally that Li_2NH has high ionic conductivity at RT with $2.54 \times 10^{-4} \text{ S cm}^{-1}$ (according to activation energy $E_a = 0.63 \text{ eV}$). This high conductivity originates from the presence of H^+ in the Li_2N^- layer. N-H bonds form, weakening the Li-N bonding and facilitating the diffusion of Li^+ . The

decomposition voltage of Li_2NH is 0.7 V, which is higher than that of Li_3N but still too low for a solid electrolyte [70].

Lithium imide (Li_2NH) has been studied extensively as a prospective reversible hydrogen storage material [71,72]. Nearly four decades ago, Boukamp et al. [73] reported, for the first time, high Li-ion conductivity in Li_2NH ($>10^{-4}$ S/cm at RT) and since then, it has been reconsidered as a promising solid-state electrolyte in the Li-ion battery. Recent interest in Li_2NH as a practical, cost effective, high-density electrolyte comes from several advantages. For example, its benefits are its lightweight (molar weight = 28.9 g mol^{-1}), abundant elements (especially nitrogen), its thermal stable nitrogen sublattice, appropriate suitable anion dynamics for cation diffusion, uncomplicated synthesis methods, etc. Nevertheless, the understanding of the electrochemical properties of Li_2NH is still debated in literature, especially ionic conduction, leading to several crystal structures and controversial results on resolved structures [70].

Recently, the connection of the cubic and the orthorhombic phases of Li_2NH has been elucidated by Paik et al. [70], especially, in terms of the structural evolution, showing that the formation of the aforementioned phases is part of a continuous structural ordering [70]. The orthorhombic Li_2NH phase was identified to undergo the order–disorder phase transformation. Although no rapid change in ionic conductivity has been reported from this phase transformation, which is confirmed by the ionic conductivity estimated for these structures between 27 and 127°C . The ionic conductivity data also help to reveal a likely cation diffusion mechanism. Ionic conductivity in cubic Li_2NH is reportedly higher than in the orthorhombic Li_2NH . Furthermore, contrarily to a prior prediction [73], the electrochemical stability window in the cubic Li_2NH is wider for the Li/ Li_2NH interface (>5 V).

Structural differences between the orthorhombic α - Li_2NH phase and cubic β - Li_2NH phase can be found in Figure 5 and have been determined by different characterization methods such as Raman and XPD (Figure 5b,c) [70]. However, the structural evolution of the aforementioned structures may be described as a transformation of tetragonal LiNH_2 into α - and β - Li_2NH via the formation of nonstoichiometric Li-NH phases, $\text{Li}_{(1-x)}\text{NH}_{(2-x)}$ ($0 < x < 1$) [70]. This mechanism for transformation is based on the proposed study of the dehydrogenation model for LiNH_2 by David et al. [74]. According to their model, the filling of vacant Li sites in the lattice of LiNH_2 initiates a structural transition from the Li-poor to Li-rich phase and thus, from tetragonal into cubic Li_2NH phase and converting a poor Li-ion-conductor into a better one, respectively. Theoretical calculations suggest that $[\text{NH}_2]^-$ groups block Li^+ diffusion in LiNH_2 and indeed, LiNH_2 is almost an ionic insulator at RT with a high Li^+ ion activation energy of 1.05 eV [68].

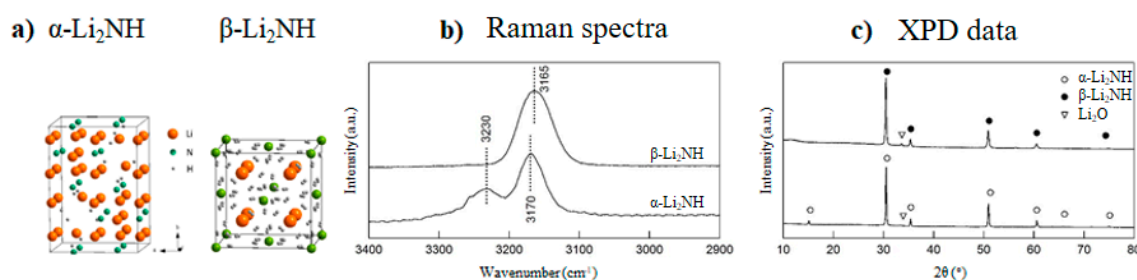


Figure 5. (a) The crystal structure of orthorhombic α - Li_2NH in s.g. $Ima2$, $a = 7.133 \text{ \AA}$, $b = 10.087 \text{ \AA}$, $c = 7.133 \text{ \AA}$ and cubic β - Li_2NH in s.g. $Fm\bar{3}m$, $a = 5.074 \text{ \AA}$; (b) Raman spectra of α - Li_2NH and β - Li_2NH structures and (c) XPD profiles. Adapted with permission from Paik, B.; Wołczyk, A. Lithium imide (Li_2NH) as a solid-state electrolyte for electrochemical energy storage applications. The Journal of Physical Chemistry C, 2019, 123, 1619–1625. Copyright (2019) American Chemical Society.

The ionic conductivity for β - Li_2NH has been reported to be $5 \times 10^{-4} \text{ S cm}^{-1}$, compared to $\sim 10^{-4} \text{ S cm}^{-1}$ in α - Li_2NH [70], in a temperature range between 27 and 107°C . The endothermic phase

change from α - to β -phase at 77–87 °C did not yield a drastic change in ionic conductivity. The increase is rather a result of cation and anion ordering.

Binary Phases of Hydrides with Lithium Halides

Similarly to the idea of replacing one Li by hydrogen in Li_3N to stabilize the compound, lithium halides were added to LiBH_4 to form a solid solution, expecting a HT LiBH_4 structure stabilized at RT. For this reason, mixtures of LiBH_4 with LiCl , LiBr , and LiI were investigated [75–80]. Solid solutions were obtained by high-energy ball milling or annealing of LiBH_4 with different ratios of LiI under Ar and promising conductivities were achieved. An array of solid solutions of $\text{Li}_{x+1}\text{I}(\text{BH}_4)_x$ was studied by Orimo and co-workers, where the obtained $\text{Li}_4\text{I}(\text{BH}_4)_3$ phase reached super ionic conductivity as high as $4 \times 10^{-4} \text{ S cm}^{-1}$ at RT [75,77,78]. XPD studies confirmed the formation of a single phase without any impurities [75]. Additional DFT calculations showed that in the presence of LiI , lithium defects were easily formed at RT in the solid solution (energy formation of 0.44 eV). This was explained by the fact that energy barriers which were found between stable defect sites are low (0.2 to 0.3 eV), giving rise to a high defect mobility [81].

Following the same principle, solid solutions of LiNH_2 and LiI at different ratios were studied [82–84]. The ionic conductivity of $\text{Li}_3(\text{NH}_2)_2\text{I}$ has been reported to be $1.7 \times 10^{-5} \text{ S cm}^{-1}$ at 27 °C ($E_a = 0.58 \text{ eV}$). However, the EIS spectrum of the compound showed a significant ionic resistance of both the bulk material and grain boundaries. The grain boundary resistance was attributed to the mechanical property of the compounds and the preparation method [82].

The heat treatment of LiNH_2 and LiCl (molar ratio = 1:3) resulted in the formation of rhombohedral and cubic polymorphs of $\text{Li}_4(\text{NH}_2)_3\text{Cl}$, and at lower LiCl ratios, $\text{Li}_7(\text{NH}_2)_6\text{Cl}$ formed [85]. These compounds were reported to have faster hydrogen desorption kinetics than the halide-free system. LiNH_2 has the same decomposition temperature but additional NH_3 was detected in addition to H_2 [85]. The halide anion is believed to increase hydrogen mobility in the system. In addition, Li sites in the structure are not completely occupied which might increase Li^+ mobility and thus result in a higher ionic conductivity [85].

Two binary single phases $\text{Li}_2\text{BH}_4\text{NH}_2$ and $\text{Li}_4\text{BH}_4(\text{NH}_2)_3$ were obtained, when the complex hydrides LiBH_4 and LiNH_2 were ball milled in ratios of 1:1 and 1:3, respectively. A conductivity of $2 \times 10^{-4} \text{ S cm}^{-1}$ was measured for both ratios at RT [86]. At 97 °C, the conductivities increased up to $6 \times 10^{-2} \text{ S cm}^{-1}$ and $10^{-3} \text{ S cm}^{-1}$, respectively. Similarly to what was observed in pure LiBH_4 , EIS of the mixture exhibits no significant grain boundary resistance [86].

$\text{LiBH}_4\text{-Li}_2\text{NH}$: $\text{Li}_5(\text{BH}_4)_3\text{NH}$ —thorough characterization of a cluster complex hydride

A new complex hydride with the formula $\text{Li}_5(\text{BH}_4)_3\text{NH}$ has been synthesized by ball milling of LiBH_4 and Li_2NH in a 3:2 molar ratio and by post annealing [72]. An orthorhombic phase was already observed by Blomqvist et al. [87], but could not be isolated or formed pure. Recently, the crystal structure of $\text{Li}_5(\text{BH}_4)_3\text{NH}$ was solved in space group (s.g.) Pnma [72] with unit cell parameters $a = 10.2031(3)$, $b = 11.5005(2)$ and $c = 7.0474(2) \text{ \AA}$ at 77 °C. DFT and synchrotron radiation X-ray powder diffraction (SR-XPD) measurements followed the model previously established for the 1:1 composition of $\text{LiBH}_4\text{:Li}_2\text{NH}$ by Hewett et al. [88], while solid-state nuclear magnetic resonance (NMR) measurements confirmed the chemical shifts calculated by DFT. The latter calculations underlined the ionic character of this lithium-rich compound, revealing a potential for use in LiBs.

$\text{Li}_5(\text{BH}_4)_3\text{NH}$ is a mixed anion salt comprised of borohydride and imide anions and is based on packing of a small complex anion BH_4^- and big complex cation $[\text{Li}_5(\text{NH})]^{3+}$. The latter corresponds to higher coordinating power of imide compared to amide [72]. In Orimo et al. [89], the reported complex of $\text{Li}_4(\text{BH}_4)(\text{NH}_2)_4$ is described by the replacement of amide anions by imide anions. $\text{Li}_4(\text{BH}_4)(\text{NH}_2)_4$ is based on packing of small cation Li^+ and complex anions BH_4^- and NH_2^- , resulting in close to cubic closed packing of anions.

Figure 6a shows the crystal structure of $\text{Li}_5(\text{BH}_4)_3\text{NH}$ which contains a particular structural feature. The imide anion is coordinated by a square pyramidal cluster of five Li atoms. With five cations per four complex anions, the compound is Li rich and the coordination of the borohydride anions is five-fold. Nevertheless, the latter is more irregular than the coordination of imide. All Li atoms are a fragment of immensely deformed tetrahedral coordination comprising of one NH_2^- anion and three BH_4^- . The anion $[\text{Li}_5(\text{BH}_4)_4(\text{NH})]^-$ has an overall C_{2v} symmetry when surrounded by four BH_4^- anions which has been determined from geometry optimization. The HOMO and HOMO-1 orbitals are shown in Figure 6b for the anion $[\text{Li}_5(\text{BH}_4)_4(\text{NH})]^-$ which are the p_x and p_y N atomic orbitals and both have the same energy. This specific arrangement proposes that the surrounding $[\text{BH}_4]^-$ anions play a crucial role by stabilizing the core of $[\text{Li}_5(\text{NH})]^{3+}$. With the exception of the covalent N–H bond, the aforementioned square pyramidal $[\text{Li}_5(\text{NH})]^{3+}$ core is of a pure ionic nature. It polymerizes into the $\text{Li}_5(\text{BH}_4)_3\text{NH}$ crystal structure while keeping its complex cation character balanced by three anions of BH_4^- . $\text{Al}_3\text{Li}_4(\text{BH}_4)_{13}$ is the other known example of a complex cation which was found with $[\text{Li}_4(\text{BH}_4)]^{3+}$ as tetrahedral cation [90].

Wołczyk et al. [72] reported a comparison of the ionic conductivity data for LiBH_4 , Li_2NH and $\text{Li}_5(\text{BH}_4)_3\text{NH}$. The RT ionic conductivity of the $\text{Li}_5(\text{BH}_4)_3\text{NH}$ compound reaches $10^{-6} \text{ S cm}^{-1}$ with an activation energy of 0.73 eV. Showing one order of magnitude higher conductivity than LiBH_4 does at RT and three orders of magnitude lower than Li_2NH . The observed inconsistencies in the Li-ion conductivity in the three orthorhombic complex hydrides are elucidated in the following and explained by ionic conduction mechanisms. Noritake et al. have reported that the rotational motion of the translational static BH_4^- anions improves the mobility of Li^+ ions in case of LiBH_4 [91] while charged vacancies or Frenkel pair defects are considered in the case of Li_2NH [68]. For the orthorhombic $\text{Li}_5(\text{BH}_4)_3\text{NH}$ compound, the Li-ion conductivity may be affected by the two anion configurations, which are closely related to the determined crystal structure.

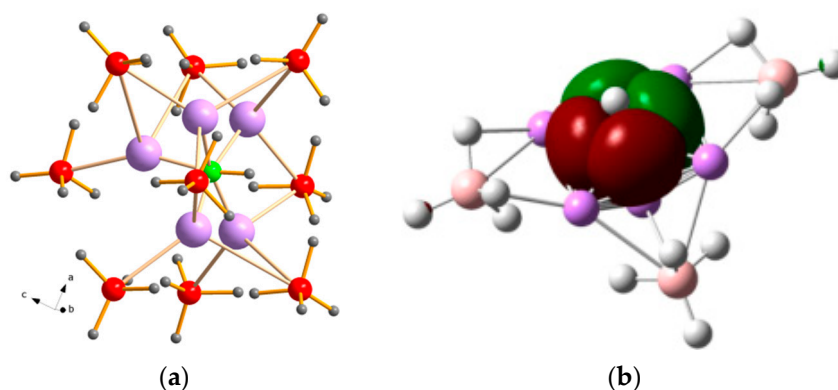


Figure 6. (a) Crystal structure of $\text{Li}_5(\text{BH}_4)_3\text{NH}$ showing the complex cation $[\text{Li}_5(\text{NH})]^{3+}$ counter-balanced by three BH_4^- anions. (b) HOMO and HOMO-1 of the DFT optimized geometry of $[\text{Li}_5(\text{NH})(\text{BH}_4)]^-$. One $[\text{BH}_4]^-$ unit is hindered for clarity. Red(-dish) is B; gray, H atom; purple, Li atom; green, N atom. Adapted with permission from Wołczyk, A., B. Paik, T. Sato, C. Nervi, M. Brighi, S.P. GharibDoust, M. Chierotti, M. Matsuo, G. Li, R. Gobetto, T.R. Jensen, R. Černý, S.-i. Orimo, and M. Baricco, $\text{Li}_5(\text{BH}_4)_3\text{NH}$: Lithium-Rich Mixed Anion Complex Hydride. *The Journal of Physical Chemistry C*, 2017. 121: pp. 11069–11075. Copyright (2017) American Chemical Society.

It is worth pointing out that the Li-ionic conductivity of $\text{Li}_5(\text{BH}_4)_3\text{NH}$ is comparable to some of the newly reported binary complex hydrides, including $\text{LiBH}_4\text{-LiX}$ solid solutions ($\text{X} = \text{Cl}, \text{Br}, \text{I}$) [75] and $\text{Li}_4(\text{BH}_4)(\text{NH}_2)_3$ [92]. This suggests a connection of Li-based complex hydrides containing $[\text{BH}_4]^-$ and $[\text{NH}]^{2-}$ anions which are potential choices to support a high Li-ionic conduction at RT [75].

Argyrodite Structure Materials

Since the first solid ionic conductor, researchers have worked on the improvement of ionic conductivity by replacing the cation [93] and anion [94] in the original substance. Following the high mobility of Ag^+ in mineral argyrodite Ag_8GeS_6 , Deiseroth et al. discovered that substituting Ag^+ by other cations in the structure led to a very high cationic conductivity [93]. Subsequently, $\text{Li}_6\text{PS}_5\text{X}$ compounds ($\text{X} = \text{Cl}, \text{Br}$ or I) adopting the argyrodite structure were synthesized and the authors reported high conductivities [93,95]. For $\text{X} = \text{Br}$, the ionic conductivity reaches $10^{-3} \text{ S cm}^{-1}$ [96,97] which is comparable to some liquid electrolytes. Ionic conductivity (σ) of other halide argyrodites (Arg-X) decreases with the radius of the halide anion, i.e., $\sigma_{\text{Arg-Br}} > \sigma_{\text{Arg-Cl}} > \sigma_{\text{Arg-I}}$.

The halide argyrodites with a high lithium ion conductivity are a new group of lithium super ionic conductors. The relationship between the ionic conductivity and the radius of the halide anions suggests that anion substitution of the halide can modify the lattice parameter and improve the conductivity. In the frame of studying the practical applications, the $[\text{BH}_4]^-$ anion was chosen as a promising substituting anion which can potentially enhance the Li^+ conductivity of these argyrodites. Dao et al. [98] synthesized the argyrodite $\text{Li}_6\text{PS}_5\text{I}_{5/6}(\text{BH}_4)_{1/6}$ and reported a significant improvement of ionic conductivity of $6 \times 10^{-4} \text{ S cm}^{-1}$ at RT, two orders of magnitude higher than the original compound [99]. The crystalline structure of the cubic argyrodite $F\bar{4}3m$ remained; only the lattice parameters of the material was varied due to the difference of ionic radii. Surprisingly, while the conductivity of $\text{Li}_6\text{PS}_5\text{I}_{5/6}(\text{BH}_4)_{1/6}$ was ameliorated, that of $\text{Li}_6\text{PS}_5\text{Br}_{5/6}(\text{BH}_4)_{1/6}$ was reduced compared to the pure halide argyrodite, which can be explained by the local geometry constraints of the Li diffusion pathway. The conductivity of the $\text{Li}_6\text{PS}_5\text{BH}_4$ synthesized by mechanochemical reaction is as high as $1.9 \times 10^{-3} \text{ S cm}^{-1}$ at RT [100]. The combination of the borohydride with sulphide and thio-sulphate compounds was also found to be appealing, resulting in a high ionic conductivity, a good electrochemical stability and compatibility with many electrode materials [101,102].

2.1.3. Application of Metal Hydrides in Solid-State Cells

After a careful exploration of the use of metal hydrides as electrode and electrolyte materials, it is important to review the latest reports on their use in all-solid-state cells. Half-cells and full-cells have been reported in the literature and are discussed here, revealing the importance of metal hydrides for future advancements in all-solid-state batteries [103].

Solid-State Half-Cell

Recently, metal hydride electrodes have been investigated in batteries using solid electrolytes such as LiBH_4 and $\text{Li}_2\text{S-P}_2\text{S}_5$ [104–111]. Solid electrolytes allow the operation of batteries at elevated temperatures at which the reaction kinetics of the hydride conversion can be greatly improved.

Complex metal hydrides, including Mg_2FeH_6 , have poor cycling performances at RT when standard liquid electrolyte is used [112]. Huen et al. [113] studied, for the first time, Mg_2FeH_6 in solid-state batteries using LiBH_4 electrolyte. At high temperature, the first Coulombic efficiency and retained capacity of Mg_2FeH_6 are improved significantly. In addition, the decomposition of Mg_2FeH_6 into MgH_2 was discovered during discharge. However, it should be noted that Mg_2FeH_6 in ASSBs was tested at 120°C and it is difficult to conclude whether the formation of MgH_2 is temperature-dependent. Since the conversion reaction of Mg_2FeH_6 is more complete, this chapter also provides new insight into the reaction mechanism, especially during charge.

Resuming the work on $y\text{MgH}_2 + (1 - y)\text{TiH}_2$ (with molar ratio $0.2 \leq y \leq 0.8$) mixtures, Dao et al. [114] investigated the properties of these composites at 120°C using LiBH_4 as solid electrolyte. As shown in Figure 7, half-cells were cycled at different C-rates.

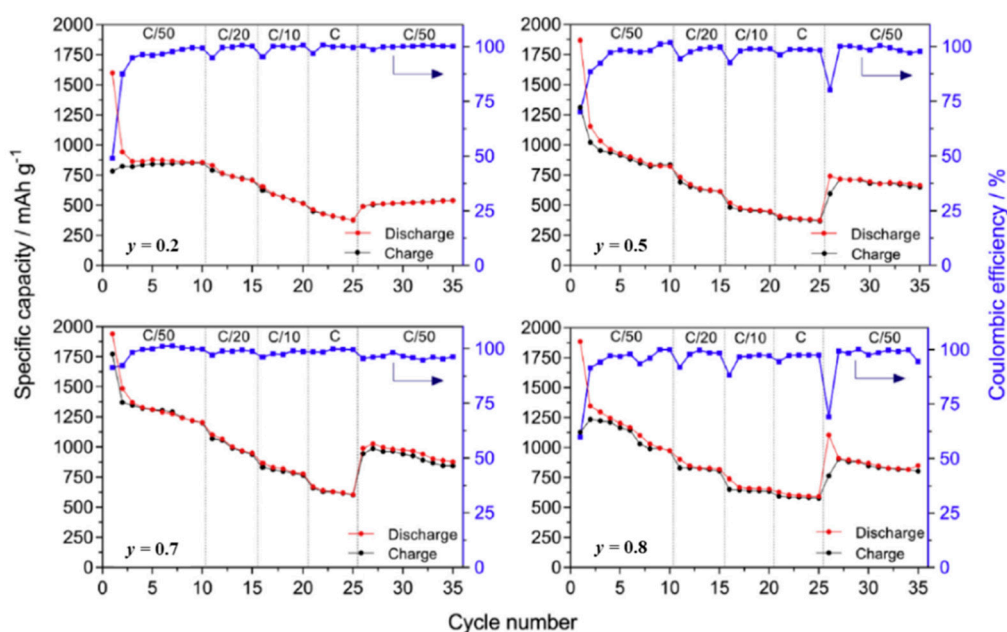


Figure 7. Galvanostatic cycling of $y\text{MgH}_2 + (1-y)\text{TiH}_2$ composites at different kinetic regimes in solid-state half-cells. Cells were tested at $120\text{ }^\circ\text{C}$ using LiBH_4 as solid electrolyte.

Compared to RT work [33], Dao et al. found a higher reversibility for all the mixtures. Composite $0.7\text{MgH}_2 + 0.3\text{TiH}_2$ exhibits the highest initial reversibility ($\sim 90\%$) among the electrodes, which is in agreement with previous findings. Moreover, after ten cycles at C/50, this mixture delivers the highest capacity (1250 mAh g^{-1}). This is attributed to better kinetics of the composite $y = 0.7$ compared to other $y\text{MgH}_2 + (1 - y)\text{TiH}_2$ electrodes. On the other hand, the Ti-rich composite $y = 0.2$ was found to be reversible, although at RT, this composite did not show the reformation of both hydrides. Furthermore, even if the initial reversibility is around $\sim 45\%$, in the subsequent cycles, it exhibits the highest capacity retention, suggesting that at $120\text{ }^\circ\text{C}$ TiH_2 possesses a better cycling stability than MgH_2 . However, when a faster C-rate is applied, all electrodes show a decrease in capacity due to kinetic limitations. Nevertheless, these electrodes still provide capacities above 300 mAh g^{-1} , even at 1C, with a Coulombic efficiency generally above 90%. All Mg-rich electrodes ($y \geq 0.5$) are able to retrieve their capacities when C/50 is restored as working condition, whereas $y = 0.2$ shows a poor recovery, suggesting some degradation within the electrode due to the fast cycling. The authors suggest that the volume changes occurring during discharge/charge could lead to voids or cracks within a solid-state half-cell and thus, a loss in contact between the particles. Certainly, achieving good contact in an all-solid-state battery is a difficult task due to the fact that the solid electrolyte cannot easily reach every particle like a liquid electrolyte can. Moreover, the accommodation of volume changes could be hampered when using hard materials. Hence, electrode preparation and formulation still remain challenging topics for practical application of all-solid-state batteries. Table 1 summarizes recent results on the utilization of metal hydrides in all-solid-state batteries.

Finally, the composites of $\text{MgH}_2 + \text{TiH}_2$ cycled with LiBH_4 as solid electrolyte at $120\text{ }^\circ\text{C}$ have displayed good electrochemical performance, which could suggest a suitable application in all-solid-state batteries in the future. Still, to accomplish the implementation in a complete cell, it will be necessary to find appropriate lithium-based cathode materials with comparable capacities while the challenge of chemical compatibility and stability against the solid electrolyte need to be faced.

Table 1. Selected recent all-solid-state battery systems utilizing metal hydrides.

Cell Configuration	Maximum Capacity, mAh g ⁻¹	Reversible Capacity at C-Rate	Reported Cycle Number	Retention Capacity, mAh g ⁻¹ at the Last Cycle	Reference
0.7MgH ₂ – 0.3TiH ₂ LiBH ₄ Li	1950	90% at C/50	35	900 (51%)	[114]
MgH ₂ LiBH ₄ Li	1750	94% at C/20	50	924 (45%)	[105]
TiH ₂ LiBH ₄ Li	1052	86% at 2.5C	50	878 (82%)	[108]
25Al ₂ O ₃ – 75MgH ₂ 80Li ₂ S – 20P ₂ S ₅ Li	3300	50% at	9	580 (17.6%)	[106]

A Full Solid-State Li-ion Cell

With the aim of building a full “all-solid-state battery” cell, **López-Aranguren et al. [115]** coupled the 0.8MgH₂ + 0.2TiH₂ mixture with sulphur as the counter electrode. Indeed, these materials show similar theoretical capacities (1718 vs. 1672 mAh g⁻¹) and sulphur had already shown good results as electrode in cells with LiBH₄ as a solid electrolyte [116]. The galvanostatic cycling of the all-solid-state battery is reported in Figure 8.

As displayed in Figure 8a, the hydride electrode is fully lithiated during the first charge, similarly to the previous work in half-cells with both liquid and solid electrolytes. Within the first cycle, it shows a limited reversibility (~55%); however, in the subsequent charge/discharge, the battery exhibits a good capacity retention. At faster C-rates, a decrease in capacity is found though a Coulombic efficiency close to 100% is kept even at C/10. When C/50 is re-applied, the capacity regains previous values (~800 mAh g⁻¹), exhibiting a good capacity retention in the subsequent cycles.

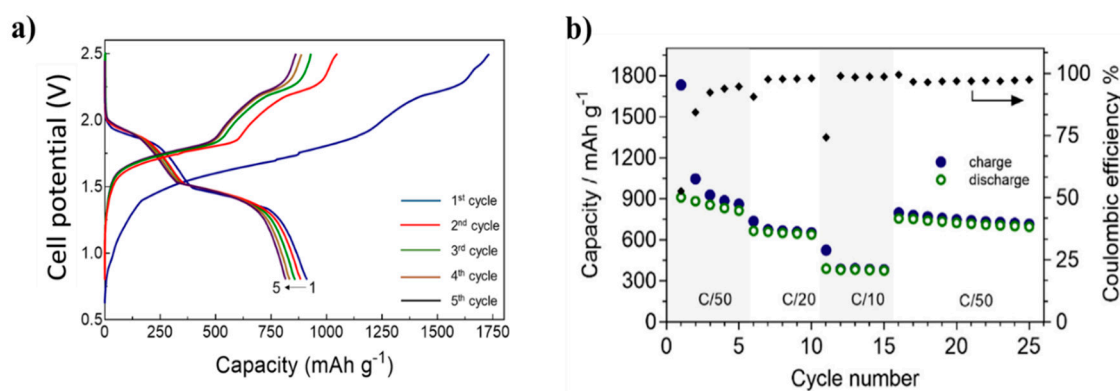


Figure 8. (a) Galvanostatic profiles of the full battery 0.8MgH₂ + 0.2TiH₂||LiBH₄||Li₂S. (b) Delivered capacities and Coulombic efficiency at different kinetic regimes. Reprinted from López-Aranguren, P., N. Berti, A.H. Dao, J. Zhang, F. Cuevas, M. Latroche, and C. Jordy, An all-solid-state metal hydride – Sulphur lithium-ion battery. *Journal of Power Sources*, 2017. 357: p. 56–60. Copyright (2017), with permission from Elsevier.

Comparing these data with those of **Dao et al. [114]**, it is possible to notice that the full battery delivers a capacity slightly lower than the composite 0.8MgH₂ + 0.2TiH₂ in a half cell alone, suggesting that this limitation could be caused by the cathode material. Indeed, sulphur suffers of poor electric conductivity and sluggish kinetics [117], therefore, its theoretical capacity has never been achieved. Nonetheless, the complete all-solid-state battery of **López-Aranguren et al.** has shown the feasible coupling of hydrides and sulphur with promising results.

2.1.4. Conclusions

Generally, metal hydrides have shown improved performance when used in Li-ion battery systems at higher temperatures thanks to the fact that mass transportation within the electrode is enhanced compared to RT cycling. From the discussed findings, it is suggested that practical use of these active materials (electrodes and electrolytes) in Li-ion batteries might come initially for high temperature applications. However, the cell assembly still requires improvements, mainly in assuring good contact between particles in order to avoid the deterioration caused by volume changes during cycling.

2.2. Na-Based Closo-Borates for Na Batteries

As mentioned previously, several issues affect the current use of LiBs, including the low natural abundance and its non-ubiquitous distribution in the Earth's crust which could be a source of political instability in the future [118]. Furthermore, it is already the case that rare elements involved in the LiBs industries, such as Co, are generating ecological problems and exacerbating social inequalities in developing countries [119].

Consequently, other chemistries for post-Li secondary batteries have been proposed. Sodium (Na) is a first reasonable choice due to its alkali nature, meaning that the overall chemical processes are virtually the same compared to LiBs. Compared to Li, Na is heavier, with a larger ionic radius and with a lower redox potential ($M^{\text{Na}} = 22.99 \text{ g mol}^{-1}$; $R^{\text{Na}+} = 1.13 \text{ \AA}$; $E_0^{\text{Na}} = -2.71 \text{ V}$ vs. standard hydrogen electrode (SHE) and $M^{\text{Li}} = 6.94 \text{ g mol}^{-1}$; $R^{\text{Li}+} = 0.73 \text{ \AA}$; $E_0^{\text{Li}} = -3.04 \text{ V}$ vs. SHE). Because of this, the established electrode materials for LiBs, in general, feature differently for Na-ion batteries (NiBs). However, the strength of NiBs will lie in cheap, robust and large-scale installations where output voltage and energy density are not ultimately crucial. As for LiBs, NiBs also rely on organic carbonate-based solvents for the liquid electrolyte and so comparable safety issues affecting LiBs remain valid for NiBs.

In the context of finding suitable solid-state electrolytes, the family of hydroborates, commonly known as borohydrides, has shown interesting properties in terms of ionic conductivity and density while they also possess advantageous mechanical properties [59,120]. Even so, safety concerns remain when dealing with the $[\text{BH}_4]^-$ anion. The larger cluster molecules and anions that are the decomposition products of the initial $[\text{BH}_4]^-$, so called *closo*-borates, are extremely stable and show a high ionic conductivity. The latter occurs after a structural phase transition that characterises their high-temperature phase. The electrochemical performance of these promising hydrides for Na-based batteries is discussed in more detail hereafter.

2.2.1. Na-Based Closo-Borates Solid Electrolyte

The $\text{Na}_2\text{B}_{12}\text{H}_{12}$ Polymorphism

The search for Na-based solid-state electrolytes by **Brighi et al.** was determined by the reduction of the high conductive phase transition temperature to below RT. The efforts were focused on the mixed $[\text{B}_{12}\text{H}_{12}]^{2-}/[\text{CB}_{11}\text{H}_{12}]^-$ system. The reason lies in the wide oxidative limits of such anions (4.1 and 5.1 V vs. Na^+/Na , respectively) [121] and in their geometrical affinity, giving them the possibility to form a solid solution in which the Na-vacancy content can be tuned according to the anion ratio, leading to a high-symmetry disordered-structure, known to be a crucial parameter in ionic conductivity [122].

Four distinct polymorphs of $\text{Na}_2\text{B}_{12}\text{H}_{12}$ were reported when studying the temperature-induced phase transitions [123,124], which also included a cubic closed packed (*ccp*) branch [125]. The in situ SR-XPD data in Figure 9a show the polymorphism as a function of temperature.

The RT monoclinic phase, in which all ions are ordered, splits at approximately the same temperature ($\sim 242 \text{ }^\circ\text{C}$) into a body centered cubic (*bcc*) and *ccp* branch, which is representative of an equilibrium state characterized by a very small energy difference separating the two polymorphs. While *ccp* is stable in the s.g. $Fm\bar{3}m$, the *bcc* branch evolves transferring thermal energy into the lattice dynamic, increasing the disorder and the symmetry, causing the transition of $Pm\bar{3}n \rightarrow Im\bar{3}m$ [126,127].

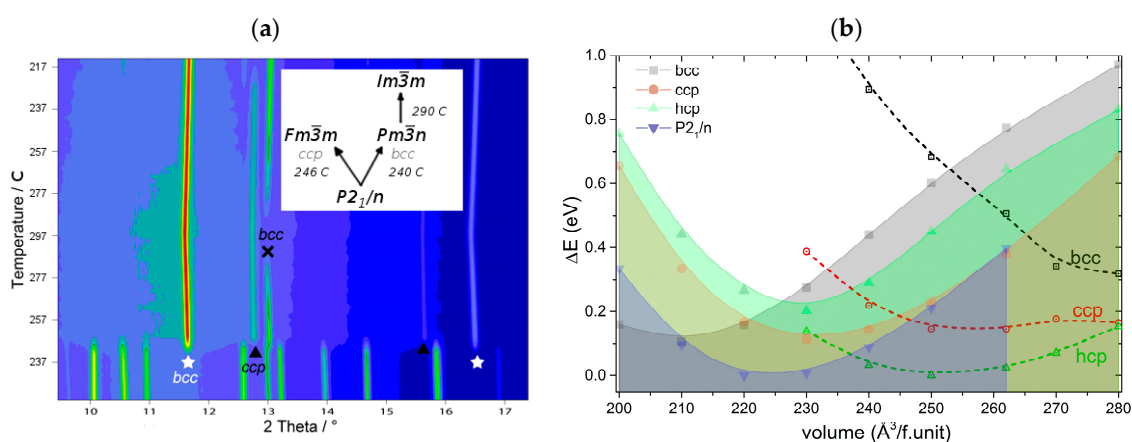


Figure 9. (a) Experimentally observed phase evolution of $\text{Na}_2\text{B}_{12}\text{H}_{12}$. The two branches corresponding to different anion lattices are shown in the inset. (b) Calculated ground state energy differences of different anion packing variants and volume per unit formula. Data for $\text{Na}_2\text{B}_{12}\text{H}_{12}$ are presented with the shaded region, $\text{Na}_2\text{B}_{12}\text{H}_{11}\text{I}$ are shown with the dashed lines. Adapted with permission from Sadikin, Y., P. Schouwink, M. Brighi, Zbigniew, and R. Cerny, Modified Anion Packing of $\text{Na}_2\text{B}_{12}\text{H}_{12}$ in Close to Room Temperature Superionic Conductors. *Inorganic Chemistry*, 2017. 56(56): pp. 5006–5016. Copyright (2017) American Chemical Society.

The coexistence of the two lattice packing variants is supported by DFT. Figure 9b shows the calculated ground state lattice energy as a function of unit cell volume for different packing types (shaded regions). Despite the global minima, represented by the monoclinic phase (s.g. $P2_1/n$), the *bcc* and *ccp* structures are very close in energy and are separated by $20 \text{ \AA}^3/\text{formula unit}$ (f.u.). Surprisingly, this matches the experimental observations quite well with the *ccp* density being higher than *bcc* (280 and $262 \text{ \AA}^3/\text{f.u.}$ at $262 \text{ }^\circ\text{C}$). In all simulated structures, sodium ions are off-centered from tetrahedral interstitial sites, forming a disordered structure, which is a sign of facile Na diffusion [128].

The mentioned high degree of Na disorder plays a crucial role for ionic conductivity, which jumps from 10^{-4} to nearly 0.1 S cm^{-1} at $267 \text{ }^\circ\text{C}$ for $\text{Na}_2\text{B}_{12}\text{H}_{12}$ after the first phase transition [123].

Despite the operating temperature being far above the desired one for RT applications, a minor modification of the anion cage considerably improves the performance of such a material. Indeed considering the heterovalent substitution of $[\text{B}_{12}\text{H}_{12}]^{2-}$ with $[\text{CB}_{11}\text{H}_{12}]^-$, the RT orthorhombic polymorph of $\text{NaCB}_{11}\text{H}_{12}$ (s.g. $Pca2_1$) transforms to the high symmetry *ccp*-type lattice at $107 \text{ }^\circ\text{C}$, with a resulting Na^+ conductivity of 0.12 S cm^{-1} [129].

$\text{Na}_{x+2y}(\text{CB}_{11}\text{H}_{12})_x(\text{B}_{12}\text{H}_{12})_y$ Solid Electrolyte

As presented in the previous section, $\text{Na}_2\text{B}_{12}\text{H}_{12}$ represents an interesting backbone to host high-Na mobility. Indeed, Figure 9b shows how closely related different packing types like *bcc* and *ccp* are, suggesting that a little modification could stabilise one of those packing variants. In this context, the partial replacement of the divalent $[\text{B}_{12}\text{H}_{12}]^{2-}$ for the monovalent $[\text{CB}_{11}\text{H}_{12}]^-$ would leave the anionic size unchanged but would affect the Na content, i.e., the ion–ion interaction. Three nominal compositions of $x\text{NaCB}_{11}\text{H}_{12} + (1-x)\text{Na}_2\text{B}_{12}\text{H}_{12}$ ($x = 1/3, 1/2$ and $2/3$) were mixed by ball milling to obtain $\text{Na}_{2-x}(\text{CB}_{11}\text{H}_{12})_x(\text{B}_{12}\text{H}_{12})_{1-x}$; the structural characterization was obtained by SR-XPD by Brighi et al. [130]. The structure with sample composition $x = 1/2$ (Figure 10), was solved in the s.g. $I23$ with lattice parameter $a = 7.98 \text{ \AA}$ at RT and with a *bcc* anion sublattice. Na is disordered around the tetrahedral sites. A tetrahedral setting should per definition be lower in energy than an octahedral one for the Na^+ cation [131], when coordinated by *closo*-borates. However, the Na–Na repulsion in the *bcc* stabilizes off-centered tetrahedral positions due to the shorter distance of 2.83 \AA and 3.99 \AA between tetrahedral and octahedral sites, respectively. The suggested model shown for the composition $x = 1/2$ in Figure 10 agrees with this hypothesis.

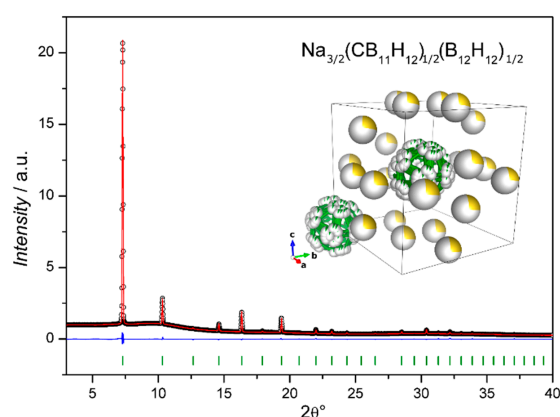


Figure 10. SR-XPD pattern and structure model for the composition $x = 1/2$. Na atoms are shown as yellow spheres, which are partially filled according to the site's occupancy, the green spheres show boron atoms and hydrogen is omitted for reasons of clarity. Reprinted from Brighi, M., Murgia, F., Łodziana, Z., Schouwink, P., Wołczyk, A., Cerny, R. A mixed anion hydroborate/carba-hydroborate as a room temperature Na-ion solid electrolyte. *Journal of Power Sources*, 2018. 404. Copyright (2018), with permission from Elsevier.

The $I23$ structure remains stable at RT for composition $x = 2/3$ while for $x = 1/3$, this configuration becomes unstable as the temperature increases. For the latter, a first phase transition to the s.g. $Pm\bar{3}n$ was observed at $T = 63\text{ }^{\circ}\text{C}$ and at $T = 193\text{ }^{\circ}\text{C}$. First, the dynamic anion disorder increases and secondly, the symmetry increases again owing to the re-appearance of the body-centered symmetry in s.g. $Im\bar{3}m$ (as followed by the polymorphism of the bcc branch of $\text{Na}_2\text{B}_{12}\text{H}_{12}$) [124].

The Arrhenius plot in Figure 11a summarizes the ionic conductivity (measured by EIS) [130] of the mixed-anion compounds compared to the respective precursors (Figure 11b) [123,129,132]. At RT, for $x = 2/3$, the Na^+ mobility is in the mS cm^{-1} range, and above $60\text{ }^{\circ}\text{C}$, approaches the superionic regime with $>10^{-2}\text{ S cm}^{-1}$. In this temperature range, a low activation energy $E_a = 314\text{ meV}$ was determined from $\sigma = \sigma_0 T^{-1} \exp(-E_a/kT)$, known as the Arrhenius relation. When the composition reaches the value of $x = 1/2$, the ionic conductivity remains constant while the activation energy slightly increases to $E_a = 367\text{ meV}$.

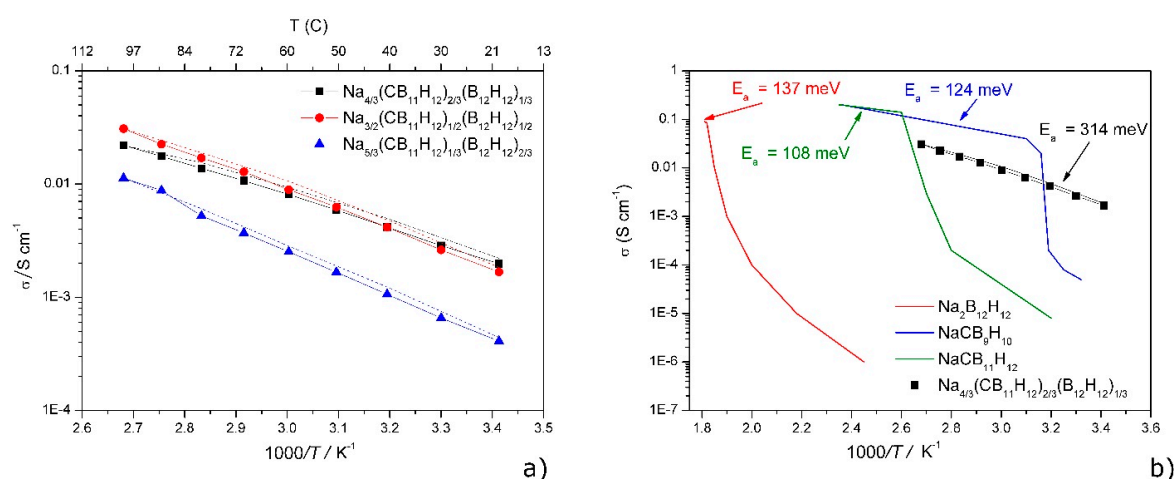


Figure 11. Plots after the Arrhenius relation for (a) Na^+ conductivity of $\text{Na}_{2-x}(\text{CB}_{11}\text{H}_{12})_x(\text{B}_{12}\text{H}_{12})_{1-x}$ in the range of $20\text{--}100\text{ }^{\circ}\text{C}$ and (b) different *closo*- and *carba-closo*-borates Na-conductors, with their respective activation energies in the superionic regime. Reprinted from Brighi, M., F. Murgia, Z. Łodziana, P. Schouwink, A. Wołczyk, and R. Cerny, A mixed anion hydroborate/carba-hydroborate as a room temperature Na-ion solid electrolyte. *Journal of Power Sources*, 2018. 404. Copyright (2018), with permission from Elsevier.

This trend is established for higher Na-contents (composition $x = 1/3$) with a conductivity drop of almost one order of magnitude at RT and an increase in the activation energy ($E_a = 409$ meV).

For the latter composition, at nearly $T = 90$ °C, where the symmetry changes to s.g. $Pm\bar{3}n$, the ionic conductivity progresses notably, confirming the transition observed by SR-XPD. This tendency of Na mobility can be explained in terms of vacancy population that increases by the substitution for a monovalent anion, as in the case for $x = 2/3$ and $1/2$.

Hence, the same conduction mechanism suggested for the high-temperature phase of $\text{Na}_2\text{B}_{12}\text{H}_{12}$, i.e., cation jumps between T-sites of *bcc* anion packing, applies to these compounds as well, similarly to other *bcc* superionics such as $\alpha\text{-Ag}_2\text{S}$ and $\alpha\text{-AgI}$ [122]. The electrochemical stability of composition $x = 2/3$ was investigated with cyclic voltammetry (CV) at 60 °C (scan rate of 0.5 mV s $^{-1}$) and is presented in Figure 12. The cell is composed as follows: $\text{Na}|\text{Na}_{2-x}(\text{CB}_{11}\text{H}_{12})_x(\text{B}_{12}\text{H}_{12})_{1-x}|\text{Na}_{2-x}(\text{CB}_{11}\text{H}_{12})_x(\text{B}_{12}\text{H}_{12})_{1-x} + \text{carbon black}|\text{Au}$ with Na as self-referenced counter electrode and Au as the working electrode. There is, however, an additional layer, composed by a mixture of solid electrolyte and carbon black that was used to amplify the low current signal by increasing the interfacial contact and improving the signal-to-noise ratio. This last modification allowed us to detect an anodic peak with the onset at 4.1 V vs. Na^+/Na (Figure 12 inset), which keeps this compound in a suitable electrochemical window of 0–4 V vs. Na^+/Na .

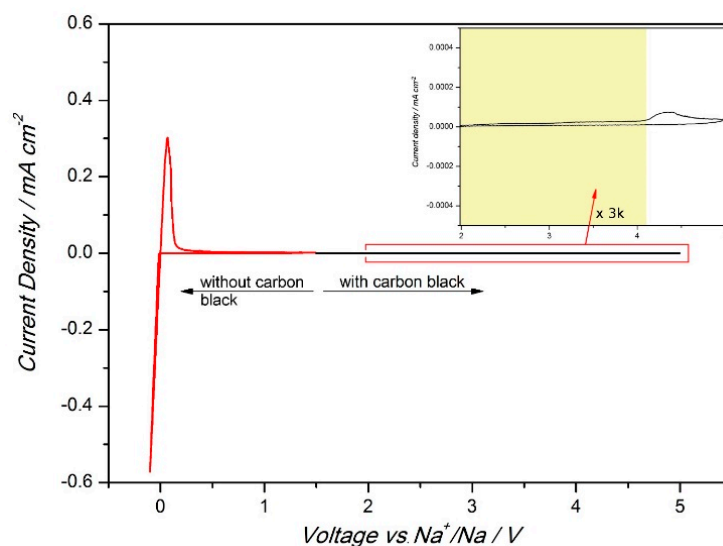


Figure 12. Cyclic voltammetry at a scan rate of 0.5 mV s $^{-1}$ for composition $x = 2/3$. Au and Na disks were used as working and counter/reference electrodes, respectively, for the voltage region $-0.1 < V < 1.5$ vs. Na^+/Na , indicated by the red curve. The black curve refers to the complementary CV, where a graphite layer was added to the solid electrolyte body ($1.5 < V < 5$ vs. Na^+/Na). Sodium plating (negative current density) and stripping (positive current density) are represented by the ohmic behaviour in the vicinity of the Na^+/Na redox potential (0 V). Reprinted from Brighi, M., F. Murgia, Z. Łodziana, P. Schouwink, A. Wołczyk, and R. Cerny, A mixed anion hydroborate/carba-hydroborate as a room temperature Na-ion solid electrolyte. *Journal of Power Sources*, 2018. 404. Copyright (2018), with permission from Elsevier.

To test the long-term reversible plating/stripping vs. metallic Na, a pellet of $\text{Na}_{4/3}(\text{CB}_{11}\text{H}_{12})_{2/3}(\text{B}_{12}\text{H}_{12})_{1/3}$ ($x = 2/3$) was sandwiched between two Na disks. Figure 13 shows the electrochemical behaviour of such cell at RT for over 500 h and two figures as magnifications on regions 20–25 and 300–305 h for better comparison.

After an open circuit voltage (V_{OC}) period of 5 h, a current density of ± 25.5 $\mu\text{A cm}^{-2}$ was alternatively applied for 30 min. The repeated plating/stripping occurs with a steady and limited

polarization, starting from ± 8.5 mV that further decreases, stabilising around ± 6 mV towards Na^+/Na . The electrolyte was stable towards Na metal for more than 500 operating hours.

2.2.2. Conclusions

The future class of solid electrolyte needs to fulfil several requirements, such as fast ionic conductivity, low density, non-toxicity, high thermal and electrochemical stability, but also, from a processing point of view, it should be highly ductile. Borohydrides are not the Holy Grail of all-solid-state batteries, but at the same time, satisfy many of the above-mentioned needs. In this context, another mixed-anion developed by Duchêne et al., $\text{Na}_2(\text{B}_{10}\text{H}_{10})_{0.5}(\text{B}_{12}\text{H}_{12})_{0.5}$ [133], was used as proof-of-concept for a 3 V all-solid-state NiB, showing high performances. The mixed-anion $\text{Na}_{2-x}(\text{CB}_{11}\text{H}_{12})_x(\text{B}_{12}\text{H}_{12})_{1-x}$ described here was shown to be stable against metallic Na operating more than 20 days with stable interfaces under Na plating/stripping. A further characterization spanning the entire range of current density up to 1 mA cm^{-2} is still necessary to determine whether dendrite penetration can be avoided (since in general having a solid material is not a sufficient condition) [134–136]. Nevertheless the achievements summarized herein put $\text{Na}_{2-x}(\text{CB}_{11}\text{H}_{12})_x(\text{B}_{12}\text{H}_{12})_{1-x}$ as a valid competitor with other solid electrolytes like oxides and thiophosphates.

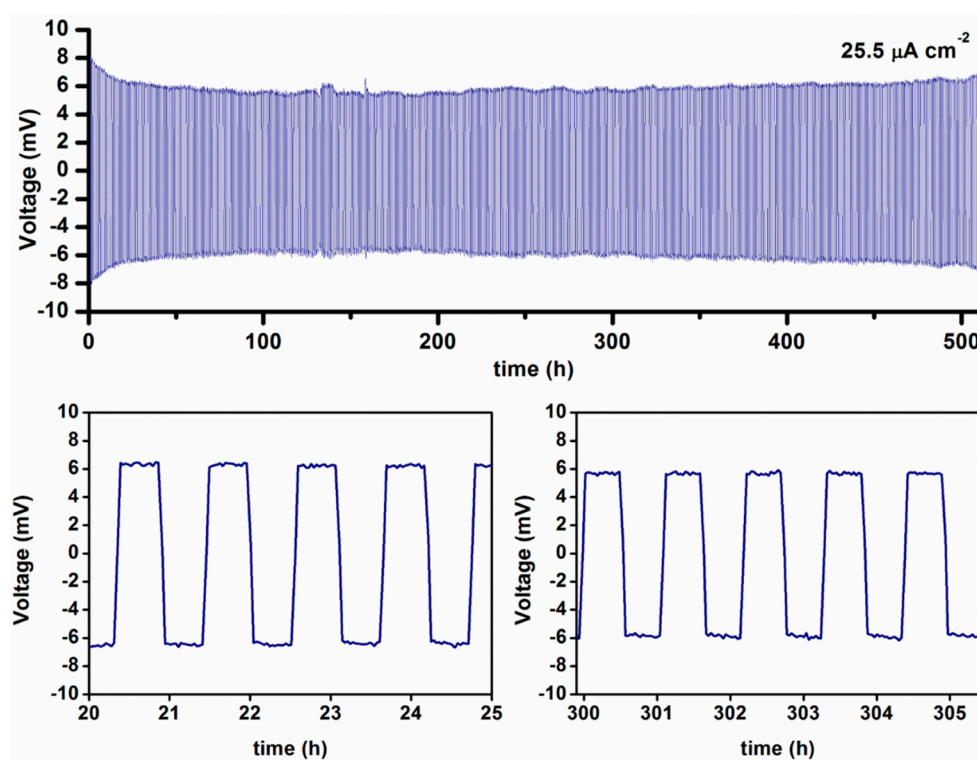


Figure 13. Galvanostatic profile of the $\text{Na}|\text{Na}_{4/3}(\text{CB}_{11}\text{H}_{12})_{2/3}(\text{B}_{12}\text{H}_{12})_{1/3}|\text{Na}$ cell, RT, 30-min sweeps. A focus on two magnifications on regions 20–25 and 300–305 h is given for better comparison. Reprinted from Murgia, F., Brighi, M. and Černý, R. *Electrochemistry Communications Room-temperature-operating Na solid-state battery with complex hydride as electrolyte. Electrochemistry Communications*, 2019. 106(August): p. 106534. Copyright (2019), with permission from Elsevier.

3. Advances in Hydrogen Storage Materials

In the last decade, substantial effort has been concentrated on using hydrogen as a fuel and energy carrier. Finding the safest conditions for large volumes of hydrogen has been, nevertheless, a challenge. Compared to the conventional compressed and cryogenic hydrogen storage, the storage of hydrogen in the solid-state chemically bonded to other compounds to form the hydrides and hydride-based

systems appears to be more suitable because the hydrogen pressure and temperature employed in this storage approach are milder than those required for compressed and cryogenic hydrogen storage. High volumetric and gravimetric hydrogen capacity, fast hydrogenation and dehydrogenation, full reversibility, low thermodynamic stability and low cost are the main parameters to be considered when studying a material with regards to its potential as a hydrogen storage source. In this part of the review, recent advances and perspectives on the different hydride categories, such as metal hydrides, complex hydrides, reactive hydride composites and rare earth complex hydrides, as well as their properties kinetically tailored by several approaches, i.e., the use of additives and confinement into a nanoporous scaffold, are discussed.

3.1. Pure Metal Hydrides (Mg, Pd, Ti)

One of the most promising materials belonging to the pure metal hydrides is magnesium (Mg) and its hydride (MgH_2) [137,138]. Despite its many advantages, the formation of this hydride creates an exothermic reaction with an enthalpy of $\Delta H_0 = -75 \text{ kJ mol}^{-1}$ of H_2 and an entropy of $\Delta S_0 = -133 \text{ J mol}^{-1}$ of H_2 [139]. The high stability of this hydride consequently raises problems in reversibility while the decomposition temperature is too high for desired industrial applications ($\approx 300 \text{ }^\circ\text{C}$ instead of the desired $\leq 100 \text{ }^\circ\text{C}$) [140].

Alloying with transition metals (TM) and changing of the composition as well as nanostructuring are a few of the methods reported to improve the properties of hydrides [141–144]. The use of palladium (Pd) as a catalyst in the MgH_2 formation has been shown to be essential [145–149]. To date, a system has not yet been found that monitors the industrial requirements and considerable effort is still invested for improving this material [150,151].

While powders are often investigated, thin films offer a more precise tool when focusing on the kinetics and the mechanism of diffusion in a system. An additional requirement for a quantitative evaluation of transport coefficients is an appropriate characterization of thermodynamic driving forces. In Mg, the equilibrium pressure of hydrogen has been reported since 1960 and an equilibrium pressure of 12–22.6 bar at temperatures of 380–410 $^\circ\text{C}$ has been identified [152–154]. Significant work on thin films has been conducted by Mooij et al. [155,156], who established a nucleation and growth mechanism while exploring hydrogenation at low pressures of 0.7 mbar in 10 nm thin Mg films that offer practically a 2D reaction geometry. By optical transmission microscopy, the growth of hydride islands was detected, which helped to establish a nucleation control. However, already at slightly higher pressures of 1.0 mbar, the islands could not be resolved any longer caused by a very high nucleation rate. X-ray diffractometry, electron and optical microscopy, Sievert apparatus and theoretical modeling are the main tools for hydride investigations. In systems, such as Mg and MgH_2 , the resistivity changes when hydrogen enters the metal. Such a setup is unavoidably challenging for high hydrogen pressures and wide ranges of temperature measurements. In 2005, Ingason et al. [157] reported resistance isotherms in a Mg system during hydrogen uptake. Moreover, Gharavi et al. [158] reported the resistance change in Mg thin films, additionally coated with a thin Pd layer, while focusing on the texture changes upon hydrogen loading and not on the kinetics of the system. Practical restrictions often hinder a simultaneous analysis of all parameters (temperature, pressure and time) with the use of one single apparatus. **Hadjixenophontos et al.** [159] suggested a way to fill that gap while studying the hydride formation by ex situ XPD and in situ resistance measurements in a wide range of parameters and demonstrated a linear to parabolic kinetic transition. By subsequently defining a resistivity model to their experimental results that considers this transition, they could quantitatively evaluate the kinetic parameters of diffusive transports through the hydride. They reported the linear growth constant obtained in the early stages at 200 $^\circ\text{C}$ to be equal to $\kappa = 6.6 \times 10^{-9} \text{ cm}\cdot\text{s}^{-1}$. Measurements in a wide temperature range from RT to 300 $^\circ\text{C}$ yield an Arrhenius behaviour with an activation energy $E_a = 28.1 \text{ kJ}\cdot\text{mol}^{-1}$ [159] and comparisons can be found in [160–162]. With supplementary investigations and calculations, this low activation energy, the described small grain size of 17 nm and

the comparison to theoretical predictions of bulk diffusion led to the conclusion that grain boundary diffusion is the main transport mechanism [159].

Grain boundaries and detailed microstructure changes in thin films are better visible in TEM micrographs. **Hadjixenophontos et al.** [163] showed that during hydrogenation of Mg, the hydride is immediately formed at the interface between the coating of Pd catalyst and the Mg thin film. The Mg hydride grows in a layer-like reaction towards the substrate. FIB used for preparation of cross sectional observations destroys the hydride phase but the microstructure change is nonetheless clear with an alteration from a columnar grain structure of freshly deposited pure Mg thin film to an equi-axed grainy structured film when the hydride is formed. Electron microscopy has been reported to irreversibly damage the hydride phase [164]. It can be used to follow the hydrogenation kinetics and the MgH₂ layer growth not only in thin films but in powders as well.

Pd does not only bring advantages to the system but also some difficulties. Looking at the phase diagram of the Mg-Pd system [146] at fairly high temperatures of hydrogen loading (200 °C) and unloading (300 °C), intermetallic phases Mg₅Pd₂ and Mg₆Pd are formed. Kumar et al. [165] reported the hydrogenation of Pd/Mg films at almost ambient temperatures (50–150 °C) that rapidly declined in the third cycle despite the fact that Pd appears stable at those conditions. This observation suggests that the Pd/Mg interface may not be stable and hinders the hydrogen transport. Reddy et al. [166] studied the formation of Pd-Mg intermetallics in thin films (at 200 °C) and presented the Mg₅Pd₂ and Mg₆Pd phases by XPD. Further cycling of their films was not discussed. **Hadjixenophontos et al.** [159] demonstrated, also in thin films, that further de-hydrogenation and re-hydrogenation were possible regardless of the intermetallic reactions at the Mg/Pd interface. The formed phases were detected by TEM micrographs to form a very dense layer close to the surface and consumed the Pd layer over time.

Replacement of Pd on top of Mg films is a bit more challenging since many elements are miscible with Mg, but due to the high cost of Pd, alternatives are of high interest. Researchers have demonstrated that it is possible to improve the performance of Mg and its hydride by adding transition metals [140] such as Iron (Fe) [167], Chromium (Cr) [168], Nickel (Ni) [144,169], Titanium (Ti) [143,170–172], Niobium (Nb) [173] and many others. Further investigations have been completed on merging the benefits of carbon materials for tuning MgH₂ hydrogen properties [174]. Recently, MgCNi₃ has also shown an important catalytic additive behaviour with its anti-perovskite structure [175]. Titanium, while being promising and immiscible with Mg, needs to be handled with care since the native oxide formed on top has been shown to control the hydrogenation. **Hadjixenophontos et al.** [164] reported a linear kinetic regime observed when hydrogenating TiO₂/Ti/Mg films and showed a growth constant at 300 °C and 20 bar H₂, of $\kappa = 10^{-10} \text{ cm s}^{-1}$. Additional measurements in a wide range of temperatures (25 °C–300 °C) and pressures (from 5×10^{-5} bar up to 100 bar H₂) revealed a plateau rate at about 1 bar H₂. The authors suggested that above this pressure, a full coverage of the oxide surface from hydrogen atoms occurs [164]. Additionally, the diffusion through the oxide is very slow and this hinders further hydrogen movement into the sample. Attributed to this oxide effect, hydrogenation performance decreases at higher pressures.

Based on the fact that light materials perform significantly better for hydrogen storage applications, the ternary system Li-Mg-Si has been reported to form promising intermetallic phases. Pavlyuk et al. [176] gave a complete structural report on seven ternary compounds that can be found in this system while additionally testing their hydrogenation properties. The ternary alloy with the Li-rich phase Li₇₀Mg₁₀Si₁₀ is shown to absorb the highest amount of hydrogen (8.8 wt.%) with a desorption temperature between MgH₂ and LiH.

Conclusively, Mg and its hydride stay under the radar of research investigations due to the dominant benefits they offer. However, the system lacks efficiency for industrial applications and a great effort is given on improving it or finding alternative systems that are more complex.

3.2. Amide and Imide Based Systems for H₂ Storage

Complex metal hydrides made from light elements, such as lithium, boron, nitrogen, or aluminium very often have particularly high hydrogen densities while poor thermodynamic and kinetic properties as well as limited reversibility are drawbacks. The chemistry of complex metal hydrides is exceptionally diverse. Many novel materials have been provided. In this respect, amides of alkali and alkaline-earth metals in combination with metal hydrides have the potential to meet the needs of on-board hydrogen storage for electric vehicles powered by fuel cells due to their high hydrogen capacity and tuneable thermodynamics [177]. A large number of amide–hydride and amide–complex hydride materials have been developed and studied in recent years [178]. Nevertheless an amide-based composite with suitable hydrogen capacities, favourable thermodynamics and decent kinetics is still a challenging mission. The first task is to accomplish a favourable thermodynamic stability, to realize hydrogen storage at moderate temperatures. Secondly, ammonia (NH₃) is an unwanted by-product which degrades the fuel cell by a loss of contact between the Pt/C-catalyst and the membrane [179]. Therefore, preventing NH₃ release needs to be addressed and filters are necessary to prevent the aforementioned membrane degradation. Thirdly, amide–hydride composites suffer from sluggish kinetics for the hydrogenation and de-hydrogenation reactions. The barriers for the kinetics are primarily a result from the mass transport and from reactions, which occur at the interface. Reducing particle size for instance by ball milling or nanoconfinement and mixing additives into the hydrogen storage materials are all effective ways to improve kinetics [180].

Research in this field started in 2002, with the first characterization of the hydrogen storage properties of the LiNH₂-LiH composite system [181]. Li₃N was reported to reversibly store more than 9 wt.% of hydrogen in a two-step process, which can be described according to the following reactions in Equations (2) and (3):



The net reaction for the complete absorption process thus becomes:



Despite its high gravimetric capacity, the reaction enthalpy of the Li-N-H system has been reported to still be too high, measured to be 66 kJ mol⁻¹ H₂ only for the first step [181], while the reported reversible hydrogen capacity has later been revised to 5.2 wt.% [182].

Many attempts to modify the composite system in order to decrease the reaction enthalpy have followed. The most successful approach was the partial replacement of Li with Mg [183–187]. In particular, of the many different compositions explored within the Li-Mg-N-H system, the Mg(NH₂)₂ + 2LiH composite showed the lowest sorption temperatures and a promising low reaction enthalpy (38.9 kJ mol⁻¹ H₂) [188,189]. The thermodynamics of the system allowed predicting 1 bar of hydrogen pressure at a temperature as low as 90 °C. Experimentally however, this result has never been achieved due to kinetic limitations.

3.2.1. Insights into Alkali-Based Amides and Imides Including Boron

In the first part of this chapter, insight into binary systems that combine lithium borohydride, amide and imide are presented, discussing their improved thermodynamics, new structures, phase diagrams and hydrogenation properties. The second part gives an overview of recent insights into the ammonolysis of alkali and alkaline-earth metal amides, in the hydrogen storage and structural properties of K-Mg-N-H, KNH₂-KH, Rb-Mg-N-H and Rb-N-H systems. The chapter ends with a comprehensive summary.

LiBH₄-LiNH₂

It has been evidenced that composite systems containing lithium borohydride (LiBH₄) [190], or mixture of borohydrides, or borohydrides and reactive hydride composites, have improved hydrogen storage properties, especially when a liquid phase is involved [191]. Furthermore, varying composition and crystal structure can lead to a fine-tuning of kinetics and thermodynamics of hydrogen storage properties as a function of temperature, pressure and phase stability. The full thermodynamic optimisation and assessment of LiBH₄ opens the way for new studies of more complex systems (i.e., binary mixtures, eutectic borohydrides) [192].

The gravimetric and volumetric hydrogen density of LiBH₄ is very high at 18.4 wt.% H₂ and 122.5 g H₂ L⁻¹, respectively [56]. As discussed in the battery chapter of this review (Figure 4), the structure of LiBH₄ is orthorhombic (s.g. Pnma), here denoted o-LiBH₄, at RT whereas a first-order polymorphic transition into a hexagonal structure (s.g. P63mc), denoted h-LiBH₄, occurs at T ~115–117 °C [193]. Both polymorphs comprise of regular, relatively rigid and undistorted BH₄⁻ tetrahedra. LiBH₄ is known to melt at T ~280 °C and decomposes at temperatures > 350 °C into LiH and elemental B where the enthalpy change of decomposition (ΔH_{dec}) is 74 kJ mol⁻¹ H₂ [194]. The crystal structure of LiNH₂ was investigated by employing neutron powder diffraction (NPD) [195]. LiNH₂ crystallizes in the tetragonal s.g. $\bar{1}4$ with unit cell parameters of $a = 5.03442(24)$ Å, $b = 5.03442(24)$ Å, $c = 10.25558(52)$ Å [195].

The LiBH₄-LiNH₂ system has been extensively investigated in a wide composition range by means of different synthesis routes (i.e., ball milling, annealing treatment and quenching from liquid phase). Wołczyk et al. [71] reported a detailed examination of the phase stability combining experimental techniques, ab initio calculations and CALPHAD assessment to fully determine the equilibrium pseudo-binary LiBH₄-LiNH₂ phase diagram (Figure 14). In detail, this system consists of two compounds: Li₂BH₄NH₂ has been reported to be metastable and Li₄BH₄(NH₂)₃ presents peritectic melting [71]. DFT calculations on LiBH₄, LiNH₂, Li₂BH₄NH₂ and Li₄BH₄(NH₂)₃ gave good agreement between experimental [196,197] and optimized structures [71]. The optimized geometries of Li₂BH₄NH₂ and Li₄BH₄(NH₂)₃ were found to have lower energy than the mixtures LiBH₄ + LiNH₂ and LiBH₄ + 3LiNH₂, by 6.6 and 13.9 kJ mol⁻¹, respectively. Previously, Herbst et al. [198] reported a lower energy of reaction equal to 6 kJ mol⁻¹ for Li₄BH₄(NH₂)₃; however, the new determination by Wołczyk et al. fits reasonably well with the value obtained by Siegel et al. [199] at 0 K (11.3 kJ mol⁻¹). Calculations of Li₂BH₄NH₂ geometries have not been reported in the literature yet [200]. It is believed, however, that the Li₄BH₄(NH₂)₃ is much denser. The thermodynamic assessment of the system shows that the formation reaction of Li₂BH₄NH₂ from LiBH₄ and Li₄BH₄(NH₂)₃ has a slightly more positive energy value, thus being a metastable compound.

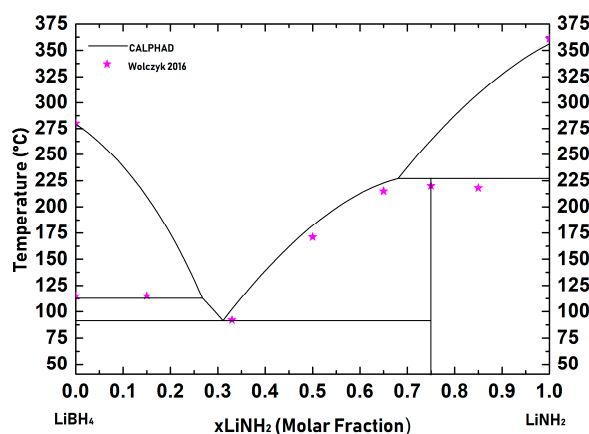


Figure 14. Calculated LiBH₄-LiNH₂ pseudo-binary phase diagram (solid lines). Experimental data (pink stars) are reported for comparison.

The unit cells of LiBH_4 , LiNH_2 , $\text{Li}_2\text{BH}_4\text{NH}_2$ and $\text{Li}_4\text{BH}_4(\text{NH}_2)_3$ contain 4, 8, 18 and 8 molecules, with 3, 2, 6 and 4 sets of non-magnetically equivalent hydrogen atoms having a relative abundance of 4:4:8, 8:8, 6:6:6:6:6:6 and 24:24:24:8, all respectively. Gauge Including Projector Augmented Waves (GIPAW) calculation of chemical shifts outlines a good agreement between the measured experimental and the weighted average value of computed chemical shift for each crystal structure. The calculated pseudo-binary phase diagram, according to the CALPHAD approach (Figure 14), shows good agreement with the literature [201,202] and new experimental and calculated data [71].

While neglecting entropy variations, the Gibbs free energy of $\text{Li}_4(\text{BH}_4)(\text{NH}_2)_3$ has been determined through ab initio calculations for the reaction in Equation (5) [199]:



The Gibbs free energy of the liquid phase, including new experimental temperature and enthalpy of melting for pure LiNH_2 obtained in Reference [71], is equal to $T_m = 357 \text{ }^\circ\text{C}$ and $\Delta H_m = 14.3 \text{ kJ mol}^{-1}$. Considering a regular solution model to describe the liquid mixture between LiNH_2 and LiBH_4 , a negative interaction parameter, $\Omega_{\text{liquid}} = -13.0 \text{ kJ mol}^{-1}$, was obtained from the assessment. As already reported previously and according to recent experimental information [203,204], the $\text{Li}_2\text{BH}_4\text{NH}_2$ compound is metastable and therefore, it is not present in the stable phase diagram.

The reactions of LiNH_2 and complex hydrides, including LiBH_4 , show a number of interesting features. It was reported that more than 11 wt.% hydrogen can be desorbed (endothermic reaction) from a mixture of $2\text{LiNH}_2 + \text{LiBH}_4$ in the temperature range $250\text{--}350 \text{ }^\circ\text{C}$ [205]. In conclusion, these materials have an outstandingly rich chemistry, which is based on their structural flexibility and additionally, a wide range of elemental compositions [194].

$\text{LiNH}_2\text{-Li}_2\text{NH}$

The first to study binary systems based on $\text{LiNH}_2\text{-Li}_2\text{NH}$ was by Chen et al. [181,206] in 2002. Originally, they suggested that H_2 release could take place at the LiNH_2/LiH interface via an acid-base reaction between $\text{H}^{\delta-}$ of LiH and $\text{H}^{\delta+}$ of Li amide. This mechanism, however, would require a very close contact between the two phases [207]. Furthermore, Miceli et al. [208] studied the binary $\text{LiNH}_2\text{-Li}_2\text{NH}$ system. The reaction rates and the diffusivity of different species in LiNH_2 and Li_2NH collected from their ab initio simulations provided for a microscopic scenario for the solid-state reaction in Equation (6):



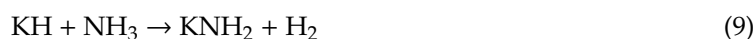
According to these ab initio calculations, the transformation path depends on the surface-to-volume ratio of the crystallites of LiNH_2 . NH_3 formation is stimulated by the presence of Li Frenkel pairs, as proposed by David et al. [74]; however, NH_3 formation is more likely to take place at the surface rather than in the bulk. Thus, it is expected that for small LiNH_2 particles, the transformation might be controlled by the surface. In this case, in the early stage of decomposition, the rate-limiting step is the formation of NH_3 supported by Frenkel pairs at the LiNH_2 surface. Once a shell of Li_2NH is formed, the rate-limiting step becomes the diffusion of H^+ in the Li_2NH product. Transfer of H^+/Li^+ across the $\text{LiNH}_2/\text{Li}_2\text{NH}$ moving interface and the formation of NH_3 from NH_2^- groups in Li_2NH are not rate limiting [208]. Shaw et al. [207] proposed a kinetic model in which a shell of Li_2NH grows from the surface while the core of LiNH_2 shrinks. However, for larger crystallites with small surface-to-volume ratio, NH_3 formation would take place in the bulk. In the presence of Frenkel pairs, this would happen at a higher pace due to the larger number of defects. However, the formation of Li_2NH in the bulk of LiNH_2 via the accretion of Li_2NH nuclei is anticipated by the diffusion of NH_2 species which might lead to the formation of the sub-stoichiometric phases reported by David et al. [74]. Miceli et al. [208] reported that the size dependence of the decomposition pathways might not be restricted to LiNH_2 but could be compared to other complex hydrides [208].

3.2.2. Insights into the Structure and Reaction Mechanism of Metal Amide—Metal Hydride Composite Systems

The effort for tailoring the amide–hydride composite system of Li and Mg (Li-Mg-N-H system) resulted in the discovery of two additives, KH and LiBH₄ [209,210]. In the KH-doped system the desorption temperature was lowered by 50 °C and it was possible to perform the dehydrogenation/re-hydrogenation at 107 °C under equilibrium conditions [210]. The addition of LiBH₄ allowed to desorb 5 wt % of H₂ at 140 °C and re-absorb the same amount of hydrogen at 100 °C [209]. A comprehensive summary on the effect of these additives and their practical application for hydrogen storage can be found in a recent review [177]. The next sub-chapters, concerning the ammonolysis of alkali and alkaline-earth metal amides and the K-Mg-N-H, KNH₂-KH, Rb-Mg-N-H and Rb-N-H systems, will present an overview of recent discoveries on some more fundamental aspects of amide–hydride systems.

Ammonolysis of Alkali and Alkaline-Earth Metal Amides

The first in situ SR-XPD study of the ammonolysis process of lightweight alkali and alkaline-earth metal hydrides showed clear evidence of the formation of previously unknown intermediates [211]. In fact, while for LiH and NaH, the formation of LiNH₂ and NaNH₂ starts to occur almost at RT, for KH, the formation of the RT polymorph of KNH₂ (monoclinic, P2₁/m) is not observed. Instead, isolated Bragg peaks appear almost at RT, which resemble the pattern of the cubic KNH₂ polymorph. However, the cubic polymorph of potassium amide should be stable only above 75 °C [212]. By increasing the temperature, the Bragg peaks of LiNH₂, NaNH₂ and the cubic KNH₂-like phase increased in intensity due to the continuation of the ammonolysis process, while the intensity of LiH, NaH and KH peaks decreased, as could be expected, hypothesizing that the ammonolysis process occurs according to the following reactions in Equations (7)–(9):



In fact, for the Li-based system, as well as for the Na-based system, the Bragg peaks of the solid phases involved in the process show a gradual shift to lower 2θ -values when the temperature increases, as it usually occurs owing to the thermal expansion of the crystal lattice. However, for the K-based system, the peaks of the cubic KNH₂-like phase gradually shift to higher 2θ -values when the temperature is raised above 160 °C, implying a counter-intuitive contraction of the cubic cell upon heating. Due to this observation, the authors suggested the possible formation of new K-N-H species with intermediate compositions [211].

Concerning the alkaline-earth metals, the most interesting piece of evidence, in view of hydrogen storage applications, is the partial formation of the high-pressure polymorph of γ -MgH₂ (tetragonal, P4₂/mnm) by ball milling pre-treatment of β -MgH₂ (orthorhombic, Pbcn) and its role in facilitating the ammonolysis process at lower temperatures. In fact, during the ammonolysis experiment, the formation of Mg(NH₂)₂ (starting at about 230 °C) occurs mostly with the consumption of the γ - polymorph rather than β -MgH₂. This fact might be helpful in order to optimize the synthesis process of Mg(NH₂)₂, which is an important component in many of the most promising amide–hydride systems.

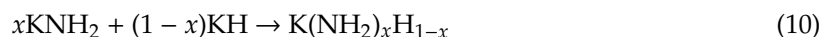
K-Mg-N-H System

The interaction of KH and Mg(NH₂)₂ has been shown to have a central role in lowering the desorption temperature of the KH-doped Mg(NH₂)₂ + 2LiH system [213]. Moreover, in the attempt to characterize the K-Mg-N-H phases involved, a new phase was discovered, a mixed

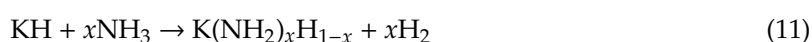
amide-imide phase: KMgNH_2NH [214,215]. However, none of the other bimetallic phases previously reported ($\text{K}_2\text{Mg}(\text{NH}_2)_2\text{NH}$, $\text{K}_2\text{Mg}(\text{NH})_2$ and KMgN) were found as reaction product, by ex situ XPD [214,216,217]. In order to clarify this aspect, the K-Mg-N-H system was studied by Santoru et al. [218] by in situ SR-XPD, confirming that no bimetallic phases were formed, in addition to $\text{K}_2\text{Mg}(\text{NH}_2)_4$ and KMgNH_2NH . For the $\text{KNH}_2 + \text{MgH}_2$ composite the K-Mg-N ratio was calculated in order to release all possible hydrogen forming the speculated bimetallic nitride, KMgN . However, even above 300 °C, this phase could not be formed. Mg_3N_2 was formed instead and the K-N-H containing phase melted and decomposed rather than interacting with Mg_3N_2 to form a bimetallic nitride. The $\text{Mg}(\text{NH}_2)_2 + \text{KH}$ composite led to the formation of KMgNH_2NH . In both systems; however, KH and KNH_2 reacted in an unexpected way, where with the progress of the reactions, their diffraction peaks gradually shifted in 2θ -scale rather than simply increasing or decreasing in intensity [218]. This behaviour was similarly reported for the ammonolysis process of KH, implying unexpected expansions and contractions of the cubic cell [211].

KNH_2 -KH System

A new study by Santoru et al. [219] closely examined the KNH_2 -KH system and confirmed the hypothesis previously reported, indicating the possibility of forming phases with intermediate amide-hydride compositions. In situ SR-XPD measurements were carried out under inert atmosphere on samples with different molar ratios of KNH_2 and KH. This series of experiments proved that in any case the two starting components react, forming two cubic phases that become more and more similar, until their Bragg peaks merge into a single set of reflections ascribable to a single cubic phase. In other words, an anionic exchange occurs between the cubic structures of the amide and hydride phase, until a phase with a single composition is reached at 270 °C. Moreover, it was revealed that the higher the initial content of potassium amide is, the larger the unit cell of the cubic phase formed. In the same study [219], NPD and ^1H solid-state (SS)-NMR measurements furnished additional proof of the formation of a metal amide/hydride solid solution. In view of these findings, the reaction of KNH_2 and KH can be generalized as



Moreover, the ammonolysis process of KH is better described by the following chemical reaction:



Rb-Mg-N-H and Rb-N-H Systems

The continuous effort to improve the hydrogen sorption properties of the already promising KH-doped Li-Mg-N-H system resulted in the testing of Rb-based additives [220–223]. This choice was prompted by the fact that K and Rb are both alkali metals with similar electronegativity and the ability to form ternary amides with Mg [220]. Rb-based additives were shown to be even better than the corresponding K-based ones in lowering the hydrogen desorption temperature of the composite. Moreover, the formation of a new RbMgNH_2NH phase responsible for a lower reaction enthalpy and lower activation energy, was inferred by stoichiometric considerations and Fourier transformed infrared data, but not directly proven by diffraction methods [222]. For these reasons, an effort was made to characterize the intermediates possibly involved in the desorption process from the structural point of view and RbMgNH_2NH was successfully synthesized, as confirmed in Santoru et al. [224]. Moreover, XPD and NPD measurements allowed to solve its crystal structure as an orthorhombic system, with s.g. $Pnma$ being isostructural with KMgNH_2NH [215,224]. Larger unit cell parameters were found, which could be expected taking into account the larger cation [224]. It is worth noticing that the use of CsH has been experimented recently [225–228] leading some authors to suggest the possible formation of a CsMgNH_2NH phase [227,228]. It would be interesting for further studies to focus on isolating this

compound in order to solve its structure and compare it to that of $\text{RbMgNH}_2\text{NH}/\text{KMgNH}_2\text{NH}$ while determine the respective similarities and differences.

Considering the novelty of these findings and the attested formation of $\text{K}(\text{NH}_2)_x\text{H}_{1-x}$ phases, both in the desorption process of the K-Mg-N-H system and during the synthesis of KNH_2 by ammonolysis of KH, the study expanded on the possibility of forming a Rb-based amide/hydride solid solution. A combination of in situ SR-XPD and ^1H SS-NMR confirmed that cubic phases with intermediate amide/hydride compositions, described as $\text{Rb}(\text{NH}_2)_x\text{H}_{1-x}$, were indeed formed by thermal treatment. Moreover, the $\text{Rb}(\text{NH}_2)_x\text{H}_{1-x}$ phases were formed even at RT after hand-grinding the pure RbNH_2 and RbH with an agate pestle and mortar [224].

3.2.3. Conclusions

During the exploration for novel materials for the storage of hydrogen, research interests have been focused on light metal borohydrides and amides as two characteristic chemical complex hydrides with very high hydrogen capacities. Mixed anion complex hydrides were discussed here, with a focus on the $\text{LiBH}_4\text{-LiNH}_2\text{-Li}_2\text{NH}$ system, which is shown to form a series of amide phases. Investigation on Li_2NH itself brought interesting results in terms of new structure determination and good ionic conduction as shown in Section 2.1.

Amide-hydride systems have shown to be particularly interesting, not only as promising candidates as hydrogen storage systems but also because they continue to provide novelty even in their fundamental aspects. In particular, the study of the ammonolysis process of alkali metals showed marked differences in how KNH_2 is formed as compared to LiNH_2 and NaNH_2 . In contrast to LiH and NaH, KH reacts with NH_3 , forming a novel amide-hydride solid solution. K-Mg-N-H and Rb-Mg-N-H systems present a striking similarity in their ability to form an isostructural bimetallic amide-imide phase which is involved in the lower reaction enthalpy and lower activation energy of a RbF-doped $\text{Mg}(\text{NH}_2)_2 + 2\text{LiH}$ system. The similarities in the chemistry of K and Rb is also evidenced in the formation of a rubidium amide-hydride solid solution with very similar properties to the K-based one and which can be formed even at RT. Since the kinetic barrier of metal amide/hydride composite arises from mass transport and reactions occurring at the interface, it is reasonable to suspect that the lower activation energy of K- and Rb-doped systems might be due, at least in part, to the possibility of forming amide/hydride phases with a continuous range of intermediate compositions. Nonetheless, looking at the structural similarities seems to be a reasonable strategy for finding new additives to improve hydrogen storage systems.

3.3. Eutectic Metal Borohydride Systems

The concept of eutectic in metallurgy specifies the formation of a homogenous liquid mixture from a mixture of substances in a defined composition at a given eutectic temperature [229]. The eutectic temperature is the lowest temperature among the melting points of all separate constituents. This phenomenon is not only observed in alloys but also in molten-salt mixtures. These molten-salts mixtures are generally good conductors for electric current, which is a consequence of their highly dissociated ionic species in the molten status [230]. They are useful as reaction media [231] as well as in extractive metallurgy [232]. Recently, Harries et al. and Paskevicius et al. proposed the employment of molten-salts and eutectic-borohydrides mixtures in solar thermal energy [233] and H_2 storage [234], respectively.

The low-melting-point borohydride mixtures are often denoted “eutectic metal borohydrides”, while these mixtures can lead to hydrogen desorption at relatively low temperatures [235,236]. Furthermore, the low melting point is beneficial for the nanoconfinement approach discussed in Section 3.5. [237–239]. Furthermore, these low melting point mixtures have been investigated as ionic liquids, aiming to provide convenient and fast re-fueling of hydrogen in electric vehicles powered by fuel cells [240,241].

The formation of eutectic borohydride mixtures from physically mixing pure borohydrides is summarized in Table 2, showing a H₂ release at lower temperatures than individual constituents [190]. The following chapter will focus and present experimental investigations of the reported systems, as well as their thermodynamics and hydrogen storage properties.

The use of eutectic borohydrides is strongly related to the stability of the liquid phase, as, for instance, alkali-metal borohydrides often melt before H₂ desorption starts. The dehydrogenation of borohydrides from the liquid state may lead to less [B₁₂H₁₂]²⁻ in the reaction products [242]. Thus, the characterization of their thermodynamic properties and decomposition mechanism is of fundamental importance [243–245].

Table 2. Eutectic borohydride systems. Temperature reported in [°C] for the melting point (mp) of individual constituents: T_{mp1}, T_{mp2} and T_{mp3}; melting point for eutectic mixture: T_{mp}; decomposition temperature: T_{dec}. Theoretical gravimetric hydrogen capacity: ρ_g reported in [wt %].

Systems	Constituents			Eutectic Mixture			Reference
	T _{mp1}	T _{mp2}	T _{mp3}	T _{mp}	T _{dec}	ρ _g	
0.62LiBH ₄ -0.38NaBH ₄	280	510	-	225	300	14.5	[237,246,247]
0.71LiBH ₄ -0.29NaBH ₄	280	510	-	219	n.a.	15.2	[247]
0.725LiBH ₄ -0.275KBH ₄	280	605	-	105	420	13.2	[238,245]
0.68NaBH ₄ -0.32KBH ₄	510	605	-	460	465	9.4	[248]
0.66LiBH ₄ -0.11NaBH ₄ -0.23KBH ₄	280	510	605	102	n.a.	13.0	[249]
0.55LiBH ₄ -0.45Mg(BH ₄) ₂	280	280	-	180	250	16.1	[244,250,251]
0.68LiBH ₄ -0.32Ca(BH ₄) ₂	280	370	-	200	350	14.5	[236,252]
0.45NaBH ₄ -0.55Mg(BH ₄) ₂	510	280	-	205	360	13.4	[252,253]

3.3.1. Experimental Study and Assessment of Eutectic Borohydride Systems

Low-melting point borohydrides are often prepared by ball milling [254]. During synthesis, cation or anion substitutions in borohydrides have been demonstrated to provide solid solutions [79,255–263], i.e., cationic or anionic fully disordered structures [263–266]. However, by mixing various light-metal borohydrides, the formation of bi-metallic and tri-metallic compounds was evidenced [190].

In the literature, it has been shown that binary combination of LiBH₄, NaBH₄ and KBH₄ undergo eutectic melting [245,247] or a thermal minimum [248]. Starting from available experimental values and ab initio calculation, the thermodynamic assessment and optimisation of binary systems allow the modelling of solid and liquid phases, leading to a description of the pseudo-ternary phase diagrams using the CALPHAD approach [267].

In the following section, binary and higher combination of borohydrides will be discussed in detail concerning their experimental studies and their thermodynamic assessment. Phase diagrams and hydrogen storage properties will be presented.

LiBH₄-NaBH₄

Among the known eutectic borohydrides, the eutectic mixture of LiBH₄-NaBH₄ has relatively low costs while the high theoretical gravimetric hydrogen storage capacity is preserved with 15 wt.%. To date, two eutectic compositions have been reported based on experimental and thermodynamic simulation methods: 0.62LiBH₄-0.38NaBH₄ with a melting point of 224 °C and 0.71LiBH₄-0.29NaBH₄ with a melting point of 216 °C [235,246,247].

In 1961, Adams [268] proposed a partial pseudo-binary LiBH₄-NaBH₄ phase diagram, describing the system as eutectic and reporting experimental liquidus points for mixtures which are rich in LiBH₄. However, the experimental method used for their determination was not reported. In 1971, Semenenko et al. [269] reported the pseudo-binary phase diagram by coupling thermographic and X-ray studies on annealed samples. The system was characterized without any eutectic point, but it was described by the formation of solid solutions, including a miscibility gap and

a minimum melting temperature at a similar composition, as previously proposed by Adams, i.e., eutectic (0.62LiBH₄-0.38NaBH₄) [269]. It is worth noting that solid solutions of LiBH₄-LiI exhibits a fast-ion conduction, owing to the stabilisation of the hexagonal structure of LiBH₄ at RT [75,77,79,257,260–262,264,270], as described in Section 2.1.

The LiBH₄-NaBH₄ system (Figure 15) was recently studied experimentally and assessed by Dematteis et al. [247], showing the formation of solid solutions on both Li and Na rich side with an eutectic melting at 216 °C for the composition 0.70LiBH₄-0.30NaBH₄. In this system, the polymorphic transition of o-LiBH₄ to h-LiBH₄ structure was observed at 95 °C, which is 20 °C lower than that for pure LiBH₄ [193].

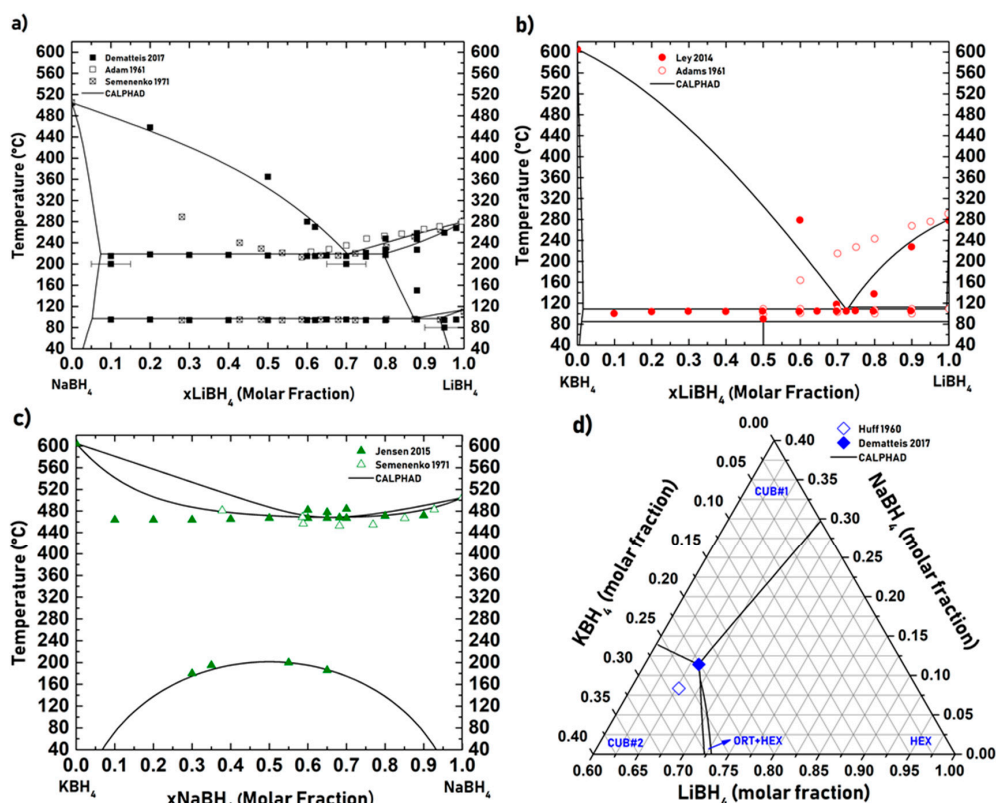


Figure 15. Literature experimental data from different authors assessed phase diagrams for the NaBH₄-KBH₄ (a), LiBH₄-NaBH₄ (b), LiBH₄-KBH₄ (c) systems and calculated minima of the liquidus surface for the LiBH₄-NaBH₄-KBH₄ (d) system. (CUB#1 and CUB#2 = cubic phases, ORT = orthorhombic phase, HEX = hexagonal phase).

LiBH₄-KBH₄

The LiBH₄-KBH₄ system (noted as LiK) was reported to be eutectic by Ley et al. [245] and Huff [271] with a melting temperature of 105 °C for the composition 0.72LiBH₄-0.28KBH₄. It has a theoretical H₂ capacity of 13.2 wt % [235]. A similar phase diagram with the same trends, but with a different eutectic composition, was reported by Adams [268]. No solid solution has been observed in known LiK systems; however, a bimetallic compound LiK(BH₄)₂ has recently been reported, which decomposes at 96 °C into LiBH₄ and KBH₄ [245]. Figure 15b reports all experimental literature data and the calculated phase diagram of the system assessed by the CALPHAD method by Dematteis et al. [249].

NaBH₄-KBH₄

To date, two experimental studies have been reported for the NaBH₄-KBH₄ [248,269] system (noted as NaK). Jensen et al. [248] showed the formation of a solid solution with full solubility above 200 °C and a minimum melting temperature of 458 °C for the composition 0.68NaBH₄-0.32KBH₄.

Below 200 °C, a miscibility gap has been evidenced by Jensen, but it was not reported from the previous study by Semenenko et al. [269]. The solid solution can be quenched at RT and the de-mixing kinetic of the solid solution at RT was studied by NMR [248]. The binary system was fully assessed by Dematteis et al. [249] and its phase diagram is presented in Figure 15c.

LiBH₄-NaBH₄-KBH₄

The thermodynamics of LiBH₄-NaBH₄-KBH₄ ternary system has been fully described combining experimental and theoretical investigations by Dematteis et al. [249]. Using the CALPHAD method combined with ab initio calculations, they determined the end-members and optimized LiBH₄-NaBH₄, LiBH₄-KBH₄ and NaBH₄-KBH₄ pseudo-binary phase diagrams data (Figure 15). The new exact ternary eutectic composition was determined and confirmed to be 0.66LiBH₄-0.11NaBH₄-0.23KBH₄ with a melting temperature of 102 °C, contrarily to that reported by Huff [271]. Figure 15d presents the liquidus projection of the eutectic melting in the LiBH₄-NaBH₄-KBH₄ ternary phase diagram.

Other Systems

The formation of eutectics has been demonstrated in binary and ternary systems, and the hydrogen release often occurs, involving a liquid phase, typically above 200 °C and at characteristic peak temperatures (T_{peak}) that depend on the interaction among the cations and the complex anion of [BH₄]⁻ in the liquid phase. The only binary system that does not show a low temperature liquid is the Mg(BH₄)₂-Ca(BH₄)₂ system, recently characterized by Dematteis et al. [272]. The dehydrogenation process is usually very complex with multi-step reactions and is subject to the conditions used, such as temperature, heating-rate, and atmosphere.

An explorative investigation of equimolar ternary combinations in the [LiBH₄-NaBH₄-KBH₄-Mg(BH₄)₂-Ca(BH₄)₂] system by Dematteis et al. [273] proved the presence of possible new ternary eutectics, such as in the LiMgCa, LiNaCa and LiNaMg systems, while NaMgCa, NaKMg and KMgCa systems presented the formation of solid solutions. Few bimetallic compounds are also formed in these ternary systems, such as KCa(BH₄)₃, LiKMg(BH₄)₄ and LiK(BH₄)₂, which affect the overall decomposition processes of this system [273].

For the first time, the existence of a quinary liquid borohydride phase was described by Dematteis et al. [274]. Above 250 °C, a five-component liquid borohydride was synthesized by an equimolar mixture of LiBH₄-NaBH₄-KBH₄-Mg(BH₄)₂-Ca(BH₄)₂ obtained via eutectic reactions involving bimetallic borohydrides. The dehydrogenation reaction of the five-component liquid borohydride occurs in a complex multistep reaction as for the ternary and quaternary systems. Dehydrogenation temperatures are not significantly improved with respect to the pure borohydrides. Furthermore, not all the initial borohydrides have shown decomposition during treatment up to 500 °C.

3.3.2. Thermodynamic Properties of Eutectic Borohydride Systems

The enthalpies of mixing the liquid phase for the assessed systems based on borohydrides [247,249] shows negative or low positive values (Table 3), suggesting an attractive interaction among different borohydrides in the liquid phase. Experimental values of the enthalpy of mixing are difficult to measure and the lack of information for such important thermodynamic properties leaves a gap in the full description of thermodynamics of eutectic borohydride systems. However, by the CALPHAD approach, eutectic borohydride systems can be assessed considering different contribution to the excess Gibbs free energy. They can be theoretically described in the whole temperature, pressure and compositional range. In the case of an ideal solution model, the enthalpy of mixing for a solution is equal to zero. If an ideal behaviour for both solid and liquid phases is considered for a binary A-B system, the enthalpy of mixtures is the weighted average of that of the pure components. Therefore, the enthalpy of melting varies linearly, as a function of composition, between those of the pure components. Neglecting the temperature dependence of the enthalpy, the deviation from the ideal behaviour of the liquid phase can be outlined by a simple thermodynamic cycle if the solid solutions are taken as

ideal. In fact, the enthalpy of mixing for the liquid phase (ΔH_{mix}) can be estimated from the difference between the enthalpy of melting of the AB mixture (ΔH_{mAB}) and of the weighted average of that of the pure components (ΔH_{mA} and ΔH_{mB}):

$$\Delta H_{mix} = \Delta H_{mAB} - x_A \Delta H_{mA} - x_B \Delta H_{mB} \quad (12)$$

where x_A and x_B are the molar fractions of the A and B components, respectively.

Table 3. Assessed (ΔH_{mASS}) values (in kJ mol^{-1}) for the enthalpy of melting in pure and mixed borohydrides. Assessed (Ω_{ASS}) values (in kJ mol^{-1}) of the interaction parameters for the liquid phase, according to the regular solution model.

Composition	ΔH_{mEXP}	ΔH_{mASS}	Ω_{ASS}	Reference
LiBH ₄		7.200		[202]
NaBH ₄		16.900		[275]
KBH ₄		19.200		[249]
0.70LiBH ₄ 0.30NaBH ₄	6.990	6.520	-19.604 *	[249]
0.725LiBH ₄ 0.275KBH ₄	11.025	9.828	-13.016	[249]
0.682NaBH ₄ 0.318KBH ₄	17.028	15.331	1.056	[249]

* A temperature dependency and sub-regular model were used to describe the LiBH₄-NaBH₄ system. The reported values have been recalculated in this review for a system described by a regular model.

The regular solution model defines the enthalpy of mixing as a function of composition for a binary A-B system by Equation (13):

$$\Delta H_{mix} = x_A x_B \Omega \quad (13)$$

where Ω is the interaction parameter, which can be easily estimated according to Equation (14):

$$\Omega = \frac{\Delta H_{mAB} - x_A \Delta H_{mA} - x_B \Delta H_{mB}}{x_A x_B} \quad (14)$$

By the integration of the differential scanning calorimetry (DSC) signal of the melting reactions in mixtures of borohydrides, the enthalpy changes from solid to liquid phase can be measured. Thus, possible interactions in the liquid phase can be evidenced and the value for the enthalpy of mixing can be estimated. For binary systems showing thermal minima (e.g., NaBH₄-KBH₄), the solid solution can be considered as ideal. In case of a eutectic melting (e.g., LiBH₄-NaBH₄ and LiBH₄-KBH₄), the solid phases can be considered fully immiscible so that the enthalpy of the solid mixture is obtained by averaging that of the pure components. Then the CALPHAD method allows the assessment of these parameters using a least square fit and taking into account all available data on pure compound from the available database or new experimental data [235]. For the LiBH₄-NaBH₄, the assessed value of Ω (Table 3) is negative, confirming the presence of a strong interaction in the liquid phase. For the LiBH₄-KBH₄ system, the assessed value is strongly negative. Finally, for the NaBH₄-KBH₄ system, Ω_{ASS} presents a low positive value. A deviation from the ideal cubic solid solution can explain the assessed value. The assessed enthalpy of mixing for the liquid phase is reliable, because they take into account possible variation of enthalpy as a function of temperature and possible deviations for ideal solid solutions.

As presented, in borohydride mixtures, all binary multi-cationic systems investigated so far show a stabilisation of the liquid phase, forming eutectic mixtures with negative or low positive enthalpy of mixing of the liquid phase [249]. Meanwhile, binary multi-anionic system of borohydrides and halides

evidenced a strong interaction in the solid phases, while no eutectic point has been reported yet. It can be concluded that in borohydride systems, the cationic and anionic sub-lattices play a different role in the interaction in solid and liquid phase upon mixing. Their thermodynamics are strongly related to the structures, coordination number, temperature, enthalpy and entropy of the transitions.

The stability of a phase is related to the reciprocal interaction among the ionic sublattices and electronegativity of the ions involved in the structure [276]. In the case of anionic substitutions, the formation of a solid solution is favoured, which may indicate that the anionic sublattices of the borohydrides are characterized of equivalent sites, which can host randomly different anions with a similar size. Nevertheless, the cation sublattices are more related to their characteristic coordination number, limiting the formation of solid solutions, but allowing destabilizing the sublattices towards a liquid phase. The stabilisation of the liquid phase at low temperatures can partially be understood considering a variation of the charge distribution in the physical mixture of different borohydrides. Short-range order and entropy could play a role as well in the formation of a multi-cation liquid phase, which should be further investigated.

3.3.3. Hydrogen Storage Properties of Eutectic Metal Borohydride Systems

The dehydrogenation mechanism of the 0.62LiBH₄-0.38NaBH₄ mixture in flowing Ar has been systematically investigated by Liu et al. [237]. A weight loss of 10.8 wt % hydrogen was recorded after heating to 650 °C through two major decomposition routes with the precipitation of LiH, Li₂B₁₂H₁₂ and B (287 °C to 520 °C), and Na and B (520 °C to 650 °C). The re-hydrogenation attempts showed that the hydrogen content decreased from 5.5 wt % to 1.1 wt % and to 0.8 wt % with no evidence of a reformation of LiBH₄. It was suggested by Liu et al. [277] that this poor cyclic stability could be improved by nanoconfinement.

The eutectic 0.725LiBH₄-0.275KBH₄ melts at 105 °C. Subject to the temperature profile, it releases up to 8.9 wt % hydrogen in Ar [278]. Like the LiBH₄-NaBH₄ mixture, it does not release hydrogen during melting. The dehydrogenation steps are firstly involving the formation of LiH, Li₂B₁₂H₁₂, B and H₂ from 290 °C to 700 °C, and secondly K, KH, B and H₂ from 550 °C to 700 °C. This mixture has a poor cyclic stability as the reversible hydrogen content decreased dramatically from 5.8 wt % to 1.0 wt % from the second cycle [278], which cannot be improved through nanoconfinement [238].

Dematteis et al. [191] investigated the hydrogen storage properties of eutectic borohydrides mixed with Mg₂NiH₄ to form reactive hydride composites (RHC). This approach evidenced enhanced kinetic and thermodynamics, and reversible hydrogen release under moderate pressure and temperature conditions [180]. In fact, the hydrogen release properties of mixtures, such as Mg₂FeH₆-M(BH₄)_x (M = Li, Na, K, Mg, Ca) have recently been explored [279]. Mg₂NiH₄-M(BH₄)_x systems (M = Li, Na, Ca; x = 1,2) have been investigated as well. These show an improvement of the hydrogen decomposition properties and a better cyclability [280–285]. The decomposition reaction might form boride species such as MgNi_{2.5}B₂. The latter species are boron donors to reversibly form the borohydride during the re-hydrogenation process. Dematteis et al. [191] also observed a lower decomposition temperature of the RHC mixture if LiBH₄ is in a eutectic mixture with borohydrides that contain stable single charged metal cation, while a leftover of the more stable borohydrides was detected after cycling. In the eutectic mixture, the presence of double charged metal cation (i.e., Ca(BH₄)₂ and Mg(BH₄)₂) leads to a complete decomposition of the borohydrides. If compared the hydrogen release temperatures of the pure borohydride and pure Mg₂NiH₄, its decrease is promoted by the presence of a stable liquid at low temperature.

3.3.4. Conclusions

The present chapter focused on the thermodynamic and hydrogen storage properties of several known low melting point borohydride systems, such as LiBH₄-NaBH₄, while halide substitution has been described elsewhere [190,286]. Given by the nature of liquid phase, these systems can start to deliver hydrogen at much lower temperatures when compared with their pure constituents. The

reorganization of crystal structure after fusion may, in principle, lead to a weakening (or strengthening) of chemical bonds as a consequence of changing chemical environment, which can affect the decomposition. Usually, the dehydrogenation of these systems goes through a complex path with the formation of a series of B-contained phases. One of the important issues is to identify the eutectic temperature for such multi-components systems. With the help of simulation methods, i.e., ab initio and thermodynamic assessment methods, the eutectic temperature could be refined for the known systems or predicted for new systems. Prior to this study, only few hydrides and LiBH_4 were fully described with the CALPHAD method. A limited database was available for metal hydrides and complex hydrides. Within the ECOSTORE project, pure borohydrides, binary and ternary combination of eutectic borohydrides of interest were fully characterised and assessed. However, a detailed description of the structure and thermodynamics of the liquid phase in borohydrides is still missing and should be investigated, possibly with total scattering methods. Experimental values of thermodynamic properties of eutectics and liquid borohydrides would be of interest to enhance the understanding of the role of the liquid in the thermal decomposition or hydrogen release reactions. They can be determined by accurate calorimetric measurements coupled with volumetric measurements.

The critical assessment and the incorporation of data into databases for calculations improve the understanding of various industrial and technological processes as well as helping in the prediction of properties of multicomponent systems. The CALPHAD method is a powerful tool for a complete description of the thermodynamic properties of borohydride mixtures. An estimation of the decomposition reactions in the investigated system can be obtained with the current optimised database. However, it should be coupled with experimental evaluation of decomposition products. As a matter of fact, the studies presented in this chapter critically collect previous studies and combine them with new experiments to finally describe the thermodynamic properties in all temperature, pressure and composition ranges.

3.4. Kinetic Tailoring of $2\text{LiBH}_4 + \text{MgH}_2/2\text{LiH} + \text{MgB}_2$ with Cost Effective $3\text{TiCl}_3 \cdot \text{AlCl}_3$

Hydrogen storage in complex metal hydrides (e.g., borohydrides $[\text{BH}_4]^-$, alanates $[\text{AlH}_4]^-$, and/or amides $[\text{NH}_2]^-$) is a fascinating field, ever since Bogdanović and Schwickardi published their seminal article reporting the possibility of the re-hydrogenation of sodium alanate in the presence of a Ti-based catalyst [287]. Since this discovery in 1996, the field of complex metal hydrides has expanded tremendously and a great number of complex metal hydrides for hydrogen storage system have been explored. However, due to the strong covalent bonds of B-H, N-H, Al-H and Ni-H in $[\text{BH}_4]^-$, $[\text{NH}_2]^-$, $[\text{AlH}_4]^-/[\text{AlH}_6]^-$ and $[\text{NiH}_6]^{4-}$, respectively [288–290], reaction kinetics involving the breaking and the formation are usually sluggish. As discussed previously, for a decade, several strategies have been developed to accelerate the hydrogen sorption properties of complex hydride materials. Firstly, the combination of two or more single hydrides to form new compounds may lower the stability or reaction enthalpy of the system and promote its reversibility while minimizing the loss of the hydrogen capacity of the original materials [151,285,291–294]. While amide examples were discussed previously, other reactive hydride composites, such as $\text{MgH}_2 + 2\text{NaBH}_4$, $\text{Mg}_2\text{NiH}_4 + \text{Ca}(\text{BH}_4)_2$, and $\text{MgH}_2 + 2\text{LiBH}_4$, are a tactic to destabilize metal hydride compounds by formation of corresponding metal hydride and MgB_2 upon thermal decomposition. The latter reaction product was shown to be a desired product as it aids in re-hydrogenation by providing a pathway for the borohydride formation [295]. Secondly, the doping with suitable additives, i.e., transition metal-based additives, which provide kinetically favored nucleation sites for the formation of reaction products for the proceeding of the hydrogen uptake and release at moderate temperature and pressure conditions. Several additives such as Ti, Zr/V/Ce containing additives, Sc_2O_3 , Nb_2O_5 or halides (NbF_5 , TiCl_3) greatly improved the dehydrogenation-hydrogenation rates of lithium-based reactive hydride composites [296–306]. Thirdly, the confinement of the storage materials in adaptive scaffolds for improved hydrogen sorption properties [307] leads to the increase of the materials surface area, reduces the hydrogen diffusion distance and provides adjacent contact between reactants [308–313].

In this chapter, the second approach will be addressed in more detail for the kinetic improvement of Li-RHC system. The Li-RHC system (i.e., $2\text{LiBH}_4 + \text{MgH}_2/2\text{LiH} + \text{MgB}_2$, denoted as Li-RHC) has attracted much attention for hydrogen storage due to its appealing theoretical hydrogen storage capacity of 11.5 wt % and calculated reaction enthalpy of $45.9 \text{ kJ mol}^{-1} \text{ H}_2$ [291,294]. This system shows the possibility to obtain fully reversible metal borohydrides at evaluated temperature and hydrogen pressure conditions. Vajo et al. [294] reported the possibility to hydrogenate 2LiH and MgB_2 including a catalyst (2–3 mol % TiCl_3) following the reaction scheme: $2\text{LiBH}_4 + \text{MgH}_2 \leftrightarrow 2\text{LiH} + \text{MgB}_2 + 4\text{H}_2$. Further efforts have been made to investigate the RHC $\text{NaH} + \text{MgB}_2$, with a theoretical hydrogen capacity of 7.8 wt % for a 2:1 molar equivalent of NaH and MgB_2 . The suggested reaction products upon hydrogenation are 2NaBH_4 and MgH_2 . However, it was shown that this procedure had intermediate reaction products such as NaMgH_3 , which decreased the hydrogen capacity. The reaction is plagued with slow hydrogen sorption kinetics and with a low experimentally obtained hydrogen absorption capacity of only 3.8 wt % [314–319]. Recently, Le et al. [320] reported a study of the effect of $3\text{TiCl}_3 \cdot \text{AlCl}_3$ on the kinetic sorption properties of Li-RHC system. In their work, they showed remarkably improved dehydrogenation kinetics of Li-RHC in the presence of the $3\text{TiCl}_3 \cdot \text{AlCl}_3$ additive (Figure 16), i.e., the incubation for the formation of MgB_2 is considerably reduced by 10 h. The increase of the molar amount of $3\text{TiCl}_3 \cdot \text{AlCl}_3$, from 7.5 to 30, leads to minimizing the incubation period between the two reaction steps. However, because of the increased amount of $3\text{TiCl}_3 \cdot \text{AlCl}_3$, the amount of released hydrogen considerably declines from about 10 wt % to 8 wt %.

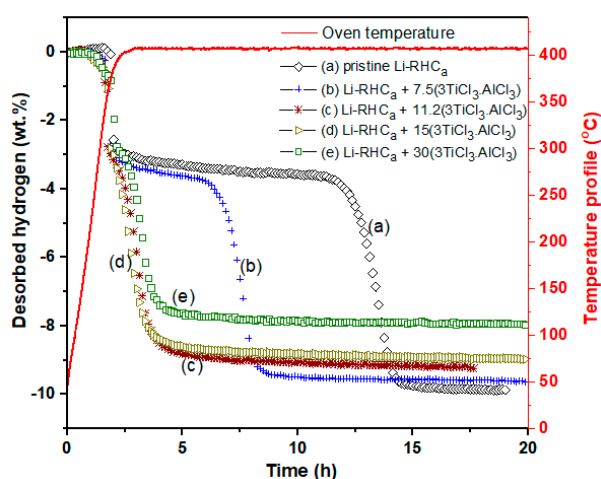


Figure 16. First dehydrogenation of the Li-RHC composites: (a) pristine Li-RHC_a , (b) $\text{Li-RHC}_a + 7.5(3\text{TiCl}_3 \cdot \text{AlCl}_3)$, (c) $\text{Li-RHC}_a + 11.2(3\text{TiCl}_3 \cdot \text{AlCl}_3)$, (d) $\text{Li-RHC}_a + 15(3\text{TiCl}_3 \cdot \text{AlCl}_3)$, (e) $\text{Li-RHC}_a + 30(3\text{TiCl}_3 \cdot \text{AlCl}_3)$. Adapted with permission from Le, T.-T., C. Pistidda, J. Puszkiel, M.V. Castro Riglos, F. Karimi, J. Skibsted, S.P. GharibDoust, B. Richter, T. Emmler, C. Milanese, A. Santoru, A. Hoell, M. Krumrey, E. Gericke, E. Akiba, T.R. Jensen, T. Klassen, and M. Dornheim, Design of a Nanometric AlTi Additive for MgB_2 -Based Reactive Hydride Composites with Superior Kinetic Properties. The Journal of Physical Chemistry C, 2018. 122(14): pp. 7642–7655. Copyright (2018) American Chemical Society.

It was shown above that the use of the selected additive clearly promotes the sorption kinetics of the system (Li-RHC). Figure 17 shows the measured reversible hydrogen capacity of the studied materials in both the hydrogenated and dehydrogenated states for 20 hydrogenation-dehydrogenation cycles. The additive $3\text{TiCl}_3 \cdot \text{AlCl}_3$ presents a beneficial effect on the hydrogen storage of the material prepared in dehydrogenated state (Figure 17b—Li RHC_d) rather than on the material prepared in the hydrogenated state (Figure 17a—Li RHC_a). Clearly, the $\text{Li-RHC}_d + 7.5(3\text{TiCl}_3 \cdot \text{AlCl}_3)$ material shows the highest measured hydrogen storage capacity, i.e., ~9.5 wt % and a rather stable cycling behaviour, with a loss of capacity smaller than 1.2 wt % over 20 cycles. The reduction of the hydrogen storage capacity for most of doped Li-RHC composites is less than 1.2 wt.%, except for the system

Li-RHC_d + 3.7(3TiCl₃·AlCl₃), containing a small amount of additive, which shows the largest drop of capacity (>2 wt %) in the cycling period. This could be attributed to the unsatisfying dispersion of the additive over the host material Li-RHC. Moreover, Li-RHC_d + 7.5(3TiCl₃·AlCl₃) displays the shortest kinetic performance (hydrogenation-dehydrogenation times of ~30 min) in both hydrogenation and dehydrogenation processes in comparison to the material prepared in the hydrogenated state Li-RHC_a + 7.5(3TiCl₃·AlCl₃), reported in [320].

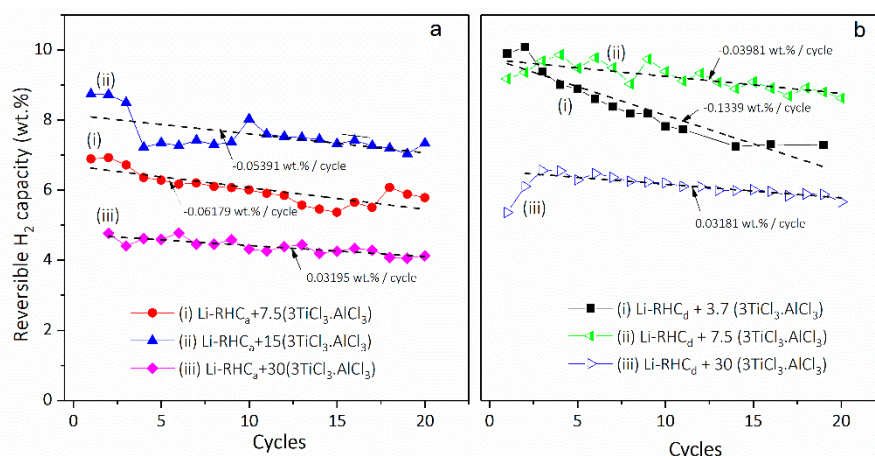
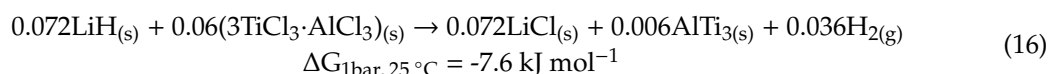
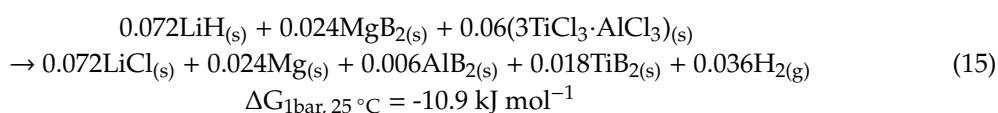


Figure 17. Reversible hydrogen storage capacities over 20 hydrogenation-dehydrogenation cycles based on the dehydrogenation curves. Cycling process performed at 350 °C and 400 °C under 50 bar and 3 bar hydrogen backpressure for the hydrogenation and dehydrogenation, respectively. Backpressure is necessary to avoid the formation of B₂H₆. (a) Samples prepared in the hydrogenated state (Li-RHC_a). (b) Samples prepared in the dehydrogenated state (Li-RHC_d). Adapted with permission from Le, T.-T., Pistidda, C.; Puszkiel, J.; Riglos, M.V.C.; Karimi, F.; Skibsted, J.; GharibDoust, S.P.; Richter, B.; Emmler, T.; Milanese, C.; Santoru, A.; Hoell, A.; Krumrey, M.; Gericke, E.; Akiba, E.; Jensen, T.R.; Klassen, T.; Dornheim, M. Design of a Nanometric AlTi Additive for MgB₂-Based Reactive Hydride Composites with Superior Kinetic Properties. The Journal of Physical Chemistry C, 2018. 122(14): p. 7642–7655. Copyright (2018) American Chemical Society.

In additional reports [296–305], the formation of TM borides was strongly suggested from the interaction between the Li-RHC with TM-based compounds. For the Li-RHC doped with 3TiCl₃·AlCl₃, the calculations of phase composition are referred to in the study of Le et al. [320]. The calculation showed that the formation of TiB₂ and AlB₂ (Equation (15)) over milling is thermodynamically more favorable than the formation of AlTi₃ (Equation (16)). However, the characterization by XPD and ¹¹B NMR [320] showed that no observation of transition metal borides is detected and the presence of free Mg as proposed in Equation (15) is not observed. Thus, the formation of TiB₂ and AlB₂ may be kinetically constrained and the formation of AlTi₃ is likely to take place.



Conclusively, the presence of Ti/Al containing particles in the Li-RHC_a + 7.5(3TiCl₃·AlCl₃) was examined by the high-resolution transmission electron microscopy (HR-TEM) technique by Le et al. [320]. Figure 18 shows the nanosized particles of hexagonal AlTi₃ and cubic AlTi₂ which are observed in the material after ball milling. During cycling, the XPD data depicted in Figure 18b,c show hexagonal AlTi₃ and cubic AlTi₂ which are still detectable as well as cubic AlTi₃. As observed,

the most frequently identified nanoparticles belong to the hexagonal AlTi_3 phase. In addition, the transition metal borides (TiB_2 and AlB_2), Mg-Al alloys and Mg-Al-B compounds have not been found via HR-TEM. The sizes of the hexagonal AlTi_3 after milling and cycling are estimated in the range of 1 to 10 nm and 1 to 5 nm, respectively. These observations are in accordance with the anomalous small angle X-ray scattering (ASAXS) results [320].

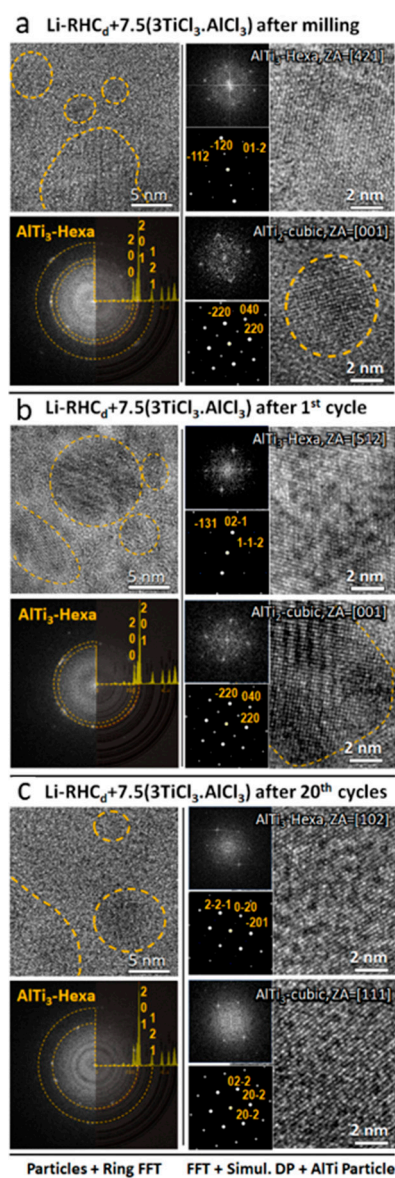


Figure 18. HR-TEM data and determination of the nanosized AlTi alloys in Li-RHC_d + 7.5(3TiCl₃·AlCl₃) (a) after milling, (b) after the 1st cycle and (c) after the 20th cycle. A fast Fourier transformation (FFT) analysis was employed for calculation in each region and compared to simulated diffraction patterns in the adequate orientation; the width of the FFT and corresponding simulations is 18 nm^{-1} . Structure cards: hexagonal AlTi_3 ICSD 191189, cubic AlTi_3 ICSD 189695, cubic AlTi_2 ICSD 189696. Adapted with permission from Le, T.-T., Pistidda, C.; Puzskiel, J.; Riglos, M.V.C.; Karimi, F.; Skibsted, J.; GharibDoust, S.P.; Richter, B.; Emmmler, T.; Milanese, C.; Santoru, A.; Hoell, A.; Krumrey, M.; Gericke, E.; Akiba, E.; Jensen, T.R.; Klassen, T.; Dornheim, M. Design of a Nanometric AlTi Additive for MgB₂-Based Reactive Hydride Composites with Superior Kinetic Properties. The Journal of Physical Chemistry C, 2018. 122(14): p. 7642–7655. Copyright (2018) American Chemical Society.

It is well known that for metal alloy systems, the nucleation and growth of precipitates is strongly influenced by crystallographic and morphological features [321]. The presence of a phase with particular crystallographic structure plays a critical role in the nucleation, growth and distribution of certain precipitates. The similarities of crystal features between the new phase and the parent phase lead to a lower energy at the coherent interface by decreasing the interface lattice misfit. Zhang et al. [322] pointed out the criteria for the edge-to-edge matching model and stated that the strain energy between the substrate and nucleus is significantly minimized when the misfit of the interatomic spacing of their close-packed or nearly close-packed atom rows is $<10\%$ and their interplanar mismatch is $<6\%$. As for the precipitates of the metal alloys, in the RHC system, the crystallographic features of the in situ formed nanoparticles and their location seem to play an important role to the processes of nucleation and growth of new phases. Bösenberg et al., Bonatto Minella et al., Puszkiel et al., and Le et al. [296,320,323,324] used these above-mentioned criteria to explain the influence of the additives on the kinetic properties of the RHC systems. They independently reported that the parent phases having similar crystal structure as the newly developing phase can act as heterogeneous nucleation sites for nucleus formation. Several transition metal borides such as TiB_2 , NbB_2 and VB_2 can provide coherent interfaces to improve the heterogeneous nucleation and growth of hexagonal MgB_2 [296,298–301,303–305,325]. As an example, the illustration of the growth of MgB_2 during dehydrogenation, adapted from [296], is given in Figure 19. For this case, Li-RHC mixed with $3\text{TiCl}_3\cdot\text{AlCl}_3$ results in the in situ formation of AlTi nanoparticles. The necessary requirements for an effective heterogeneous nucleation are reported in Refs. [296,322,323]. In detail, those are firstly a low interfacial energy amongst the nucleation agent and the newly developing phase. Secondly, a sufficient high amount of the nucleation agent. Thirdly, the appropriate distribution of the nucleation agent. To obtain the minimized lattice mismatch, the atom rows in the close-packed or nearly closed-packed planes arranged to meet edge to edge at the interface. A simple approach to identify the close-packed planes is by XPD. The close-packed planes are those with the highest X-ray diffraction intensity in the diffraction patterns. The relative difference in the d -value between two close-packed planes is known as d -value mismatch. There is a critical value of the d -value mismatch, below which the planes containing the atom rows in the two phases can match well, so that the interfacial energy is minimized. A reasonable reference value for the critical d -value mismatch is 6% or smaller [322].

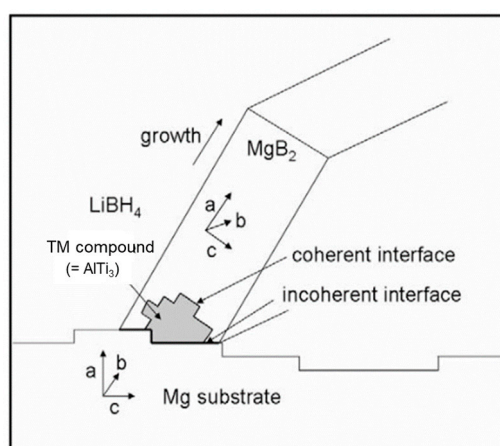


Figure 19. Model of plate-like growth of MgB_2 during dehydrogenation. TM compound is assumed to be located in the interface to the Mg substrate. The figure was adapted from Reference [296]. Reprinted from Bösenberg, U.; Kim, J.W.; Gossler, D.; Eigen, N.; Jensen, T.R.; von Colbe, J.M.B.; Zhou, Y.; Dahms, M.; Kim, D.H.; Günther, R. Role of additives in $\text{LiBH}_4\text{-MgH}_2$ reactive hydride composites for sorption kinetics. *Acta Materialia*, 2010. 58(9): p. 3381–3389. Copyright (2010), with permission from Elsevier.

Opposed to the reports of Bösenberg et al., Bonatto Minella et al., and Puszkiel et al., [296,323,324], in Le et al., AlTi alloys have been identified as a product of the interaction between Li-RHC and

$3\text{TiCl}_3 \cdot \text{AlCl}_3$. The d -value mismatches of AlTi alloys and MgB_2 have been calculated, referred to [320], that is, MgB_2 {1011} // hexagonal-AlTi₃ {2021} = 3.3%; MgB_2 {1010} // cubic-TiAl₃ {2020} = 31.9% and MgB_2 {1010} // cubic-TiAl₂ {2020} = 35.0%. These results point out that the hexagonal AlTi₃ phase has a similar crystal structure to MgB_2 with a d -value mismatch less than 6%. Additionally, based on the observed kinetic improvement in $\text{Li-RHC}_d + 7.5(3\text{TiCl}_3 \cdot \text{AlCl}_3)$ and according to the ASAXS [320] and HR-TEM results, the proper amount of AlTi₃ nanoparticles appears to be well dispersed and is located on the formed MgB_2 upon cycling. From these observations, it is indicated that the hexagonal AlTi₃ alloy plays an efficient heterogeneous nucleation for formation of newly developing phase (MgB_2). Furthermore, the presence of AlTi₃ facilitates the decrease of MgB_2 particle size, leading to a faster consumption of MgB_2 , suppressing the MgB_2 agglomeration and providing a more active surface for the interaction between material and hydrogen gas.

In conclusion, the investigations on tailoring the sorption kinetics with additives of the reactive hydride composites, involve the understanding of the kinetic and thermodynamic behaviours of the studied system. The findings reported in this chapter lay the ground for continuing research and for transferring the developed approaches to similar RHC systems. A deeper investigation of possible synthetic pathways for producing TM-based nanoparticles is expected to lead to a better tailoring and to further improvement of the material kinetic properties.

3.5. Role of Nanoconfinement in Enhancing the Properties of Hydrogen Storage Materials

Despite the high hydrogen content of many light metal hydrides and complex hydrides, the high stability of these compounds precludes their application for hydrogen storage purposes, commonly due to the high temperatures and low reversibility of the dehydrogenation reactions. As already mentioned before one of the strategies to address this issue involves the nanoconfinement of hydrides in porous matrices with pore size in the order of few nanometres, destabilizing the confined material and promoting the hydrogen exchange [326]. With this approach, it is possible to reduce drastically the macroscopic size of the material by introducing and trapping it in small cavities. The confined hydride is physically prevented from agglomerating by the pore walls, allowing the formation of nanostructured material in form of size-controlled nanoparticles. The term nanostructured material referred to a material with a microstructure characterized by length scale in the order of a few nanometres, typically between 1 and 10 nm, that maybe extended into one, two or three dimensions, as in nanorods, layers or coating and nanoparticles, respectively.

The decrease of the particle size leads to an increase of the surface to volume ratio. However, creating surfaces costs energy, if the surface energy of the hydride is larger than that of the metal, this operation will reduce the enthalpy of the formation of the system. For small particles, the energetic contribution given by the surface energy cannot be ignored and the reduced ΔH implicates a substantial destabilisation of the whole system [327–329]. In addition to the aforementioned destabilisation, the size reduction of the particles directly affects the kinetics of hydrogenation/dehydrogenation, increasing the rate of hydrogen dissociation on the surface and the diffusion of hydrogen into the structure of the material [313,330].

High-energy ball milling [254] is still the most common method to obtain such small particles, with grain sizes down to 3–25 nm with a relatively controllable particle size distribution and reduced equipment costs [331–333]. This first step in a “top-down patterning to guide bottom-up assembly” [334] is followed by more complicated approaches involve bottom-up mechanisms of nucleation and particles growth in solution or vapor that requires good control of the reaction conditions. Such methods are, however, not easy to scale up and are mostly used in the case of TM [335–338]. However, the good achievements reached with ball milling and other synthesis of hydrides nanoparticles are soon nullified by hydrogenation-dehydrogenation cycles that contribute to the aggregation and re-aggregation of the particles via repeated sintering [293,339,340].

The confinement of hydrides requires porous materials with certain characteristics in order to be viable for application. In first instance, the scaffold needs a proper porous structure. A high pore

volume is a fundamental aspect to allow the confinement of sufficient amounts of active material. Common values of total pore volume are near to 1 mL g^{-1} where higher values are even more appreciated [341–343]. However, not all pores are good for the confinement of hydrides and the synthesis of nanoparticles. The size and connectivity of the pores are crucial aspects to take into consideration. If the cavities are excessively large, the host particles would have a behaviour comparable to that of the bulk. Moreover, capillary forces that drive the introduction into the pores of material in a liquid phase are substantial between a diameter of 2 and 50 nm [344]. Specifically, the International Union of Pure and Applied Chemistry (IUPAC) nomenclature refers to materials with a pore size between 2 nm and 50 nm as “mesoporous materials” [345].

The structural material must be light in order to maintain an overall acceptable gravimetric density of hydrogen. For this reason, carbon and silica are commonly favoured over other materials in the preparation of porous materials such as metal oxides. The latter are often chosen for catalytic applications, for the preparation of heat exchangers and biomedical applications [346–349]. Moreover, a good scaffold should be chemically inert with hydrides and have a high thermal stability as the common operation temperatures of metal hydrides are excessively high for scaffolds based on organic and polymeric structures. For this reason, both carbon and silica scaffolds are usually preferred, even if silica, due to many functional groups on the surface may react with the host material. For example, in the case of complex metal hydrides, LiBH_4 reacts with silica, forming irreversibly lithium silicates [41,350,351]. Carbonaceous scaffolds, however, can be heated at high temperatures without structural collapses and with an inert behaviour.

Both silica and carbon porous materials also satisfy the characteristics necessary for production on a large scale: the low price of production, involving cheap precursor materials and simple production methods.

In this section, nanoconfinement approaches will be discussed and related to complex metal hydrides.

3.5.1. Nanoconfinement Approaches

The confinement of the active material in pores of few nanometer can be performed following different approaches, limited by the physical chemical characteristics of the material. Wet infiltration and melt infiltration are the two main methods to introduce hydrides in a porous scaffold. The first method involves the solubility of the hydride in a solvent that, in the form of solute, can deeply penetrate into the porous structure of the host material. The solvent can then be removed by evaporation, leaving the active material trapped and widely dispersed in the porous structure, as reported by Peru et al. and others [352–355]. However, this method suffers from synthetic restrictions due to the solubility of the hydrides to nanoconfine, limiting the amount of material that is possible to solubilize and infiltrate, requiring more impregnations in order to load the scaffold properly [353]. Moreover, the strong interactions among solvent and solute hydrides can make the complete extraction of solvent required for the infiltration difficult, in particular, in the cases when the solvent generates stable coordination complexes with the solute [356,357]. The second method, melt infiltration, is adopted on hydrides or mixtures of hydrides with a decomposition temperature higher than their melting point. Ionic hydrides such as LiH , NaH or MgH_2 generally have high melting points. Much lower temperatures are required in order to melt complex metal hydrides such as alanates, borohydrides and amides. The melt infiltration of these compounds is simple and possible at relatively low temperatures with the application of a hydrogen backpressure in order to prevent the material decomposition with consequent hydrogen release [344,351]. Without the use of a solvent, the infiltration is faster and easier to perform. Moreover, the melt infiltration allows a more efficient load of the porous material since there are no limits due to the solvent solubility.

As mentioned previously, due to their high hydrogen content, borohydrides are among the most interesting compounds for hydrogen storage. However, these complex hydrides are characterized by elevated stability that prevents them from practical use. For this reason, the nanoconfinement

approach may be one of the best solutions to destabilize and make borohydrides and other systems previously discussed viable materials for hydrogen storage applications.

3.5.2. Confined Borohydrides

As mentioned on several occasions in this review, lithium borohydride seems promising for solid-state hydrogen storage. However, in bulk form, its stability allows only a slow hydrogen desorption. The presence of LiH among the reaction products reduces the overall hydrogen amount that one could obtain by thermal decomposition. Moreover, the high stability of the products makes it impossible to rehydrogenate LiBH₄ under reasonable pressure and temperature conditions [89,357]. A certain degree of destabilisation that improves the LiBH₄ sorption properties can be achieved by nanoconfinement [358]. LiBH₄ introduction in a porous scaffold has been performed both through chemical impregnation using tetrahydrofuran (THF) as solvent [359,360], and melt infiltration at about 280–300 °C under hydrogen or inert gas pressure [361–363]. The infiltrated LiBH₄ shows a clear increase of the hydrogen exchange rate of several orders of magnitude [361] and the desorption temperature decrease drastically. The onset temperature of composite materials with carbon is shifted to about 200 °C, while the main desorption peak is generally centered between 300 and 350 °C [359,362,364–366]. Moreover, the confined LiBH₄ shows enhanced reversibility under mild conditions, partially preserving its hydrogen capacity after few cycles. The reason for this improvement is the suppression of B₂H₆ release that, in turn, results from smaller pores preventing the loss of boron through B₂H₆ during dehydrogenation [366,367].

The investigation of the nanoconfinement effect is not limited to the pure LiBH₄. The presence of a low melting temperature eutectic mixture of borohydrides allowed the introduction in porous scaffold of LiBH₄ at even lower temperatures than 280 °C and further destabilisation due to the interaction of different cations in the molten phase [235,289]. In most of the eutectic mixtures examined, LiBH₄ constitutes the major fraction of the mixture, giving an overall high hydrogen density. NaBH₄ is very attractive for hydrogen storage but like LiBH₄, it releases hydrogen only at very high temperatures with the main desorption starting above 450 °C and proceeding with a multistep decomposition above 500 °C [368–370]. Evidence of its destabilisation and drastic reduction of desorption temperatures have been reported for nanoconfined composites. Pure NaBH₄ melts at about 500 °C [235], which allows for the melt infiltration under hydrogen atmosphere [369]. However, the stability in different solvents allowed the infiltration through various media such as liquid NH₃ [371], diglyme [352], *n*-propylamine [372] and even water at high pH values [352]. The desorption temperatures of nanoconfined NaBH₄ found in the aforementioned literature variate widely by the method, the materials adopted for the infiltration and by the scaffold. The composite materials obtained by melt infiltration in porous carbon show that the onset temperature shifted to below 300 °C while the main desorption takes place at 450 °C [369]. For the same materials, but impregnated with an alkaline aqueous solution, the values for the onset and main hydrogen desorption dropped further to 200 °C and 350 °C, respectively [369]. Similar temperatures for the main desorption were obtained by using NH₃ or diglyme as solvents showing initial low hydrogen release even below 150 °C [352,371]. Even better performances were achieved confining NaBH₄ among graphene layers by solvent impregnation with *n*-propylamine; in this case, the dehydrogenation starts below 40 °C with a main desorption at 200 °C showing a stable reversibility over a few sorption cycles [372].

The loading limitations due to the NaBH₄ solubility and the solvent elimination from the sample encouraged the improvement of the melt infiltration approach. The use of recently studied eutectic mixtures of LiBH₄ and NaBH₄ allows the introduction in a porous scaffold of a larger amount of hydrides [237,247]. A composite material obtained by nanoconfinement of a mixture of borohydrides achieves a kinetic enhancement by both the presence of the carbon scaffold and multiple cationic species. The introduction in a carbon aerogel allows the reduction of the hydrogen desorption temperatures of 107 °C, bringing the main desorption of the composite LiBH₄-NaBH₄ in carbon aerogel to 333 °C [246].

Among the alkali borohydrides, KBH_4 seems not to be very suitable for hydrogen storage applications, mostly due to the high stability and as consequence the high temperature of hydrogen release, $\sim 680^\circ\text{C}$ [235]. However, KBH_4 combined with LiBH_4 generates a low melting point system. The eutectic composition, with the 0.275 mol % of KBH_4 , melts at about 105°C , allowing the extremely low temperature melt infiltration of LiBH_4 and KBH_4 in porous scaffolds [245]. In carbon aerogel with an average pore diameter of 25 nm, the kinetics are improved and the system starts to release hydrogen at about 190°C , with a major desorption at about 400°C [238].

Another complex hydride with the potential to fulfill the requirements for hydrogen storage materials is $\text{Mg}(\text{BH}_4)_2$ due to its extremely high content of hydrogen of 14.9 wt.%. $\text{Mg}(\text{BH}_4)_2$ shows a variety of crystal structures, (α -, β -, γ -, δ -, ζ - and two as-yet unsolved structures β' - and ε - $\text{Mg}(\text{BH}_4)_2$) and its transitions are rich. For instance the porous γ - $\text{Mg}(\text{BH}_4)_2$ [373] experiences two endothermic phase changes, the first at $\sim 150^\circ\text{C}$ to the ε -phase, and the second at $\sim 180^\circ\text{C}$ to β' , as reported by Heere et al. and others [374,375], before the high temperature β -phase transition ($\sim 220^\circ\text{C}$) occurs. In contrast, α - $\text{Mg}(\text{BH}_4)_2$ transitions directly into the β phase at $\sim 220^\circ\text{C}$. The complexity of decomposition pathways, structures and dynamics are reported in [376,377].

In general, the hydrogen desorption for the $\text{Mg}(\text{BH}_4)_2$ bulk material occurs between 290°C and 500°C in different steps [378,379], while the nanoconfinement showed a general improvement of the hydrogen sorption behaviour. The infiltration of $\text{Mg}(\text{BH}_4)_2$ is performed via solvent impregnation, commonly using diethyl ether. In a carbon scaffold with pores smaller than 2 nm, $\text{Mg}(\text{BH}_4)_2$ shows hydrogen desorption starting at about 150°C under vacuum and peak temperatures at 257°C and 317°C [380]. Even better performances were recorded by infiltrating the $\text{Mg}(\text{BH}_4)_2$ in a porous scaffold doped with transition metals [381]. The use of a nickel-doped carbon drastically reduces the temperature of hydrogen release with the dehydrogenation starting at 75°C and reaching the maximum desorption rate at 155°C [382]. A melt infiltration approach is possible by using an eutectic mixture of LiBH_4 and $\text{Mg}(\text{BH}_4)_2$. The two borohydrides with a molar ratio of about 1:1 show a very low melting point of 180°C , allowing the introduction in porous scaffolds of a large amount of LiBH_4 and $\text{Mg}(\text{BH}_4)_2$ [383]. The presence of carbon accelerates the hydrogen desorption rate; meanwhile the encapsulation in small pores inhibits the formation of *closo*-borates, $[\text{B}_{12}\text{H}_{12}]^{2-}$, enhancing the cyclability [384]. The eutectic mixture infiltrated in carbon aerogel shows low desorption temperatures, with a first desorption peak in coincidence with the melting temperature of the mixture (180°C) and a major dehydrogenation at about 250°C against the bulk mixture, where the main dehydrogenation events occur in the temperature range of 230 – 400°C . Moreover, the 8.3 wt % of hydrogen uptake is maintained after four sorption cycles in comparison to the approximately 3 wt % of the bulk [239].

The last example in this chapter is calcium borohydride. This complex hydride decomposes in two main steps, the first at about 320°C and the second at 550°C , with an overall hydrogen capacity of 9 wt.% [385]. The introduction of pure $\text{Ca}(\text{BH}_4)_2$ in a carbon aerogel structure was performed by solvent impregnation with methyl tert-butyl ether (MTBE) [355]. Once nanoconfined, the hydride starts to release hydrogen at about 100°C , with a main desorption peak at about 280°C while showing a hydrogen capacity of 2.4 wt % for 18 cycles [355]. Further studies have been performed on eutectic mixtures of $\text{Ca}(\text{BH}_4)_2$ with LiBH_4 and their nanoconfinement. This eutectic mixture, with the composition determined to be 0.68LiBH_4 – $0.32\text{Ca}(\text{BH}_4)_2$, melts at about 200°C , allowing a low temperature melt infiltration in a porous material [236,252]. The infiltration in different carbon scaffolds showed the gradual decrease of the main dehydrogenation peak temperature with the reduction of the pore size, as shown in Figure 20 [386]. An even lower desorption temperature has been registered for high surface area CO_2 activated aerogel carbon, with a difference between bulk and infiltrated material of 95°C and the main desorption peak occurring at 298°C compared to 393°C for the bulk [246]. However, the improvements registered for the first desorption are gradually lost within five hydrogenation cycles [387].

3.5.3. Conclusions

Even bringing consistent improvements to various complex hydrides, the analyzed nanoconfined systems still do not have the characteristics required for practical applications. However, the study of new infiltrated materials opens new possibilities and lead us closer to the realization of a solid-state hydrogen storage application.

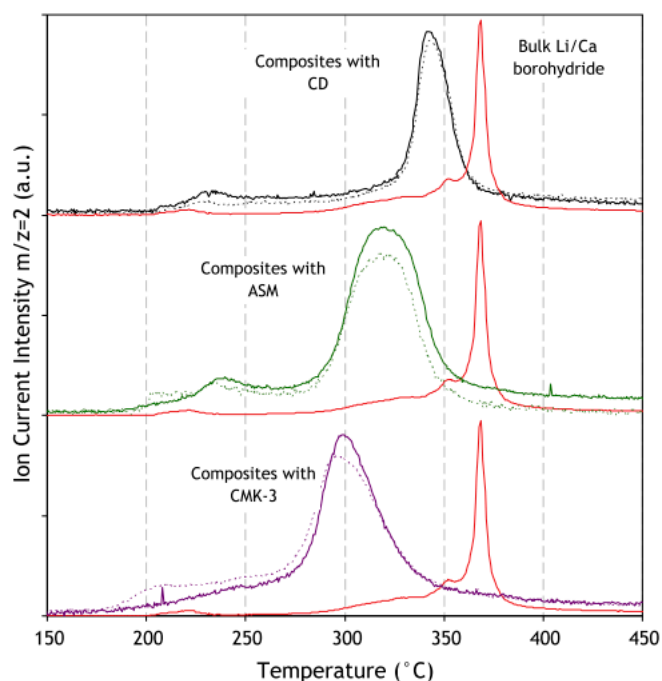


Figure 20. Thermal programmed desorption measurements coupled with mass spectrometry of an eutectic mixture of LiBH_4 and $\text{Ca}(\text{BH}_4)_2$ infiltrated in carbon scaffolds with different pore sizes. The dotted curves represent the physical mixture of carbon and hydrides while the solid curve shows the melt infiltrated composites. Red curve: bulk; black: composite with non-porous Carbon Disks (CD); green: with porous ASM (average pores diameter $\sim 25\text{nm}$), purple: porous CMK-3 (average pores diameter $\sim 5\text{nm}$). Note: CD are non-porous carbon disks. Figure is adapted from [386]. Reprinted from Ampoumogli, A., G. Charalambopoulou, P. Javadian, B. Richter, T.R. Jensen, and T. Steriotis, Hydrogen desorption and cycling properties of composites based on mesoporous carbons and a LiBH_4 – $\text{Ca}(\text{BH}_4)_2$ eutectic mixture. *Journal of Alloys and Compounds*, 2015. 645(1): p. S480-S484., Copyright (2015), with permission from Elsevier.

3.6. Rare Earth Borohydrides

The International Union of Pure and Applied Chemistry (IUPAC) defines rare earth (RE) elements (E) as the 15 elements belonging to the lanthanides group, plus yttrium and scandium, as they are usually found within the same ore. REE have atomic numbers (Z) of 57 to 71, 39 and 21, respectively. The lanthanide group, situated in the 4f block of the periodic table, has a decreasing ionic radius with an increasing atomic number. La (Z = 57) has the largest ionic radius (1.172 Å) and Lu (Z = 71) the smallest ionic radius (1.001 Å, based on the ionic radius of RE^{3+} cations in octahedral environment) [388].

When referring to REE, society usually infers this term to be related to their abundance, distribution and prices. In fact, the word ‘rare’ does not mean that they are not abundant; ‘rare’ simply refers to the difficulty scientists had in the 19th century in separating the REE from its ore. ‘Earth’ is an ancient term for oxide and finds its origin in the fact that REE permanently form oxides [389]. Their abundance in the earth crust is comparable to copper and lead. More specifically, the light REE (La-Sm) are more abundant than the heavy REE (Eu-Lu). Their abundance is between two and five orders of magnitude higher than precious Au or Pt [389].

3.6.1. Synthesis of Rare Earth Borohydrides (*REB*)

Rare earth borohydrides, pure and in composite mixtures, as well as in bimetallic compounds, are the focus of this chapter. A general overview of the metal borohydrides and their derivatives can be found in [190]. Nevertheless, the high thermal stability of the alkali and alkaline-earth borohydrides has attracted more attention to less stable compounds such as *RE* borohydrides and much attention has been paid to solvent-free as well as halide-free synthesis [390]. Generally, the approaches implemented for the synthesis of *REB* can be divided into solvent-free synthesis and solvent-based synthesis, as discussed below.

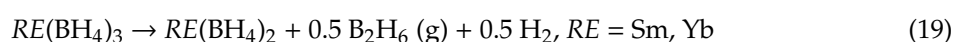
Solvent Free Synthesis of *REB*

The initial synthesis method for *REB* compounds was based on the reactions in Equation (17)–(18) and carried out by ball milling of a $RECl_3$ with an alkali borohydride (Li, Na, K). $LiBH_4$ has been proven to be the best precursor for this reaction [391–393].



However, the products obtained with this method are dependent on the ionic radius of the *RE* metal. *REB* compounds with four different structure types are formed [391,392]. Larger cations (La^{3+} - Sm^{3+}) form cubic spinel like $LiRE(BH_4)_3Cl$ structure with s.g. $I\bar{4}3m$ Equation (17) [63,394]. Slightly smaller cations, (Sm^{3+} - Yb^{3+}) form α and β - $RE(BH_4)_3$ with a rhenium oxide (ReO_3) structure type and space groups $Pa\bar{3}$ [395], $Pm\bar{3}m$ [396] or $Fm\bar{3}c$ [397], respectively (Equation (18)). The latter was derived from NPD and $Fm\bar{3}c$ is the DFT optimized s.g. for β - $RE(BH_4)_3$.

For Sm, α - and β - $Sm(BH_4)_3$ and small amounts of $LiSm(BH_4)_3Cl$ form after ball milling [254]. Heating the sample to $T \sim 180$ °C, reduced Sm^{3+} to Sm^{2+} and $Sm(BH_4)_2$ is formed. Attempts to synthesize europium borohydride with the ball milling method were unsuccessful and any known Eu-containing phases could not be identified in the XPD pattern after milling. Yb forms both α/β - $Yb(BH_4)_3$ and $LiYb(BH_4)_4$ and heating the sample to $T \sim 100$ °C forms $Yb(BH_4)_2$ based on reaction shown in Equation (19). The smallest cation (Lu^{3+}) acts as the strongest Lewis acid and forms $LiLu(BH_4)_4$ compound in s.g. $P\bar{4}2c$.



The structure types of most compounds of the Ln-series based on solvent free synthesis are summarized in Figure 21 with respect to cations ionic radii.

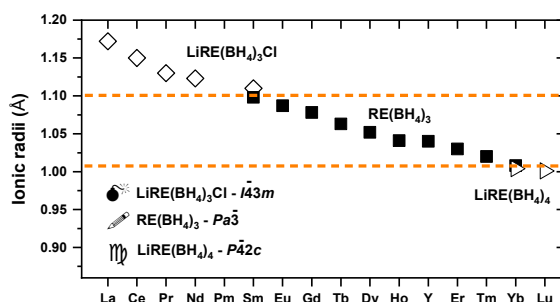


Figure 21. Overview of borohydride phases obtained by mechanochemical reactions of $RECl_3$ and $LiBH_4$. The ionic radius of RE^{3+} cations in the solid-state are displayed in octahedral environment [388]. Reproduced with permission from Wegner, W.; Jaron, T.; Grochala, W. Polymorphism and hydrogen discharge from holmium borohydride, $Ho(BH_4)_3$, and $KHo(BH_4)_4$. International Journal of Hydrogen Energy, 2014, 39, p. 20024-20030, Copyright (2014), with permission from Elsevier.

Solvent-Based Synthesis of REB

REB obtained by ball milling and the metathesis reaction shown in Equation (18) are contaminated with LiCl which acts as a ‘dead mass’ and decreases the active hydrogen content. Moreover, the formation of REB with larger cations was not possible via the solvent-free method. Therefore, solvent methods were developed to obtain pure rare earth borohydrides. In the latter, precursors are first reacted in a solvent i.e., toluene/ether which acts as a reaction medium to form $RE(BH_4)_3$ as per Equation (20):



After solvent removal, a second solvent i.e., dimethyl sulfide (DMS) is added to the mixture forming complex solvate $RE(BH_4)_3S(CH_3)_2$ that is soluble in DMS and allows the filtration of LiCl. Using this method, $RE(BH_4)_3$, $RE = La, Ce, Pr$ have been synthesized and allowed the formation of $Eu(BH_4)_2$ for the first time [398–400]. However, Payandeh et al. [401] found that the samples obtained are often contaminated with $LiBH_4$ due to the partial solubility of $LiBH_4$ in DMS. This contamination was observed for the first time in a $La(BH_4)_3$ compound which formed $Li_3K_3La_2(BH_4)_{12}$ upon reaction with KBH_4 .

The third method for synthesis of REB is based on the reaction of an ionic hydride REH_3 and a borane donating compound, e.g., $S(CH_3)_2BH_3$ based on Equations (21) and (22).



Using this method, $RE(BH_4)_3$, $RE = La, Ce$ and $Eu(BH_4)_2$ were synthesized and two high temperature polymorphs of $Eu(BH_4)_2$ were identified [400,402]. The crystal structures of $RE(BH_4)_n$ ($n = 2,3$) obtained by either solvent free or solvent method are summarized in Figure 22 and in the following section, the crystal structures of trivalent REB are presented and the relationship between the different structure types is discussed.

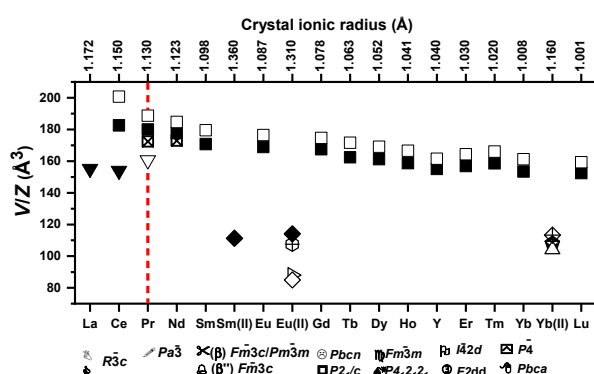


Figure 22. Unit cell volumes (V) of the reported rare earth borohydrides divided by the number of formula units (Z) [391,392,395,396,399,400,402–407] are presented. The ionic crystal radius were taken from [388]. The high-temperature polymorphs are displayed with empty signs. The figure was adapted from [408] with permission from The Royal Society of Chemistry.

3.6.2. Crystal Structures of Monometallic REB

In Figure 23, three major structure types of $RE(BH_4)_3$ are shown. All of them are of the cubic rhenium oxide (ReO_3) structure type in which Re atoms sit at the corner and O atoms at the edge. A wide selection of structures can be derived by coupled rotations of groups of octahedra. $Pa\bar{3}$ and $R\bar{3}c$ polymorphs are distorted ReO_3 structures but the $Fm\bar{3}c$ phase is an ideal cubic ReO_3 structure. The ReO_3 structure type is very closely related to the perovskite, $SrTiO_3$, without the Sr atoms placed in the

middle of the cube and therefore, having an empty void in this position, as shown in Figure 23b by the reddish sphere [409].

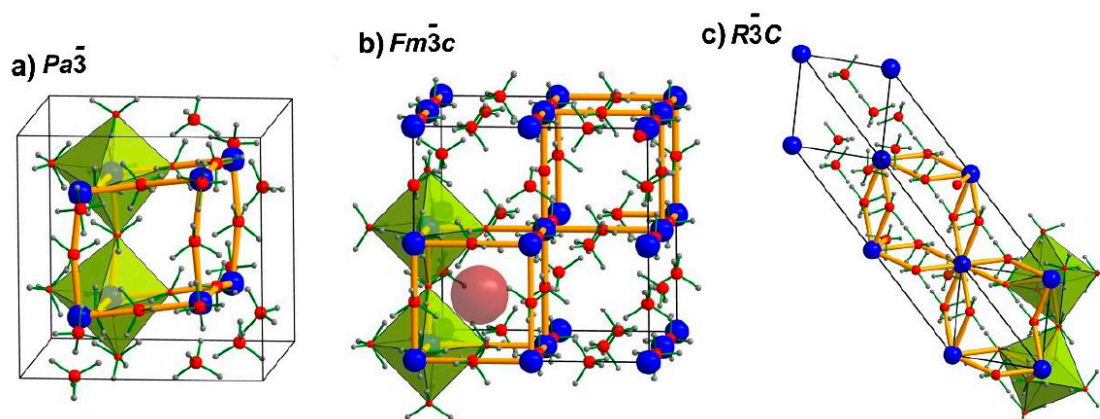


Figure 23. Crystal structures of trivalent rare earth borohydrides with space groups (a) $Pa\bar{3}$, (b) $Fm\bar{3}c$, (c) $R\bar{3}c$. The figure was adapted from [408] with permission from The Royal Society of Chemistry.

In all of the structures, RE atoms are coordinated to six BH_4^- in an octahedral geometry and all the BH_4^- groups are bridging between the RE^{3+} centers. $Pr(BH_4)_3$ is the only REB that shows all three polymorphs with different symmetries, i.e., $Pa\bar{3}$, $Fm\bar{3}c$ and $R\bar{3}c$. At RT, $Pr(BH_4)_3$ crystallizes in the s.g. $Pa\bar{3}$. Upon heating, the structure first unfolds and β - $Pr(BH_4)_3$ as ideal ReO_3 structure ($Fm\bar{3}c$) forms, but this polymorph is unstable and immediately transforms to r - $Pr(BH_4)_3$ with a smaller unit cell volume; this transformation is assigned to the large voids in the β -polymorph shown in Figure 23b by the reddish sphere. These voids allow the bending of the Pr–B–Pr bonds based on the rotation of $Pr(BH_4)_6$ octahedra. As a consequence, the Pr–B bond increases and the Pr–Pr bond distance decreases, which leads to contraction of the unit cell volume and stabilisation of r -phase ($R\bar{3}c$), which was found by Payandeh et al. [408].

However, performing the same experiment under elevated hydrogen pressure ($p(H_2) = 40$ bar) changes the polymorphic transition mechanism and β - $Pr(BH_4)_3$ as porous polymorph is stabilized as the major phase at 190 °C. Figure 22 shows that the crystal structures of the REB are dependent on the cation size, where praseodymium is a borderline element. When the cation size is smaller than Pr, the structure collapses and rhombohedral phase ($R\bar{3}c$) forms at RT which is due to formation of large voids in the structure, which collapse. However, when the metal cation is smaller such as neodymium, $Pa\bar{3}$ stabilizes as the RT phase.

3.6.3. Crystal Structures of Bimetallic REB

The structures of bimetallic rare earth borohydrides are more diverse and are presented in Table 4. While this chapter only discusses the selected compounds, further details can be found in [410]. Bimetallic $LiRE(BH_4)_3Cl$, $RE = Ce, Pr, Nd, Gd$ and $LiLa(BH_4)_3X$, $X = Cl, Br, I$ compounds have received significant attention due to their high ionic conductivity of $\sim 10^{-4} S cm^{-1}$ at RT. These compounds crystallize in cubic unit cell with a spinel-like structure and s.g. $I\bar{4}3m$ (No. 217), as has been reported by Payandeh et al. [411] and others [63,391]. In this structure $Z = 8$ and La, B, and X atoms fully occupy the 8c, 24g, and 8c Wyckoff sites. However, Li-ions occupy the 12d sites and in order to maintain the charge neutrality, the occupancy should be 2/3. In this structure, anions, $[La_4X_4(BH_4)_{12}]^{4-}$, as isolated tetranuclear anionic clusters exist and these contain a distorted cubane-like $La_4 \times 4$ core. Furthermore, those are charge-balanced by Li^+ cations (Figure 24b). Li ions, which are coordinated tetrahedrally to four BH_4^- groups via the tetrahedral edge and lanthanum atoms octahedrally coordinate to three halide ions and three borohydride groups via the faces ($\eta 3$) and form a distorted octahedron.

Table 4. Structural classification of bimetallic rare earth *REB*, their structural prototype and their properties (updated version of Table 2 in [410]).

M_2	M_1	$M_1M_2(BH_4)_n$ $M_1M_2(BH_4)_nCl_z$	Structure	Structural Prototype	Investigated Application, Reference
La	Li	c-LiLa(BH ₄) ₃ Cl	$\bar{I}43m$	Spinel	Li ion conductivity, [63,391]
		c-LiLa(BH ₄) ₃ Br	$\bar{I}43m$	Spinel	Li ion conductivity, [411]
		c-LiLa(BH ₄) ₃ I	$\bar{I}43m$	Spinel	Li ion conductivity, [411]
	Na	o-NaLa(BH ₄) ₄	<i>Pbcn</i>	New	Hydrogen storage, [412]
	K	m-K ₃ La(BH ₄) ₆	$P2_1/n$	<i>rt</i> -Na ₃ AlF ₆	Hydrogen storage, [412]
Ce	Li	c-LiCe(BH ₄) ₃ Cl	$\bar{I}43m$	Spinel	Li ion conductivity, [394,413]
	Na	o-NaCe(BH ₄) ₄	<i>Pbcn</i>	Own	Hydrogen storage, [401]
	K	m-K ₃ Ce(BH ₄) ₆	$P2_1/n$	<i>rt</i> -Na ₃ AlF ₆	Hydrogen storage, [414]
	Rb	m-Rb ₃ Ce(BH ₄) ₆	$P2_1/n$	<i>rt</i> -Na ₃ AlF ₆	not specified, [415]
Pr	Li	c-LiPr(BH ₄) ₃ Cl	$\bar{I}43m$	Spinel	not specified, [391]
	Na	o-NaPr(BH ₄) ₄	<i>Pbcn</i>	Own	Hydrogen storage, [401]
Nd	Li	c-LiNd(BH ₄) ₃ Cl	$\bar{I}43m$	Spinel	not specified, [391]
Sm	Li	c-LiSm(BH ₄) ₄ Cl	$\bar{I}43m$	Spinel	not specified, [391]
	K	o-KSm(BH ₄) ₃	$P2_1cn$	CdTiO ₃	Hydrogen storage, [416]
	Rb	o-RbSm(BH ₄) ₃	$Pbn2_1$	CdTiO ₃	Hydrogen storage, [416]
	Cs	o-CsSm(BH ₄) ₃	$P22_12_1$	NaNbO ₃	Hydrogen storage, [416]
Eu	Rb	o-RbEu(BH ₄) ₃	$Pbn2_1/Pna2_1$	CdTiO ₃	not specified, [415]
	Cs	t-CsEu(BH ₄) ₃	$P4/m3m$	NaNbO ₃	Luminescence, [415]
Gd	Li	c-LiGd(BH ₄) ₃ Cl	$\bar{I}43m$	Spinel	Li ion conductivity, [63,391]
		m-KGd(BH ₄) ₄	$P2_1/c$	LiMnF ₄	<i>Magneto-calorimetry</i> , [417]
		m-K ₂ Gd(BH ₄) ₅	$P2_1/m$	Own	<i>Magneto-calorimetry</i> , [417]
	K	m-K ₃ Gd(BH ₄) ₆	$P2_1/n$	<i>rt</i> -Na ₃ AlF ₆	<i>Magneto-calorimetry</i> , [417]
		c-Cs ₃ Gd(BH ₄) ₆	$Fm\bar{3}$	(NH ₄) ₃ AlF ₆	<i>Magneto-calorimetry</i> , [415]
Ho	K	o-KHo(BH ₄) ₄	<i>Cmcm</i>	<i>ht</i> -CrVO ₄	not reported, [403]
Y	Li	t-LiY(BH ₄) ₄	$P\bar{4}2c$	CuAlCl ₄	Li ion conductivity, [418,419]
		o-NaY(BH ₄) ₄	$C222_1$	<i>ht</i> -CrVO ₄	Na ion conductivity, [418,419]
	Na	m-NaY(BH ₄) ₂ Cl ₂	$P2/c$	MgWO ₄	not specified, [420]
		o-KY(BH ₄) ₄	<i>Cmcm</i>	<i>ht</i> -CrVO ₄	not specified, [421]
		m-KY(BH ₄) ₄	$C2/c$	<i>rt</i> -LaNbO ₄	not specified, [422]
	K	o-RbY(BH ₄) ₄	<i>Pnma</i>	BaSO ₄	not specified, [422]
		m-RbY(BH ₄) ₄	$P2_1/c$	AgMnO ₄ (deformed BaSO ₄)	not specified, [423]
	Cs	c-Rb ₃ Y(BH ₄) ₆	$Fm\bar{3}$	(NH ₄) ₃ AlF ₆	not specified, [415,422]
		c-CsY(BH ₄) ₄	$I4_1/a$	CaWO ₄ -scheelite	not specified, [423]
c-Cs ₃ Y(BH ₄) ₆		$Fm\bar{3}$	(NH ₄) ₃ AlF ₆	not specified, [415,422]	
Er	Na	o-NaEr(BH ₄) ₄	<i>Cmcm</i>	<i>ht</i> -CrVO ₄	Hydrogen storage, [401]
	K	o-KEr(BH ₄) ₄	<i>Cmcm</i>	<i>ht</i> -CrVO ₄	not specified, [424]
Yb	Li	c-LiYb(BH ₄) ₃ Cl	$P\bar{4}2c$	CuAlCl ₄	not specified, [392]
	Na	o-NaYb(BH ₄) ₄	<i>Cmcm</i>	<i>ht</i> -CrVO ₄	not specified, [425]
	K	o-KYb(BH ₄) ₄	<i>Cmcm</i>	<i>ht</i> -CrVO ₄	not specified, [425]
		c-KYb(BH ₄) ₃ - <i>rt</i>	$P\bar{4}3m$	CaTiO ₃	Luminescence, [415]
	o-KYb(BH ₄) ₃ - <i>ht</i>	$Pm2_1b$	New	not specified, [415]	
Lu	Li	t-LiLu(BH ₄) ₄	$P\bar{4}2c$	CuAlCl ₄	not specified, [391]

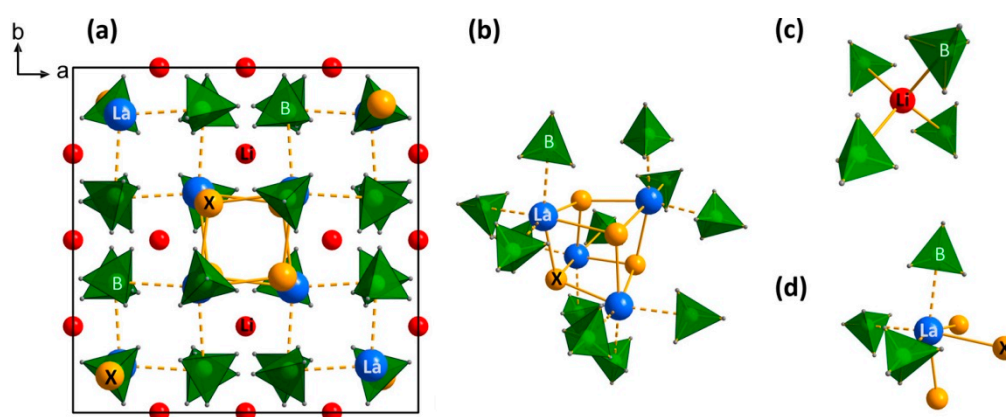


Figure 24. Crystal structure of $\text{LiRE}(\text{BH}_4)_3\text{Cl}$, $\text{RE} = \text{Ce}, \text{Pr}, \text{Nd}, \text{Gd}$ and $\text{LiLa}(\text{BH}_4)_3\text{X}$, $\text{X} = \text{Cl}, \text{Br}, \text{I}$ compounds. (b) Isolated tetranuclear anionic clusters $[\text{RE}_4\text{X}_4(\text{BH}_4)_{12}]^{4-}$ with a distorted cubane La_4X_4 core and (c) tetrahedral coordination of Li to four BH_4 groups. (d) Octahedral La coordination to three BH_4 groups and three X atoms. Symbols: La, blue sphere; halide X, yellow sphere; Li, red sphere; green tetrahedrons are BH_4 anions with a whitish sphere (boron) inside and hydrogen on the corners. Adapted with permission from GharibDoust, S., M. Brighi, Y. Sadikin, D.B. Ravnsbæk, R. Černý, T. Jensen, and J. Skibsted, Synthesis, Structure and Li Ion Conductivity of $\text{LiLa}(\text{BH}_4)_3\text{X}$, $\text{X} = \text{Cl}, \text{Br}, \text{I}$. J. Phys. Chem. C, 2017. 121: pp. 19010–19021. Copyright (2017) American Chemical Society.

Partial lithium occupancy leads to a high lithium-ion conductivity for these types of compounds. Moreover, it has been found that the conduction channel can be tuned by changing the anions in the structure and the optimized size of channel is suggested when bromide is used as anion. However, unlike $\text{LiLa}(\text{BH}_4)_3\text{X}$, $\text{X} = \text{Cl}, \text{I}$ samples, the bromide-containing sample is not stable and slowly decomposes to $\text{La}(\text{BH}_4)_3$ and LiBr over time.

The $\text{NaRE}(\text{BH}_4)_4$, $\text{RE} = \text{La}, \text{Ce}, \text{Pr}$, compounds crystallize in a new structure type with orthorhombic unit cell and s.g. $Pbcn$, (Figure 25a). In this structure, both Na and RE atoms have an octahedral coordination to BH_4^- units. Two distinct types of BH_4^- anions with coordination number of three exist in this structure. The first one bridges between two RE atoms and one Na atom. The second one bridges between two Na atoms and one RE atom, which creates a zig-zag chain of edge sharing $\text{Na}(\text{BH}_4)_6$ octahedra connected with edge sharing $\text{La}(\text{BH}_4)_6$ octahedra along the c-axis. The latter as a new type of structure for REB built from brucite-like layers of octahedra (*hcp* of anions) was reported by Payandeh et al. [412] with half of the octahedral sites empty. Similar octahedral chains have been observed for $\alpha\text{-PbO}_2$ (zig-zag chains) and rutile (straight chains).

The second group of $\text{NaRE}(\text{BH}_4)_4$, $\text{RE} = \text{Y}, \text{Er}, \text{Yb}, \text{Sc}$, with smaller size of rare earth cations crystallize in the s.g. $Cmcm$ (Figure 25b). The structure consists of $\text{RE}(\text{BH}_4)_4^-$ anions and Na^+ cations, forming a distorted trigonal prism around the complex anion. RE atoms have tetrahedral coordination to BH_4^- units while Na atoms have octahedral coordination to BH_4^- and from edge-sharing $\text{K}(\text{BH}_4)_6$ octahedral chains along c-axis, see Figure 25b [403].

Figure 25c presents the unit cell volume per formula unit V/Z of the bimetallic sodium rare earth borohydride. Bimetallic borohydrides with bigger rare earth cations (La, Ce, Pr) crystallize in s.g. $Pbcn$ and have a smaller unit cell volume whereas borohydrides with smaller rare earth cations (Y, Er, Yb) crystallize in s.g. $Cmcm$ or $C222_1$ with a larger unit cell volume. $\text{NaGd}(\text{BH}_4)_4$ forms an amorphous yet unstable phase. In s.g. $Pbcn$, both cations have the coordination number six, which leads to denser packing and smaller unit cell volume for these structures. Moreover, the unit cell volume of bimetallic borohydrides can be related to the unit cell volume of REB. As shown in Figure 22, bigger rare earth cations ($\text{RE} = \text{La}, \text{Ce}$) crystallize in the rhombohedral unit cell with s.g. $R\bar{3}c$ and V/Z in the range of 154.0–155.2 \AA^3 . However, smaller rare earth cations ($\text{RE} = \text{Nd-Yb}$) crystallize in a cubic unit cell with s.g. $P\bar{a}3$ and larger V/Z in the range of 183–153.4 \AA^3 . Therefore, when rare earth borohydrides ($\text{RE} = \text{La}, \text{Ce}$) with rhombohedral unit cell ($R\bar{3}c$) react with NaBH_4 , bimetallic borohydrides with smaller unit cell

volume and *Pbcn* symmetry form [412]. However, the reaction between *REB* with cubic unit cell ($P\bar{a}3$, $RE = \text{Nd-Yb}$) and NaBH_4 forms bimetallic compounds with space group symmetry $C222_1$ or $Cmcm$ and larger unit cell volume. $\text{Pr}(\text{BH}_4)_3$ is the only rare earth borohydride with a cubic unit cell at RT ($P\bar{a}3$) that undergoes a polymorphic transition to a rhombohedral phase ($R\bar{3}c$) at $T \sim 190^\circ\text{C}$. This transition is accompanied by a significant contraction in the unit cell volume. The reaction between NaBH_4 and $\text{Pr}(\text{BH}_4)_3$ occurs at elevated temperatures and therefore, the formation of $\text{NaPr}(\text{BH}_4)_4$ compound with s.g. *Pbcn* is suggested to be a reaction between NaBH_4 and the rhombohedral polymorph of $\text{Pr}(\text{BH}_4)_3$ ($R\bar{3}c$) [401].

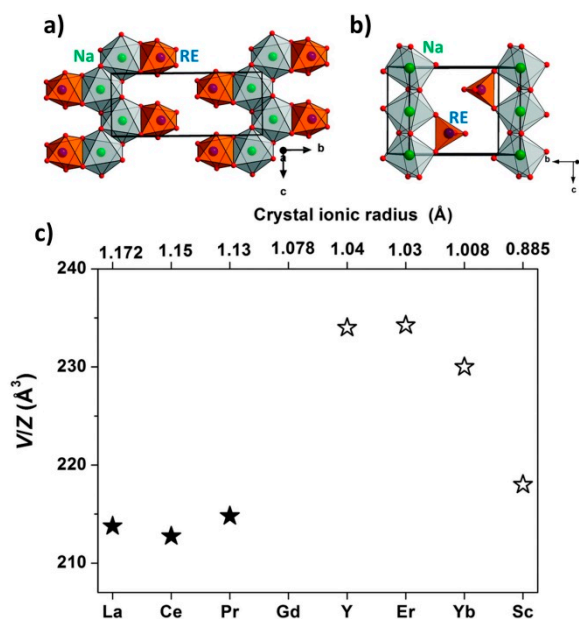
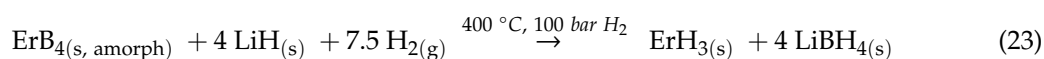


Figure 25. Crystal structures of (a) $\text{NaRE}(\text{BH}_4)_4$, $RE = \text{La, Ce, Pr}$ and (b) $\text{NaRE}(\text{BH}_4)_4$, $RE = \text{Y, Er, Yb, Sc}$. RE : blue, Na: green, and B: red. H atoms are removed for clarity. (c) The unit cell volumes per formula unit, V/Z , of the known bi-metallic sodium rare earth borohydrides. Symbols: ★, $\text{NaRE}(\text{BH}_4)_4$, $RE = \text{La, Ce, Pr}$ (*Pbcn*) and ☆, $\text{NaRE}(\text{BH}_4)_4$, $RE = \text{Y, Er, Yb, Sc}$ ($C222_1$ or $Cmcm$). The figure was adapted from [401] with permission from The Royal Society of Chemistry.

3.6.4. Reactive Hydride Composites with *REB*

In this section, the hydrogen storage properties of selected $\text{RE}(\text{BH}_4)_3$ are investigated. Previous reports showed that in $\text{Er}(\text{BH}_4)_3$, synthesized by mechanochemical milling of $\text{ErCl}_3 + \text{LiBH}_4$, up to 20% of the initial released hydrogen could be re-hydrogenated [426]. However, an explanation of reaction products was not given. In order to gain better insight into the reaction mechanism, $\text{Er}(\text{BH}_4)_3$ was synthesized based on solvent methods. Surprisingly, for this pure $\text{Er}(\text{BH}_4)_3$ no reabsorption of hydrogen could be observed after initial decomposition and re-hydrogenation, and only amorphous decomposition products ErB_4 and ErH_n , $n = 2, 3$ were expected to form.

However, Heere et al. [406] showed that by mixing 50 wt % LiH into these decomposition products and applying re-hydrogenation, ErH_3 and LiBH_4 were formed, monitored by in situ SR-XPD (Figure 26). In summary, the re-hydrogenation can only be achieved in combination with a lithium source. Therefore, 20 wt % re-hydrogenation of $\text{Er}(\text{BH}_4)_3$ observed by the aforementioned report is attributed to the contamination with LiBH_4 from solvent-free synthesis. The latter forms LiH during decomposition and enables the re-hydrogenation reaction, as shown in Equation (23).



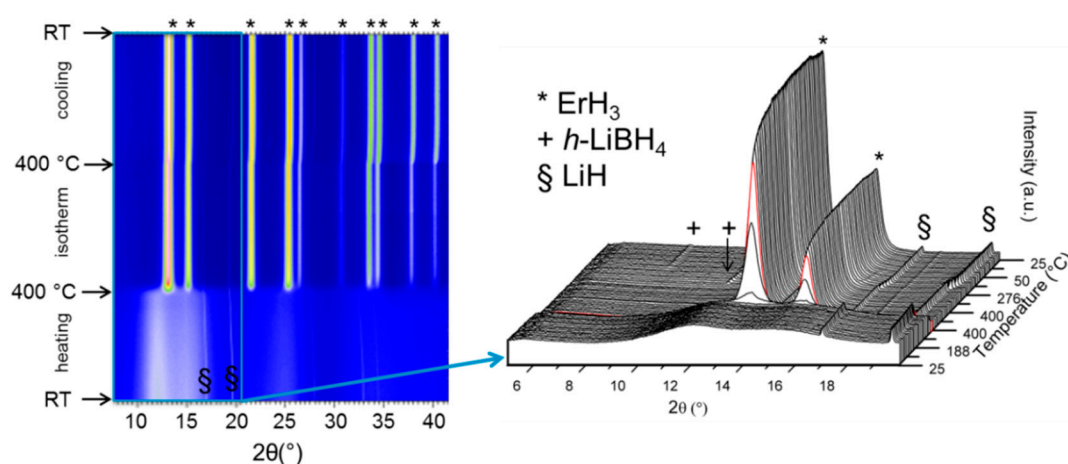
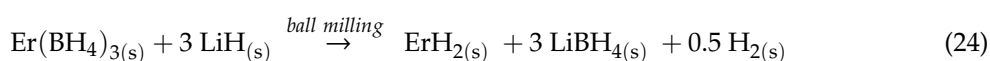
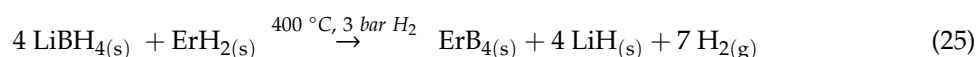


Figure 26. In situ SR-XPD data of a composite containing desorbed $\text{Er}(\text{BH}_4)_3 + 50 \text{ wt } \% \text{ LiH}$. The composite was thermally treated from RT to 400 °C with a 1 h isotherm and cooling to RT, all in $p(\text{H}_2) = 100 \text{ bar}$ (temperature ramp of $5 \text{ }^\circ\text{C min}^{-1}$). Inset showing magnification of the 2θ range 5 to 20° to enhance the visibility of the appearance of Bragg peaks for $h\text{-LiBH}_4$ (+). The red curve in the magnification marks the end temperature of 400 °C. $\lambda = 0.69733 \text{ \AA}$. The figure was adapted from [406], published by the PCCP Owner Societies.

Additionally, two composites were investigated, $\text{Er}(\text{BH}_4)_3\text{-6LiH}$ and $3\text{LiBH}_4\text{-Er}(\text{BH}_4)_3\text{-3LiH}$. The reactants were ball milled for 1 h and in both samples, ErH_2 forms after milling which suggests a reaction between $\text{Er}(\text{BH}_4)_3$ and LiH based on Equation (24):



Desorption of the samples was performed at $T = 400 \text{ }^\circ\text{C}$ under $p(\text{H}_2) = 3 \text{ bar}$ followed by a 12 h isotherm and the XPD pattern of the samples after decomposition revealed the formation of LiH and ErB_4 based on Equation (25):



In the next step, absorption was conducted for 12 h at 340 °C and $p(\text{H}_2) = 100 \text{ bar}$. The formation of LiBH_4 and ErH_3 from the XPD pattern after absorption suggests the hydrogen uptake based on the Equation (23).

The hydrogen release and uptake of the $3\text{LiBH}_4\text{-Er}(\text{BH}_4)_3\text{-3LiH}$ composite was studied by Heere et al. by a Sieverts' apparatus and the results are presented in Figure 27 [427]. This composite has a hydrogen storage capacity of 9 wt %, but, only 6 wt % of hydrogen can be released at a moderate temperature due to the formation of stable LiH . Figure 27 shows that 4.2 wt % of H_2 is released in the first desorption. The second and third desorption cycles released 3.7 and 3.5 wt % H_2 , respectively, which are equivalent to 88.1% and 83.3% of the initial hydrogen release [427].

In conclusion, the hydrogen storage properties in these mixtures are attributed to the reformation of LiBH_4 based on the reaction of REB_4 and LiH . The pure REB are not promising candidates for hydrogen storage properties and more favourable results can be obtained by mixing rare earth borides/hydrides with alkali metal borohydrides such as LiBH_4 , which facilitates their re-hydrogenation at milder hydrogenation conditions.

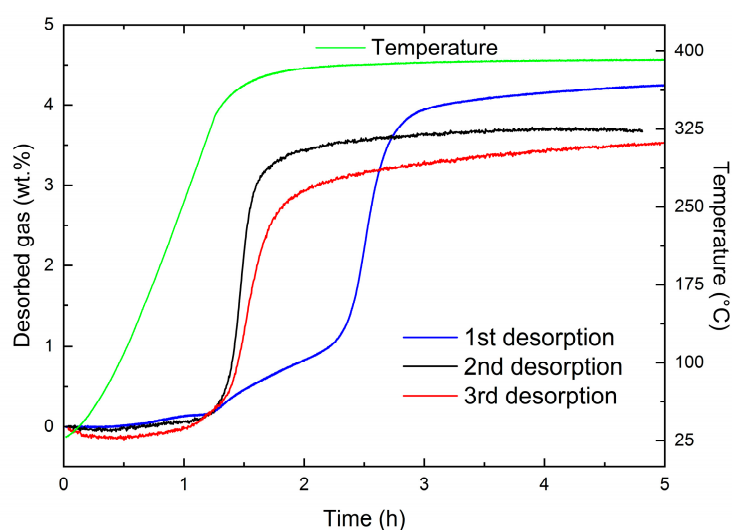


Figure 27. Sieverts' measurement for $3\text{LiBH}_4\text{-Er}(\text{BH}_4)_3\text{-3LiH}$. $p(\text{H}_2) = 5\text{--}10$ bar. The samples were treated from RT to $400\text{ }^\circ\text{C}$ ($\Delta T/\Delta t = 5\text{ }^\circ\text{C min}^{-1}$).

3.6.5. Conclusions

Research on rare earth borohydrides is further increasing due to their potential as energy materials for applications including hydrogen storage and solid-state ion conductors for battery applications. Li ionic conductivities of 10^{-4} S cm^{-1} in $\text{LiRE}(\text{BH}_4)_3\text{X}$ ($\text{RE} = \text{La, Ce, Gd}$; $\text{X} = \text{Cl, Br, I}$ [63,411,413]) have been observed, which is about three magnitudes higher than conductivities for $o\text{-LiBH}_4$ at RT [63]. Similar conductivity values have been observed for the $h\text{-LiBH}_4\text{-LiX}$ with $\text{X} = \text{Cl, Br, I}$ [75,80]. Recently, ternary borohydrides including new garnet type materials, $\text{Li}_3\text{K}_3\text{Ce}_2(\text{BH}_4)_{12}$ and $\text{Li}_3\text{K}_3\text{La}_2(\text{BH}_4)_{12}$ [414], have been explored by **Brighi et al.** as Li ion conductors with a conductivity value of 10^{-5} S cm^{-1} . All those σ values are in the range of their corresponding oxide garnets, such as $\text{Li}_5\text{La}_3\text{Ta}_2\text{O}_{12}$ with $\sigma = 10^{-6}\text{ S cm}^{-1}$ at RT [428].

REB show further interesting properties for applications within the optical and the magnetic field. Marks et al. [429] investigated $\text{RE}(\text{BH}_4)_2(\text{THF})_2$ ($\text{RE} = \text{Eu, Yb}$) and showed that the $\text{RE} = \text{Eu}$ compound exhibits a bright blue luminescence. Magnetic properties have been investigated and magnetic entropy change of $54.6\text{ J kg}^{-1}\text{ K}^{-1}$ at a magnetic field change of 9 T has been reported for $\text{K}_2\text{Gd}(\text{BH}_4)_5$ [404,417,430].

This chapter reviewed recent accomplishments in selected *RE* borohydrides. The synthesis routes for solvent-free, halide-free and solvent- and halide-free *RE* borohydrides were discussed, along with the properties of mono- and bi-metallic *RE* borohydrides and *RE* borohydrides in composite mixtures, while a special focus was given to hydrogen storage properties and reaction pathways.

4. Final Conclusions and Outlook

The review gives an overview of recently achieved milestones within the research of metal hydrides with respect to promising applications in all-solid-state batteries and complex metal hydrides for solid-state hydrogen storage.

Generally, under the framework of this project, the performance of metal hydrides were improved at higher temperatures thanks to the fact that mass transportation within the electrode was enhanced compared to RT cycling, which suggests that electrodes and electrolytes from metal hydrides might be initially realized for high temperature applications. The application of metal hydride anodes and hydride complexes in LiBs and particularly in all-solid-state cells were presented. The mechanism and internal behaviour of the hydride anodes in LiBs were also elucidated. Interestingly, the first full all-solid-state lithium metal hydride-lithium sulfur cell was successfully assembled and cycled with a promising performance. New metal hydride complexes were also discovered and studied with

high lithium ionic conductivity and stability for application as solid electrolytes, i.e., the borohydride substituted argyrodite $\text{Li}_6\text{PS}_5\text{X}_{1-y}(\text{BH}_4)_y$, and a cluster complex hydride $\text{LiBH}_4\text{-Li}_2\text{NH}$: $\text{Li}_5(\text{BH}_4)_3\text{NH}$. Other potential complex hydrides, including sodium *closo*-borates, as solid-state electrolytes were shown, which are viable alternatives satisfying many needs. In this context a mixed-hydroborate-anion developed by Duchêne et al., $\text{Na}_2(\text{B}_{10}\text{H}_{10})_{0.5}(\text{B}_{12}\text{H}_{12})_{0.5}$ [133], was used as proof-of-concept for a 3 V all-solid-state sodium ion battery. In the future, new cage structures will be investigated such as the recently published *nido*-borate (i.e., $\text{NaB}_{11}\text{H}_{14}$) by Payandeh et al. [431], which can be synthesized directly from rather cheap NaBH_4 and have been employed also in combination with *closo*-borates. Other working ions such as Mg are also promising, as a new compound synthesized from $\text{Mg}(\text{BH}_4)_2$ and ethylenediamine has been shown to have an exceptionally high conductivity of up to $6 \times 10^{-5} \text{ S cm}^{-1}$ at 70 °C in the solid state [432]. A follow up with different organic complexes reported details on conductivities with a particular focus on the dynamics of $\text{Mg}(\text{BH}_4)_2\text{-diglyme}_{0.5}$ [433], while Ruyet et al. [434] revealed a high conductivity of $3 \times 10^{-6} \text{ S cm}^{-1}$ at 100 °C for a solid-state Mg conductor based on $\text{Mg}(\text{BH}_4)(\text{NH}_2)$. The achievements summarized herein put the aforementioned complex hydrides as valid competitors to other solid electrolytes, like oxides and thiophosphates, while their investigation will remain a highly interesting topic.

At the same time, hydrogen as energy carrier will be used more dominantly in the future. Japan will employ hydrogen during the Olympic Games 2020 and will show how a hydrogen economy can be implemented in all parts of life. From generating “green and renewable” hydrogen via electrolysis, through the transport of people in hydrogen powered cars and buses, to warm water production for the sustainable use of heat from fuel cells. New applications are vital for strongly required infrastructures such as hospitals, which, in the case of earthquakes and tsunamis, are not allowed to use Diesel powered generators (in Japan). Already today, back-up systems in hospitals work with fuel cells and hydrogen is stored within metal hydride alloy storage units, which supply energy and warm water, when centralized energy supply is failing. Therefore, an energy storage system as a role model for our intermittent “green and renewable” energy sources could be realized from metal hydrides.

Author Contributions: Conceptualization, writing—original draft preparation, M.H.; writing—review and editing E.H., T.T.L. and M.H., writing—original Section 2.1., A.H.D., N.B. and P.H.; writing—original Section 2.2., M.B.; writing—original Section 3.1., E.H.; writing—original Section 3.2., E.M.D., A.R.W. and A.S.; writing—original Section 3.3., E.M.D. and Y.L.; writing—original Section 3.4., T.T.L.; writing—original Section 3.5., F.P.; writing—original Section 3.6., S.P. and M.H. All authors have read and agreed to the published version of the manuscript.

Funding: The research leading to these results has received funding from the People Program Marie Skłodowska-Curie Actions(MSCA) of the European Union’s Seventh Framework Program FP7/2007–2013/under REA grant agreement n° 607040 (MSCA ITN ECOSTORE).

Acknowledgments: During this Marie Skłodowska-Curie Actions funded EU project ECOSTORE thirteen PhD thesis arose. All these theses investigated different aspects of material advances in battery materials and hydrogen storage materials for an efficient and compact storage of renewable energy. All former students would like to acknowledge the contribution and support of their respective PhD supervisor, namely, Magnus H. Sørby & Bjørn C. Hauback (Institute for Energy Technology (IFE), Norway); Torben Jensen (University of Aarhus, Denmark); Dorthe Ravnsbæk (University of Southern Denmark, Denmark); Fermín Cuevas & Michel Latroche (Institut de Chimie et des Matériaux Paris Est, France); Marcello Baricco (University of Turino, Italy); Claudio Pistidda, Thomas Klassen & Martin Dornheim (Helmholtz-Zentrum Geesthacht, Germany); Theodore Steriotis & Georgia Charalambopoulou (NCSR “Demokritos”, Greece); Guido Schmitz (University of Stuttgart, Germany); Radovan Černý (University of Geneva, Switzerland); and David Book & Daniel Reed (University of Birmingham, Great Britain), as well as the consulting partners in Japan, Shin-Ichi Orimo, Etsuo Akiba and Hai-Wen Li. The industrial partners Saft, former Rockwood Lithium (now Albemarle) and ZOZ are acknowledged as well. All partners and students made it a very vibrant innovative training network. Last but not least, the two most important personalities responsible for the project coordination, Klaus Taube, and our secretary Sigrid Wulff have to be thanked deeply, as this project and its success would not have been possible without them!

Conflicts of Interest: The authors declare no conflict of interest. The funders had no role in the design of the study; in the collection, analyses, or interpretation of data; in the writing of the manuscript, or in the decision to publish the results.

References

1. Yoshida, T.; Kojima, K. Toyota MIRAI fuel cell vehicle and progress toward a future hydrogen society. *Interface Mag.* **2015**, *24*, 45–49. [CrossRef]
2. Pillot, C. The rechargeable battery market and main trends 2014–2015. *Avicenne Energy* **2015**. Available online: http://www.avicenne.com/pdf/Fort_Lauderdale_Tutorial_C_Pillot_March2015.pdf (accessed on 21 February 2020).
3. Poupin, L.; Humphries, T.D.; Paskevicius, M.; Buckley, C.E. An experimental high temperature thermal battery coupled to a low temperature metal hydride for solar thermal energy storage. *Sustain. Energy Fuels* **2020**, *4*, 285–292. [CrossRef]
4. Zhao-Karger, Z.; Fichtner, M. Beyond intercalation chemistry for rechargeable mg batteries: A short review and perspective. *Front. Chem.* **2018**, *6*, 656. [CrossRef] [PubMed]
5. Elia, G.A.; Marquardt, K.; Hoepfner, K.; Fantini, S.; Lin, R.; Knipping, E.; Peters, W.; Drillet, J.F.; Passerini, S.; Hahn, R. An overview and future perspectives of aluminum batteries. *Adv. Mater.* **2016**, *28*, 7564–7579. [CrossRef] [PubMed]
6. Janek, J.; Zeier, W.G. A solid future for battery development. *Nat. Energy* **2016**, *1*, 300. [CrossRef]
7. Tarascon, J.M. Key challenges in future Li-battery research. *Philos. Trans. A Math. Phys. Eng. Sci.* **2010**, *368*, 3227–3241. [CrossRef]
8. Tarascon, J.M.; Armand, M. Issues and challenges facing rechargeable lithium batteries. *Nature* **2001**, *414*, 359–367. [CrossRef]
9. S. C. 50th A. P. Team. *Sony History*, 1996th ed.; Sony Corporation, 1996; Available online: <https://www.sony.net/SonyInfo/CorporateInfo/History/SonyHistory/2-13.html> (accessed on 21 February 2020).
10. Li, C.; Zhang, H.P.; Fu, L.J.; Liu, H.; Wu, Y.P.; Ram, E.; Holze, R.; Wu, H.Q. Cathode materials modified by surface coating for lithium ion batteries. *Electrochim. Acta* **2006**, *51*, 3872–3883. [CrossRef]
11. Kraytsberg, A.; Ein-Eli, Y. Higher, stronger, better ... A review of 5 volt cathode materials for advanced lithium-ion batteries. *Adv. Energy Mater.* **2012**, *2*, 922–939. [CrossRef]
12. Shetti, N.P.; Dias, S.; Reddy, K.R. Nanostructured organic and inorganic materials for Li-ion batteries: A review. *Mater. Sci. Semicond. Process.* **2019**, *104*, 104684. [CrossRef]
13. Liu, M.; Deng, N.; Ju, J.; Fan, L.; Wang, L.; Li, Z.; Zhao, H.; Yang, G.; Kang, W.; Yan, J. A review: Electrospun nanofiber materials for lithium-sulfur batteries. *Adv. Funct. Mater.* **2019**, *29*. [CrossRef]
14. Wang, H.; Yang, Y.; Liang, Y.; Robinson, J.T.; Li, Y.; Jackson, A.; Cui, Y.; Dai, H. Graphene-Wrapped sulfur particles as a rechargeable lithium-sulfur battery cathode material with high capacity and cycling stability. *Nano Lett.* **2011**, *11*, 2644–2647. [CrossRef] [PubMed]
15. Myung, S.T.; Maglia, F.; Park, K.J.; Yoon, C.S.; Lamp, P.; Kim, S.J.; Sun, Y.K. Nickel-Rich layered cathode materials for automotive lithium-ion batteries: Achievements and perspectives. *ACS Energy Lett.* **2017**, *2*, 196–223. [CrossRef]
16. Oumellal, Y.; Rougier, A.; Nazri, G.A.; Tarascon, J.M.; Aymard, L. Metal hydrides for lithium-ion batteries. *Nat. Mater.* **2008**, *7*, 916–921. [CrossRef]
17. Aymard, L.; Oumellal, Y.; Bonnet, J.P. Metal hydrides: An innovative and challenging conversion reaction anode for lithium-ion batteries. *Beilstein J. Nanotechnol.* **2015**, *6*, 1821–1839. [CrossRef]
18. Braga, M.H.; Grundish, N.S.; Murchison, A.J.; Goodenough, J.B. Alternative strategy for a safe rechargeable battery. *Energy Environ. Sci.* **2017**, *10*, 331–336. [CrossRef]
19. Varzi, A.; Raccichini, R.; Passerini, S.; Scrosati, B. Challenges and prospects of the role of solid electrolytes in the revitalization of lithium metal batteries. *J. Mater. Chem. A* **2016**, *4*, 17251–17259. [CrossRef]
20. Sartori, S.; Cuevas, F.; Latroche, M. Metal hydrides used as negative electrode materials for Li-ion batteries. *Appl. Phys. A Mater. Sci. Process.* **2016**, *122*, 135. [CrossRef]
21. Brutti, S.; Mulas, G.; Piciollo, E.; Panero, S.; Reale, P. Magnesium hydride as a high capacity negative electrode for lithium ion batteries. *J. Mater. Chem.* **2012**, *22*, 14531–14537. [CrossRef]
22. Yang, S.; Wang, H.; Ouyang, L.; Liu, J.; Zhu, M. Improvement in the Electrochemical lithium storage performance of MgH₂. *Inorganics* **2018**, *6*, 2. [CrossRef]
23. Oumellal, Y.; Zaidi, W.; Bonnet, J.P.; Cuevas, F.; Latroche, M.; Zhang, J.; Bobet, J.L.; Rougier, A.; Aymard, L. Reactivity of TiH₂ hydride with lithium ion: Evidence for a new conversion mechanism. *Int. J. Hydrog. Energy* **2012**, *37*, 7831–7835. [CrossRef]

24. Teprovich, J.A.; Zhang, J.; Colón-Mercado, H.; Cuevas, F.; Peters, B.; Greenway, S.; Zidan, R.; Latroche, M. Li-Driven electrochemical conversion reaction of AlH_3 , LiAlH_4 , and NaAlH_4 . *J. Phys. Chem. C* **2015**, *119*, 4666–4674. [[CrossRef](#)]
25. Silvestri, L.; Forgia, S.; Farina, L.; Meggiolaro, D.; Panero, S.; La Barbera, A.; Brutti, S.; Reale, P. Lithium alanates as negative electrodes in lithium-ion batteries. *ChemElectroChem* **2015**, *2*, 877–886. [[CrossRef](#)]
26. Silvestri, L.; Farina, L.; Meggiolaro, D.; Panero, S.; Padella, F.; Brutti, S.; Reale, P. Reactivity of sodium alanates in lithium batteries. *J. Phys. Chem. C* **2015**, *119*, 28766–28775. [[CrossRef](#)]
27. Ptashnik, V.B.; Dunaeva, T.Y.; Baikov, Y.M. The Electrical Conductivity of Solid Lithium Hydride Doped with Sulphur. *Phys. Status Solidi B* **1982**, *110*, K121–K124. [[CrossRef](#)]
28. Berti, N.; Hadjixenophontos, E.; Cuevas, F.; Zhang, J.; Lacoste, A.; Dubot, P.; Schmitz, G.; Latroche, M. Thin films as model system for understanding the electrochemical reaction mechanisms in conversion reaction of MgH_2 with lithium. *J. Power Sources* **2018**, *402*, 99–106. [[CrossRef](#)]
29. Huen, P.; Ravnsbæk, D.B. Insight into poor cycling stability of MgH_2 anodes. *J. Electrochem. Soc.* **2017**, *164*, A3138–A3143. [[CrossRef](#)]
30. Huang, L.; Aymard, L.; Bonnet, J.-P. MgH_2 - TiH_2 mixture as an anode for lithium-ion batteries: Synergic enhancement of the conversion electrode electrochemical performance. *J. Mater. Chem. A* **2015**, *3*, 15091–15096. [[CrossRef](#)]
31. Ito, M.; Setoyama, D.; Matsunaga, J.; Muta, H.; Kurosaki, K.; Uno, M.; Yamanaka, S. Electrical and thermal properties of titanium hydrides. *J. Alloys Compd.* **2006**, *420*, 25–28. [[CrossRef](#)]
32. Wipf, H.; Kappesser, B.; Werner, R. Hydrogen diffusion in titanium and zirconium hydrides. *J. Alloys Compd.* **2000**, *310*, 190–195. [[CrossRef](#)]
33. Berti, N.; Cuevas, F.; Zhang, J.; Latroche, M. Enhanced reversibility of the electrochemical Li conversion reaction with MgH_2 - TiH_2 nanocomposites. *Int. J. Hydrog. Energy* **2017**. [[CrossRef](#)]
34. Berti, N. MgH_2 - TiH_2 Hydrides as Negatives Electrodes of Li-Ion Batteries. Ph.D. Thesis, Université Paris-Est, Paris, France, 2017.
35. Oumellal, Y.; Rougier, A.; Tarascon, J.-M.; Aymard, L. $2\text{LiH} + \text{M}$ ($\text{M} = \text{Mg}, \text{Ti}$): New concept of negative electrode for rechargeable lithium-ion batteries. *J. Power Sources* **2009**, *192*, 698–702. [[CrossRef](#)]
36. Oumellal, Y.; Zlotea, C.; Bastide, S.; Cachet-Vivier, C.; Leonel, E.; Sengmany, S.; Leroy, E.; Aymard, L.; Bonnet, J.P.; Latroche, M. Bottom-Up preparation of MgH_2 nanoparticles with enhanced cycle life stability during electrochemical conversion in Li-ion batteries. *Nanoscale* **2014**, *6*, 14459–14466. [[CrossRef](#)] [[PubMed](#)]
37. Huen, P.; Peru, F.; Charalambopoulou, G.; Steriotis, T.A.; Jensen, T.R.; Ravnsbæk, D.B. Nanoconfined NaAlH_4 conversion electrodes for Li batteries. *ACS Omega* **2017**, *2*, 1956–1967. [[CrossRef](#)]
38. Zhang, B.; Xia, G.; Sun, D.; Fang, F.; Yu, X. Magnesium hydride nanoparticles self-assembled on graphene as anode material for high-performance lithium-ion batteries. *ACS Nano* **2018**, *12*, 3816–3824. [[CrossRef](#)]
39. Silvestri, L.; Paolone, A.; Cirrincione, L.; Stallworth, P.; Greenbaum, S.; Panero, S.; Brutti, S.; Reale, P. NaAlH_4 nanoconfinement in a mesoporous carbon for application in lithium ion batteries. *J. Electrochem. Soc.* **2017**, *164*, A1120–A1125. [[CrossRef](#)]
40. Fichtner, M. Nanoconfinement effects in energy storage materials. *Phys. Chem. Chem. Phys.* **2011**, *13*, 21186–21195. [[CrossRef](#)]
41. Nielsen, T.K.; Besenbacher, F.; Jensen, T.R. Nanoconfined hydrides for energy storage. *Nanoscale* **2011**, *3*, 2086–2098. [[CrossRef](#)]
42. Winter, M.; Besenhard, J.O.; Spahr, M.E.; Novak, P. Insertion electrode materials for rechargeable lithium batteries. *Adv. Mater.* **1998**, *10*, 725–763. [[CrossRef](#)]
43. Kaskhedikar, N.A.; Maier, J. Lithium storage in carbon nanostructures. *Adv. Mater.* **2009**, *21*, 2664–2680. [[CrossRef](#)]
44. Hu, Y.S.; Adelhelm, P.; Smarsly, B.M.; Hore, S.; Antonietti, M.; Maier, J. Synthesis of hierarchically porous carbon monoliths with highly ordered microstructure and their application in rechargeable lithium batteries with high-rate capability. *Adv. Funct. Mater.* **2007**, *17*, 1873–1878. [[CrossRef](#)]
45. Mrgudich, J.N. Conductivity of silver iodide pellets for solid-electrolyte batteries. *J. Electrochem. Soc.* **1960**, *107*, 475–479. [[CrossRef](#)]
46. Tubandt, C.; Lorenz, E. Molekularzustand und elektrisches leitvermögen kristallisierter salze. *Z. Phys. Chem.* **1914**, *87*, 513–542. [[CrossRef](#)]

47. Bachman, J.C.; Muy, S.; Grimaud, A.; Chang, H.H.; Pour, N.; Lux, S.F.; Paschos, O.; Maglia, F.; Lupart, S.; Lamp, P.; et al. Inorganic solid-state electrolytes for lithium batteries: Mechanisms and properties governing ion conduction. *Chem. Rev.* **2016**, *116*, 140–162. [[CrossRef](#)]
48. Zhang, Z.; Shao, Y.; Lotsch, B.; Hu, Y.S.; Li, H.; Janek, J.; Nazar, L.F.; Nan, C.W.; Maier, J.; Armand, M.; et al. New horizons for inorganic solid state ion conductors. *Energy Environ. Sci.* **2018**, *11*. [[CrossRef](#)]
49. de Klerk, N.J.J.; Rosloń, I.; Wagemaker, M. Diffusion mechanism of Li argyrodite solid electrolytes for Li-ion batteries and prediction of optimized halogen doping: The effect of Li vacancies, halogens, and halogen disorder. *Chem. Mater.* **2016**, *28*, 7955–7963. [[CrossRef](#)]
50. Braga, M.H.; Ferreira, J.A.; Stockhausen, V.; Oliveira, J.E.; El-Azab, A. Novel Li₃ClO based glasses with superionic properties for lithium batteries. *J. Mater. Chem. A* **2014**, *2*, 5470–5480. [[CrossRef](#)]
51. Jalem, R.; Yamamoto, Y.; Shiiba, H.; Nakayama, M.; Munakata, H.; Kasuga, T.; Kanamura, K. Concerted migration mechanism in the Li ion dynamics of garnet-type Li₇La₃Zr₂O₁₂. *Chem. Mater.* **2013**, *25*, 425–430. [[CrossRef](#)]
52. Weber, D.A.; Senyshyn, A.; Weldert, K.S.; Wenzel, S.; Zhang, W.B.; Kaiser, R.; Berendts, S.; Janek, J.; Zeier, W.G. Structural insights and 3D diffusion pathways within the lithium superionic conductor Li₁₀GeP₂S₁₂. *Chem. Mater.* **2016**, *28*, 5905–5915. [[CrossRef](#)]
53. Kraft, M.A.; Culver, S.P.; Calderon, M.; Bocher, F.; Krauskopf, T.; Senyshyn, A.; Dietrich, C.; Zevalkink, A.; Janek, J.; Zeier, W.G. Influence of lattice polarizability on the ionic conductivity in the lithium superionic argyrodites Li₆PS₅X (X = Cl, Br, I). *J. Am. Chem. Soc.* **2017**, *139*, 10909–10918. [[CrossRef](#)] [[PubMed](#)]
54. Shi, S.; Lu, P.; Liu, Z.; Qi, Y.; Hector, L.G., Jr.; Li, H.; Harris, S.J. Direct calculation of Li-ion transport in the solid electrolyte interphase. *J. Am. Chem. Soc.* **2012**, *134*, 15476–15487. [[CrossRef](#)] [[PubMed](#)]
55. He, X.; Zhu, Y.; Mo, Y. Origin of fast ion diffusion in super-ionic conductors. *Nat. Commun.* **2017**, *8*, 15893. [[CrossRef](#)] [[PubMed](#)]
56. Schlesinger, H.I.; Brown, H.C. Metallo borohydrides. III. Lithium borohydride. *J. Am. Chem. Soc.* **1940**, *62*, 3429–3435. [[CrossRef](#)]
57. Zuttel, A.; Rentsch, S.; Fischer, P.; Wenger, P.; Sudan, P.; Mauron, P.; Emmenegger, C. Hydrogen storage properties of LiBH₄. *J. Alloys Compd.* **2003**, *356*, 515–520. [[CrossRef](#)]
58. Zuttel, A.; Borgschulte, A.; Orimo, S.I. Tetrahydroborates as new hydrogen storage materials. *Scr. Mater.* **2007**, *56*, 823–828. [[CrossRef](#)]
59. Matsuo, M.; Nakamori, Y.; Orimo, S.; Maekawa, H.; Takamura, H. Lithium superionic conduction in lithium borohydride accompanied by structural transition. *Appl. Phys. Lett.* **2007**, *91*, 42–45. [[CrossRef](#)]
60. Yao, Y.S.; Klug, D.D. High-Pressure phases of lithium borohydride LiBH₄: A first-principles study. *Phys. Rev. B* **2012**, *86*, 64107. [[CrossRef](#)]
61. Ikeshoji, T.; Tsuchida, E.; Morishita, T.; Ikeda, K.; Matsuo, M.; Kawazoe, Y.; Orimo, S. Fast-Ionic conductivity of Li⁺ in LiBH₄. *Phys. Rev. B* **2011**, *83*, 144301. [[CrossRef](#)]
62. Skripov, A.V.; Soloninin, A.V.; Filinchuk, Y.; Chernyshov, D. Nuclear magnetic resonance study of the rotational motion and the phase transition in LiBH₄. *J. Phys. Chem. C* **2008**, *112*, 18701–18705. [[CrossRef](#)]
63. Ley, M.B.; Boulineau, S.; Janot, R.L.; Filinchuk, Y.; Jensen, T.R. New Li ion conductors and solid state hydrogen storage materials: LiM(BH₄)₃Cl, M = La, Gd. *J. Phys. Chem. C* **2012**, *116*, 21267–21276. [[CrossRef](#)]
64. Trück, J.; Hadjixenophontos, E.; Joshi, Y.; Richter, G.; Stender, P.; Schmitz, G. Ionic conductivity of melt-frozen LiBH₄ films. *RSC Adv.* **2019**, *9*, 38855–38859. [[CrossRef](#)]
65. Takahashi, K.; Hattori, K.; Yamazaki, T.; Takada, K.; Matsuo, M.; Orimo, S.-I.; Maekawa, H.; Takamura, H. All-solid-state lithium battery with LiBH₄ solid electrolyte. *J. Power Sources* **2013**, *226*, 61–64. [[CrossRef](#)]
66. Takahashi, K.; Maekawa, H.; Takamura, H. Effects of intermediate layer on interfacial resistance for all-solid-state lithium batteries using lithium borohydride. *Solid State Ion.* **2014**, *262*, 179–182. [[CrossRef](#)]
67. Li, W.; Wu, G.; Araújo, C.M.; Scheicher, R.H.; Blomqvist, A.; Ahuja, R.; Xiong, Z.; Feng, Y.; Chen, P. Li⁺ ion conductivity and diffusion mechanism in α-Li₃N and β-Li₃N. *Energy Environ. Sci.* **2010**, *3*, 1524–1530. [[CrossRef](#)]
68. Li, W.; Wu, G.T.; Xiong, Z.T.; Feng, Y.P.; Chen, P. Li⁺ ionic conductivities and diffusion mechanisms in Li-based imides and lithium amide. *Phys. Chem. Chem. Phys.* **2012**, *14*, 1596–1606. [[CrossRef](#)]
69. Knutz, B.; Skaarup, S. Cycling of Li/Li₃N/TiS₂ solid-state cells. *Solid State Ion.* **1983**, *9–10*, 371–374. [[CrossRef](#)]
70. Paik, B.; Wolczyk, A. Lithium imide (Li₂NH) as a solid-state electrolyte for electrochemical energy storage applications. *J. Phys. Chem. C* **2019**, *123*, 1619–1625. [[CrossRef](#)]

71. Wolczyk, A.; Pinatel, E.R.; Chierotti, M.R.; Nervi, C.; Gobetto, R.; Baricco, M. Solid-State NMR and thermodynamic investigations on $\text{LiBH}_4\text{LiNH}_2$ system. *Int. J. Hydrog. Energy* **2016**, *41*, 14475–14483. [[CrossRef](#)]
72. Wolczyk, A.; Paik, B.; Sato, T.; Nervi, C.; Brighi, M.; Gharib Doust, S.P.; Chierotti, M.; Matsuo, M.; Li, G.; Gobetto, R.; et al. $\text{Li}_5(\text{BH}_4)_3\text{NH}$: Lithium-rich mixed anion complex hydride. *J. Phys. Chem. C* **2017**, *121*, 11069–11075. [[CrossRef](#)]
73. Boukamp, B.A.; Huggins, R.A. Ionic-Conductivity in lithium imide. *Phys. Lett. A* **1979**, *72*, 464–466. [[CrossRef](#)]
74. David, W.I.; Jones, M.O.; Gregory, D.H.; Jewell, C.M.; Johnson, S.R.; Walton, A.; Edwards, P.P. A mechanism for non-stoichiometry in the lithium amide/lithium imide hydrogen storage reaction. *J. Am. Chem. Soc.* **2007**, *129*, 1594–1601. [[CrossRef](#)] [[PubMed](#)]
75. Maekawa, H.; Matsuo, M.; Takamura, H.; Ando, M.; Noda, Y.; Karahashi, T.; Orimo, S. Halide-Stabilized LiBH_4 , a room-temperature lithium fast-ion conductor. *J. Am. Chem. Soc.* **2009**, *131*, 894–895. [[CrossRef](#)] [[PubMed](#)]
76. Matsuo, M.; Takamura, H.; Maekawa, H.; Li, H.W.; Orimo, S. Stabilization of lithium superionic conduction phase and enhancement of conductivity of LiBH_4 by LiCl addition. *Appl. Phys. Lett.* **2009**, *94*, 084103. [[CrossRef](#)]
77. Miyazaki, R.; Karahashi, T.; Kumatani, N.; Noda, Y.; Ando, M.; Takamura, H.; Matsuo, M.; Orimo, S.; Maekawa, H. Room temperature lithium fast-ion conduction and phase relationship of LiI stabilized LiBH_4 . *Solid State Ion.* **2011**, *192*, 143–147. [[CrossRef](#)]
78. Sveinbjörnsson, D.; Myrdal, J.S.G.; Blanchard, D.; Bentzen, J.J.; Hirata, T.; Mogensen, M.B.; Norby, P.; Orimo, S.-I.; Vegge, T. Effect of heat treatment on the lithium ion conduction of the $\text{LiBH}_4\text{-LiI}$ solid solution. *J. Phys. Chem. C* **2013**, *117*, 3249–3257. [[CrossRef](#)]
79. Rude, L.H.; Zavorotynska, O.; Arnbjerg, L.M.; Ravnsbæk, D.B.; Malmkjær, R.A.; Grove, H.; Hauback, B.C.; Baricco, M.; Filinchuk, Y.; Besenbacher, F.; et al. Bromide substitution in lithium borohydride, $\text{LiBH}_4\text{-LiBr}$. *Int. J. Hydrog. Energy* **2011**, *36*, 15664–15672. [[CrossRef](#)]
80. Gulino, V.; Brighi, M.; Dematteis, E.M.; Murgia, F.; Nervi, C.; Cerny, R.; Baricco, M. Phase Stability and fast ion conductivity in the hexagonal $\text{LiBH}_4\text{-LiBr-LiCl}$ solid solution. *Chem. Mater.* **2019**, *31*, 5133–5144. [[CrossRef](#)]
81. Myrdal, J.S.G.; Blanchard, D.; Sveinbjörnsson, D.; Vegge, T. Li-Ion conduction in the $\text{LiBH}_4\text{-LiI}$ system from density functional theory calculations and quasi-elastic neutron scattering. *J. Phys. Chem. C* **2013**, *117*, 9084–9091. [[CrossRef](#)]
82. Matsuo, M.; Sato, T.; Miura, Y.; Oguchi, H.; Zhou, Y.; Maekawa, H.; Takamura, H.; Orimo, S.-I. Synthesis and lithium fast-ion conductivity of a new complex hydride $\text{Li}_3(\text{NH}_2)_2\text{I}$ with double-layered structure. *Chem. Mater.* **2010**, *22*, 2702–2704. [[CrossRef](#)]
83. Gamba, N.S.; Larochette, P.A.; Gennari, F.C. $\text{Li}_4(\text{NH}_2)_3\text{Cl}$ amide-chloride: A new synthesis route, and hydrogen storage kinetic and thermodynamic properties. *RSC Adv.* **2016**, *6*, 15622–15629. [[CrossRef](#)]
84. Anderson, P.A.; Chater, P.A.; Hewett, D.R.; Slater, P.R. Hydrogen storage and ionic mobility in amide-halide systems. *Faraday Discuss.* **2011**, *151*, 271–284. [[CrossRef](#)] [[PubMed](#)]
85. Davies, R.A.; Anderson, P.A. Synthesis and characterization of two new amide chloride compounds: Potential H-2 storage materials. *Int. J. Hydrog. Energy* **2015**, *40*, 3001–3005. [[CrossRef](#)]
86. Matsuo, M.; Remhof, A.; Martelli, P.; Caputo, R.; Ernst, M.; Miura, Y.; Sato, T.; Oguchi, H.; Maekawa, H.; Takamura, H.; et al. Complex hydrides with $(\text{BH}_4)^{-}$ and $(\text{NH}_2)^{-}$ anions as new lithium fast-ion conductors. *J. Am. Chem. Soc.* **2009**, *131*, 16389–16391. [[CrossRef](#)]
87. Blomqvist, A.; Araujo, C.M.; Scheicher, R.H.; Srepusharawoot, P.; Li, W.; Chen, P.; Ahuja, R. Hydrogen as promoter and inhibitor of superionicity: A case study on Li-N-H systems. *Phys. Rev. B* **2010**, *82*. [[CrossRef](#)]
88. Hewett, D.R. Mixed Anion Amides for Hydrogen Storage. Ph.D. Thesis, University of Birmingham, Birmingham, UK, 2012.
89. Orimo, S.; Nakamori, Y.; Kitahara, G.; Miwa, K.; Ohba, N.; Towata, S.; Züttel, A. Dehydriding and rehydriding reactions of LiBH_4 . *J. Alloys Compd.* **2005**, *404–406*, 427–430. [[CrossRef](#)]
90. Lindemann, I.; Domenech Ferrer, R.; Dunsch, L.; Filinchuk, Y.; Cerny, R.; Hagemann, H.; D’Anna, V.; Lawson Daku, L.M.; Schultz, L.; Gutfleisch, O. $\text{Al}_3\text{Li}_4(\text{BH}_4)_{13}$: A complex double-cation borohydride with a new structure. *Chemistry* **2010**, *16*, 8707–8712. [[CrossRef](#)]

91. Noritake, T.; Aoki, M.; Towata, S.; Ninomiya, A.; Nakamori, Y.; Orimo, S. Crystal structure analysis of novel complex hydrides formed by the combination of LiBH_4 and LiNH_2 . *Appl. Phys. A Mater. Sci. Process.* **2006**, *83*, 277–279. [[CrossRef](#)]
92. Aoki, M.; Miwa, K.; Noritake, T.; Kitahara, G.; Nakamori, Y.; Orimo, S.; Towata, S. Destabilization of LiBH_4 by mixing with LiNH_2 . *Appl. Phys. A Mater. Sci. Process.* **2005**, *80*, 1409–1412. [[CrossRef](#)]
93. Deiseroth, H.J.; Kong, S.T.; Eckert, H.; Vannahme, J.; Reiner, C.; Zaiss, T.; Schlosser, M. $\text{Li}_6\text{PS}_5\text{X}$: A class of crystalline Li-rich solids with an unusually high Li^+ mobility. *Angew. Chem. Int. Ed. Engl.* **2008**, *47*, 755–758. [[CrossRef](#)]
94. Paskevicius, M.; Hansen, B.R.S.; Jorgensen, M.; Richter, B.; Jensen, T.R. Multifunctionality of silver closo-boranes. *Nat. Commun.* **2017**, *8*, 15136. [[CrossRef](#)] [[PubMed](#)]
95. Epp, V.; Gun, O.; Deiseroth, H.J.; Wilkening, M. Highly mobile ions: Low-Temperature NMR directly probes extremely fast Li^+ hopping in argyrodite-type $\text{Li}_6\text{PS}_5\text{Br}$. *J. Phys. Chem. Lett.* **2013**, *4*, 2118–2123. [[CrossRef](#)]
96. Chen, M.; Rao, R.P.; Adams, S. High capacity all-solid-state $\text{Cu-Li}_2\text{S/Li}_6\text{PS}_5\text{Br/In}$ batteries. *Solid State Ion.* **2014**, *262*, 183–187. [[CrossRef](#)]
97. Rao, R.P.; Adams, S. Studies of lithium argyrodite solid electrolytes for all-solid-state batteries. *Phys. Status Solidi A Appl. Mater. Sci.* **2011**, *208*, 1804–1807. [[CrossRef](#)]
98. Dao, A.H.; Lopez-Aranguren, P.; Cerny, R.; Guiader, O.; Zhan, J.X.; Cuevas, F.; Latroche, M.; Jordy, C. Improvement of the ionic conductivity on new substituted borohydride argyrodites. *Solid State Ion.* **2019**, *339*, 114987. [[CrossRef](#)]
99. Jordy, C.; López-Aranguren, P.; Dao, A.H.; Latroche, M.; Zhang, J.; Cuevas, F. Solid electrolyte for a lithium-ion electrochemical element. Patent WO/2019/057840, 28 March 2019.
100. Sakuda, A.; Yamauchi, A.; Yubuchi, S.; Kitamura, N.; Idemoto, Y.; Hayashi, A.; Tatsumisago, M. Mechanochemically prepared $\text{Li}_2\text{S-P}_2\text{S}_5\text{-LiBH}_4$ solid electrolytes with an argyrodite structure. *ACS Omega* **2018**, *3*, 5453–5458. [[CrossRef](#)]
101. Sakuda, A.; Hayashi, A.; Tatsumisago, M. Recent progress on interface formation in all-solid-state batteries. *Curr. Opin. Electrochem.* **2017**, *6*, 108–114. [[CrossRef](#)]
102. Sakuda, A.; Takeuchi, T.; Kobayashi, H. Electrode morphology in all-solid-state lithium secondary batteries consisting of $\text{LiNi}_{1/3}\text{Co}_{1/3}\text{Mn}_{1/3}\text{O}_2$ and $\text{Li}_2\text{S-P}_2\text{S}_5$ solid electrolytes. *Solid State Ion.* **2016**, *285*, 112–117. [[CrossRef](#)]
103. Latroche, M.; Blanchard, D.; Cuevas, F.; El Kharbachi, A.; Hauback, B.C.; Jensen, T.R.; de Jongh, P.E.; Kim, S.; Nazer, N.S.; Ngene, P.; et al. Full-Cell hydride-based solid-state Li batteries for energy storage. *Int. J. Hydrog. Energy* **2019**, *44*, 7875–7887. [[CrossRef](#)]
104. Zeng, L.; Ichikawa, T.; Kawahito, K.; Miyaoka, H.; Kojima, Y. Bulk-Type all-solid-state lithium-ion batteries: remarkable performances of a carbon nanofiber-supported MgH_2 composite electrode. *ACS Appl. Mater. Interfaces* **2017**, *9*, 2261–2266. [[CrossRef](#)]
105. Zeng, L.; Kawahito, K.; Ikeda, S.; Ichikawa, T.; Miyaoka, H.; Kojima, Y. Metal hydride-based materials towards high performance negative electrodes for all-solid-state lithium-ion batteries. *Chem. Commun. (Camb)* **2015**, *51*, 9773–9776. [[CrossRef](#)] [[PubMed](#)]
106. Ikeda, S.; Ichikawa, T.; Goshome, K.; Yamaguchi, S.; Miyaoka, H.; Kojima, Y. Anode properties of Al_2O_3 -added MgH_2 for all-solid-state lithium-ion batteries. *J. Solid State Electrochem.* **2015**, *19*, 3639–3644. [[CrossRef](#)]
107. Ikeda, S.; Ichikawa, T.; Kawahito, K.; Hirabayashi, K.; Miyaoka, H.; Kojima, Y. Anode properties of magnesium hydride catalyzed with niobium oxide for an all solid-state lithium-ion battery. *Chem. Commun. (Camb.)* **2013**, *49*, 7174–7176. [[CrossRef](#)] [[PubMed](#)]
108. Kawahito, K.; Zeng, L.; Ichikawa, T.; Miyaoka, H.; Kojima, Y. Electrochemical performance of titanium hydride for bulk-type all-solid-state lithium-ion batteries. *Mater. Trans.* **2016**, *57*, 755–757. [[CrossRef](#)]
109. El Kharbachi, A.; Uesato, H.; Kawai, H.; Wenner, S.; Miyaoka, H.; Sørby, M.H.; Fjellvåg, H.; Ichikawa, T.; Hauback, B.C. $\text{MgH}_2\text{-CoO}$: A conversion-type composite electrode for LiBH_4 -based all-solid-state lithium ion batteries. *RSC Adv.* **2018**, *8*, 23468–23474. [[CrossRef](#)]
110. Liu, J.; Xu, J.Y.; Lin, Y.; Li, J.; Lai, Y.Q.; Yuan, C.F.; Zhang, J.; Zhu, K. All-solid-state lithium ion battery: Research and industrial prospects. *Acta Chim. Sin.* **2013**, *71*, 869–878. [[CrossRef](#)]
111. Mo, F.J.; Chi, X.W.; Yang, S.P.; Wu, F.L.; Song, Y.; Sun, D.L.; Yao, Y.; Fang, F. Stable three-dimensional metal hydride anodes for solid-state lithium storage. *Energy Storage Mater.* **2019**, *18*, 423–428. [[CrossRef](#)]

112. Zaïdi, W.; Bonnet, J.P.; Zhang, J.; Cuevas, F.; Latroche, M.; Couillaud, S.; Bobet, J.L.; Sougrati, M.T.; Jumas, J.C.; Aymard, L. Reactivity of complex hydrides Mg_2FeH_6 , Mg_2CoH_5 and Mg_2NiH_4 with lithium ion: Far from equilibrium electrochemically driven conversion reactions. *Int. J. Hydrog. Energy* **2013**, *38*, 4798–4808. [CrossRef]
113. Huen, P.; Ravnsbæk, D.B. All-solid-state lithium batteries—The Mg_2FeH_6 -electrode $LiBH_4$ -electrolyte system. *Electrochem. Commun.* **2018**, *87*, 81–85. [CrossRef]
114. Dao, A.H.; Berti, N.; López-Aranguren, P.; Zhang, J.; Cuevas, F.; Jordy, C.; Latroche, M. Electrochemical properties of MgH_2 - TiH_2 nanocomposite as active materials for all-solid-state lithium batteries. *J. Power Sources* **2018**, *397*, 143–149. [CrossRef]
115. López-Aranguren, P.; Berti, N.; Dao, A.H.; Zhang, J.; Cuevas, F.; Latroche, M.; Jordy, C. An all-solid-state metal hydride—Sulfur lithium-ion battery. *J. Power Sources* **2017**, *357*, 56–60. [CrossRef]
116. Unemoto, A.; Yasaku, S.; Nogami, G.; Tazawa, M.; Taniguchi, M.; Matsuo, M.; Ikeshoji, T.; Orimo, S. Development of bulk-type all-solid-state lithium-sulfur battery using $LiBH_4$ electrolyte. *Appl. Phys. Lett.* **2014**, *105*, 083901. [CrossRef]
117. Lin, Z.; Liang, C. Lithium-Sulfur batteries: From liquid to solid cells. *J. Mater. Chem. A* **2015**, *3*, 936–958. [CrossRef]
118. Tarascon, J.M. Is lithium the new gold? *Nat. Chem.* **2010**, *2*, 510. [CrossRef] [PubMed]
119. Amnesty International. Available online: <https://www.amnesty.org/en/latest/news/2019/03/amnesty-challenges-industry-leaders-to-clean-up-their-batteries/> (accessed on 21 February 2020).
120. Caputo, R.; Garroni, S.; Olid, D.; Teixidor, F.; Surinach, S.; Baro, M.D. Can $Na_2[B_{12}H_{12}]$ be a decomposition product of $NaBH_4$? *Phys. Chem. Chem. Phys.* **2010**, *12*, 15093–15100. [CrossRef]
121. Wiersema, R.J.; Hawthorne, M.F. Electrochemistry and Boron-11 nuclear magnetic-resonance spectra of monocarbon carboranes. *Inorg. Chem.* **1973**, *12*, 785–788. [CrossRef]
122. Keen, D.A. Disordering phenomena in superionic conductors. *J. Phys. Condens. Matter* **2002**, *14*, R819–R857. [CrossRef]
123. Udovic, T.J.; Matsuo, M.; Unemoto, A.; Verdál, N.; Stavila, V.; Skripov, A.V.; Rush, J.J.; Takamura, H.; Orimo, S. Sodium superionic conduction in $Na_2B_{12}H_{12}$. *Chem Commun. (Camb.)* **2014**, *50*, 3750–3752. [CrossRef]
124. Verdál, N.; Her, J.H.; Stavila, V.; Soloninin, A.V.; Babanova, O.A.; Skripov, A.V.; Udovic, T.J.; Rush, J.J. Complex high-temperature phase transitions in $Li_2B_{12}H_{12}$ and $Na_2B_{12}H_{12}$. *J. Solid State Chem.* **2014**, *212*, 81–91. [CrossRef]
125. Sadikin, Y.; Schouwink, P.; Brighi, M.; Lodziana, Z.; Cerny, R. Modified anion packing of $Na_2B_{12}H_{12}$ in close to room temperature superionic conductors. *Inorg Chem.* **2017**, *56*, 5006–5016. [CrossRef]
126. Skripov, A.V.; Babanova, O.A.; Soloninin, A.V.; Stavila, V.; Verdál, N.; Udovic, T.J.; Rush, J.J. Nuclear magnetic resonance study of atomic motion in $A_2B_{12}H_{12}$ (A = Na, K, Rb, Cs): Anion reorientations and Na^+ mobility. *J. Phys. Chem. C* **2013**, *117*, 25961–25968. [CrossRef]
127. Verdál, N.; Udovic, T.J.; Stavila, V.; Tang, W.S.; Rush, J.J.; Skripov, A.V. Anion reorientations in the superionic conducting phase of $Na_2B_{12}H_{12}$. *J. Phys. Chem. C* **2014**, *118*, 17483–17489. [CrossRef]
128. Wang, Y.; Richards, W.D.; Ong, S.P.; Miara, L.J.; Kim, J.C.; Mo, Y.; Ceder, G. Design principles for solid-state lithium superionic conductors. *Nat. Mater.* **2015**, *14*, 1026–1031. [CrossRef] [PubMed]
129. Tang, W.S.; Unemoto, A.; Zhou, W.; Stavila, V.; Matsuo, M.; Wu, H.; Orimo, S.I.; Udovic, T.J. Unparalleled lithium and sodium superionic conduction in solid electrolytes with large monovalent cage-like anions. *Energy Environ. Sci.* **2015**, *8*, 3637–3645. [CrossRef]
130. Brighi, M.; Murgia, F.; Lodziana, Z.; Schouwink, P.; Wolczyk, A.; Cerny, R. A mixed anion hydroborate/carba-hydroborate as a room temperature Na-ion solid electrolyte. *J. Power Sources* **2018**, *404*, 7–12. [CrossRef]
131. Pauling, L. The principles determining the structure of complex ionic crystals. *J. Am. Chem. Soc.* **1929**, *51*, 1010–1026. [CrossRef]
132. Tang, W.S.; Matsuo, M.; Wu, H.; Stavila, V.; Zhou, W.; Talin, A.A.; Soloninin, A.V.; Skoryunov, R.V.; Babanova, O.A.; Skripov, A.V.; et al. Liquid-Like ionic conduction in solid lithium and sodium monocarba-closo-decaborates near or at room temperature. *Adv. Energy Mater.* **2016**, *6*, 1502237. [CrossRef]
133. Duchêne, L.; Kühnel, R.S.; Stilp, E.; Cuervo Reyes, E.; Remhof, A.; Hagemann, H.; Battaglia, C. A 3 V all-solid-state sodium-ion battery based on a closo-borate electrolyte. *Energy Environ. Sci.* **2017**, *10*, 2609–2615. [CrossRef]

134. Sharafi, A.; Meyer, H.M.; Nanda, J.; Wolfenstine, J.; Sakamoto, J. Characterizing the Li-Li₇La₃Zr₂O₁₂ interface stability and kinetics as a function of temperature and current density. *J. Power Sources* **2016**, *302*, 135–139. [[CrossRef](#)]
135. Cheng, E.J.; Sharafi, A.; Sakamoto, J. Intergranular Li metal propagation through polycrystalline Li_{6.25}Al_{0.25}La₃Zr₂O₁₂ ceramic electrolyte. *Electrochim. Acta* **2017**, *223*, 85–91. [[CrossRef](#)]
136. Taylor, N.J.; Stangeland-Molo, S.; Haslam, C.G.; Sharafi, A.; Thompson, T.; Wang, M.; Garcia-Mendez, R.; Sakamoto, J. Demonstration of high current densities and extended cycling in the garnet Li₇La₃Zr₂O₁₂ solid electrolyte. *J. Power Sources* **2018**, *396*, 314–318. [[CrossRef](#)]
137. Pasquini, L. The effects of nanostructure on the hydrogen sorption properties of magnesium-based metallic compounds: A review. *Crystals* **2018**, *8*, 106. [[CrossRef](#)]
138. Selvam, P.; Viswanathan, B.; Swamy, C.S.; Srinivasan, V. Magnesium and magnesium alloy hydrides. *Int. J. Hydrog. Energy* **1986**, *11*, 169–192. [[CrossRef](#)]
139. Crivello, J.C.; Dam, B.; Denys, R.V.; Dornheim, M.; Grant, D.M.; Huot, J.; Jensen, T.R.; de Jongh, P.; Latroche, M.; Milanese, C.; et al. Review of magnesium hydride-based materials: Development and optimisation. *Appl. Phys. A Mater. Sci. Process.* **2016**, *122*, 5077. [[CrossRef](#)]
140. Webb, C.J. A review of catalyst-enhanced magnesium hydride as a hydrogen storage material. *J. Phys. Chem. Solids* **2015**, *84*, 96–106. [[CrossRef](#)]
141. Cesario Asselli, A.A.; Bourbeau Hébert, N.; Huot, J. The role of morphology and severe plastic deformation on the hydrogen storage properties of magnesium. *Int. J. Hydrog. Energy* **2014**, *39*, 12778–12783. [[CrossRef](#)]
142. Chu, H.; Qiu, S.; Sun, L.; Huot, J. Enhancement of the initial hydrogenation of Mg by ball milling with alkali metal amides MNH₂ (M = Li or Na). *Dalton Trans.* **2015**, *44*, 16694–16697. [[CrossRef](#)]
143. Eijit, S.W.H.; Leegwater, H.; Schut, H.; Anastasopol, A.; Egger, W.; Ravelli, L.; Hugenschmidt, C.; Dam, B. Layer-resolved study of the Mg to MgH₂ transformation in Mg-Ti films with short-range chemical order. *J. Alloys Compd.* **2011**, *509*, S567–S571. [[CrossRef](#)]
144. AlMatrouk, H.S.; Chihai, V. Theoretical study on the effects of the magnesium hydride doping with cobalt and nickel on the hydrogen release. *Int. J. Hydrog. Energy* **2015**, *40*, 5319–5325. [[CrossRef](#)]
145. Barcelo, S.; Rogers, M.; Grigoropoulos, C.P.; Mao, S.S. Hydrogen storage property of sandwiched magnesium hydride nanoparticle thin film. *Int. J. Hydrog. Energy* **2010**, *35*, 7232–7235. [[CrossRef](#)]
146. Okamoto, H. Mg-Pd (Magnesium-Palladium). *J. Phase Equilibria Diffus.* **2010**, *31*, 407–408. [[CrossRef](#)]
147. Nobuhara, K.; Kasai, H.; Diño, W.A.; Nakanishi, H. H₂ dissociative adsorption on Mg, Ti, Ni, Pd and La surfaces. *Surf. Sci.* **2004**, *566–568*, 703–707. [[CrossRef](#)]
148. Krozer, A.; Kasemo, B. Unusual kinetics due to interface hydride formation in the hydriding of Pd/Mg sandwich layers. *J. Vac. Sci. Technol. A Vac. Surf. Film* **1987**, *5*, 1003–1005. [[CrossRef](#)]
149. Higuchi, K.; Kajioaka, H.; Toiyama, K.; Fujii, H.; Orimo, S.; Kikuchi, Y. In situ study of hydriding-dehydriding properties in some Pd/Mg thin films with different degree of Mg crystallization. *J. Alloys Compd.* **1999**, *293–295*, 484–489. [[CrossRef](#)]
150. Kim, K.-B.; Shim, J.-H.; Park, S.-H.; Choi, I.-S.; Oh, K.H.; Cho, Y.W. Dehydrogenation reaction pathway of the LiBH₄-MgH₂ composite under various pressure conditions. *J. Phys. Chem. C* **2015**, *119*, 9714–9720. [[CrossRef](#)]
151. Vajo, J.J.; Mertens, F.; Ahn, C.C.; Bowman, R.C.; Fultz, B. Altering hydrogen storage properties by hydride destabilization through alloy formation: LiH and MgH₂ destabilized with Si. *J. Phys. Chem. B* **2004**, *108*, 13977–13983. [[CrossRef](#)]
152. Stampfer, J.F., Jr.; Holley, C.E., Jr.; Suttle, J.F. The magnesium-hydrogen system. *J. Am. Chem. Soc.* **1960**, *82*, 3504–3508. [[CrossRef](#)]
153. Bogdanovic, B. Thermodynamic investigation of the magnesium-hydrogen system. *J. Alloys Compd.* **1999**, *282*, 84–92. [[CrossRef](#)]
154. Takeichi, N.; Sakaida, Y.; Kiyobayashi, T.; Takeshita, H.T. Hydrogen absorption and desorption behavior of magnesium hydride: Incubation period and reaction mechanism. *Mater. Trans.* **2014**, *55*, 1161–1167. [[CrossRef](#)]
155. Mooij, L.; Dam, B. Hysteresis and the role of nucleation and growth in the hydrogenation of Mg nanolayers. *Phys. Chem. Chem. Phys.* **2013**, *15*, 2782–2792. [[CrossRef](#)]
156. Mooij, L.; Dam, B. Nucleation and growth mechanisms of nano magnesium hydride from the hydrogen sorption kinetics. *Phys. Chem. Chem. Phys.* **2013**, *15*, 11501–11510. [[CrossRef](#)] [[PubMed](#)]

157. Ingason, A.S.; Olafsson, S. Thermodynamics of hydrogen uptake in Mg films studied by resistance measurements. *J. Alloys Compd.* **2005**, *404*, 469–472. [[CrossRef](#)]
158. Gharavi, A.G.; Akyildiz, H.; Ozturk, T. Thickness effects in hydrogen sorption of Mg/Pd thin films. *J. Alloys Compd.* **2013**, *580*, S175–S178. [[CrossRef](#)]
159. Hadjixenophontos, E.; Zhang, K.; Weigel, A.; Stender, P.; Schmitz, G. Hydrogenation of Pd/Mg films: A quantitative assessment of transport coefficients. *Int. J. Hydrog. Energy* **2019**, *44*, 27862–27875. [[CrossRef](#)]
160. Yao, X.; Zhu, Z.H.; Cheng, H.M.; Lu, G.Q. Hydrogen diffusion and effect of grain size on hydrogenation kinetics in magnesium hydrides. *J. Mater. Res.* **2008**, *23*, 336–340. [[CrossRef](#)]
161. Fernandez, J.F.; Sanchez, C.R. Rate determining step in the absorption and desorption of hydrogen by magnesium. *J. Alloys Compd.* **2002**, *340*, 189–198. [[CrossRef](#)]
162. Han, J.S.; Pezat, M.; Lee, J.Y. Thermal-Desorption of hydrogen from magnesium hydride. *Scr. Metall.* **1986**, *20*, 951–956. [[CrossRef](#)]
163. Hadjixenophontos, E.; Roussel, M.; Sato, T.; Weigel, A.; Stender, P.; Orimo, S.I.; Schmitz, G. Imaging the hydrogenation of Mg thin films. *Int. J. Hydrog. Energy* **2017**, *42*, 22411–22416. [[CrossRef](#)]
164. Hadjixenophontos, E.; Michalek, L.; Weigel, A.; Schmitz, G. Hydrogen sorption kinetics in MgH₂ and TiH₂ thin films. *Defect Diffus. Forum* **2018**, *383*, 127–132. [[CrossRef](#)]
165. Kumar, S.; Reddy, G.L.N.; Raju, V.S. Hydrogen storage in Pd capped thermally grown Mg films: Studies by nuclear resonance reaction analysis. *J. Alloys Compd.* **2009**, *476*, 500–506. [[CrossRef](#)]
166. Reddy, G.L.N.; Kumar, S.; Sunitha, Y.; Kalavathi, S.; Raju, V.S. Intermixing and formation of Pd-Mg intermetallics in Pd/Mg/Si films. *J. Alloys Compd.* **2009**, *481*, 714–718. [[CrossRef](#)]
167. Zheng, S.; Wang, K.; Oleshko, V.P.; Bendersky, L.A. Mg-Fe thin films: A phase-separated structure with fast kinetics of hydrogenation. *J. Phys. Chem. C* **2012**, *116*, 21277–21284. [[CrossRef](#)]
168. Fry, C.M.P.; Grant, D.M.; Walker, G.S. Catalysis and evolution on cycling of nano-structured magnesium multilayer thin films. *Int. J. Hydrog. Energy* **2014**, *39*, 1173–1184. [[CrossRef](#)]
169. Liu, Y.; Cao, Y.; Huang, L.; Gao, M.; Pan, H. Rare earth-Mg-Ni-based hydrogen storage alloys as negative electrode materials for Ni/MH batteries. *J. Alloys Compd.* **2011**, *509*, 675–686. [[CrossRef](#)]
170. Jung, H.; Cho, S.; Lee, W. A catalytic effect on hydrogen absorption kinetics in Pd/Ti/Mg/Ti multilayer thin films. *J. Alloys Compd.* **2015**, *635*, 203–206. [[CrossRef](#)]
171. Vermeulen, P.; Niessen, R.A.H.; Notten, P.H.L. Hydrogen storage in metastable Mg₂Ti(1-y) thin films. *Electrochem. Commun.* **2006**, *8*, 27–32. [[CrossRef](#)]
172. Zhang, Y.; Zhuang, X.; Zhu, Y.; Wan, N.; Li, L.; Dong, J. Synergistic effects of TiH₂ and Pd on hydrogen desorption performances of MgH₂. *Int. J. Hydrog. Energy* **2015**, *40*, 16338–16346. [[CrossRef](#)]
173. Bazzanella, N.; Checchetto, R.; Miotello, A. Atoms and nanoparticles of transition metals as catalysts for hydrogen desorption from magnesium hydride. *J. Nanomater.* **2011**, *2011*, 1–11. [[CrossRef](#)]
174. Peng, D.; Ding, Z.; Zhang, L.; Fu, Y.; Wang, J.; Li, Y.; Han, S. Remarkable hydrogen storage properties and mechanisms of the shell-core MgH₂@carbon aerogel microspheres. *Int. J. Hydrog. Energy* **2018**, *43*, 3731–3740. [[CrossRef](#)]
175. Ding, Z.M.; Fu, Y.K.; Wang, Y.; Bi, J.; Zhang, L.; Peng, D.D.; Li, Y.; Han, S.M. MgCNi₃ prepared by powder metallurgy for improved hydrogen storage properties of MgH₂. *Int. J. Hydrog. Energy* **2019**, *44*, 8347–8356. [[CrossRef](#)]
176. Pavlyuk, V.; Dmytriv, G.; Chumak, I.; Gutfleisch, O.; Lindemann, I.; Ehrenberg, H. High hydrogen content super-lightweight intermetallics from the Li-Mg-Si system. *Int. J. Hydrog. Energy* **2013**, *38*, 5724–5737. [[CrossRef](#)]
177. Garroni, S.; Santoru, A.; Cao, H.J.; Dornheim, M.; Klassen, T.; Milanese, C.; Gennari, F.; Pistidda, C. Recent progress and new perspectives on metal amide and imide systems for solid-state hydrogen storage. *Energies* **2018**, *11*, 1027. [[CrossRef](#)]
178. Cao, H.J.; Zhang, Y.; Wang, J.H.; Xiong, Z.T.; Wu, G.T.; Chen, P. Materials design and modification on amide-based composites for hydrogen storage. *Prog. Nat. Sci. Mater. Int.* **2012**, *22*, 550–560. [[CrossRef](#)]
179. Gomez, Y.A.; Oyarce, A.; Lindbergh, G.; Lagergren, C. Ammonia contamination of a proton exchange membrane fuel cell. *J. Electrochem. Soc.* **2018**, *165*, F189–F197. [[CrossRef](#)]
180. Rude, L.H.; Nielsen, T.K.; Ravnsbaek, D.B.; Bosenberg, U.; Ley, M.B.; Richter, B.; Arnbjerg, L.M.; Dornheim, M.; Filinchuk, Y.; Besenbacher, F.; et al. Tailoring properties of borohydrides for hydrogen storage: A review. *Phys. Status Solidi A Appl. Mater. Sci.* **2011**, *208*, 1754–1773. [[CrossRef](#)]

181. Chen, P.; Xiong, Z.; Luo, J.; Lin, J.; Tan, K.L. Interaction of hydrogen with metal nitrides and imides. *Nature* **2002**, *420*, 302–304. [[CrossRef](#)]
182. Hu, Y.H.; Ruckenstein, E. H₂ storage in Li₃N temperature-programmed hydrogenation and dehydrogenation. *Ind. Eng. Chem. Res.* **2003**, *42*, 5135–5139. [[CrossRef](#)]
183. Leng, H.Y.; Ichikawa, T.; Hino, S.; Hanada, N.; Isobe, S.; Fujii, H. New metal-N-H system composed of Mg(NH₂)₂ and LiH for hydrogen storage. *J. Phys. Chem. B* **2004**, *108*, 8763–8765. [[CrossRef](#)]
184. Luo, W. (LiNH₂-MgH₂): A viable hydrogen storage system. *J. Alloys Compd.* **2004**, *381*, 284–287. [[CrossRef](#)]
185. Nakamori, Y.; Kitahara, G.; Miwa, K.; Towata, S.; Orimo, S. Reversible hydrogen-storage functions for mixtures of Li₃N and Mg₃N₂. *Appl. Phys. A* **2005**, *80*, 1–3. [[CrossRef](#)]
186. Nakamori, Y.; Orimo, S. Destabilization of Li-based complex hydrides. *J. Alloys Compd.* **2004**, *370*, 271–275. [[CrossRef](#)]
187. Xiong, Z.T.; Wu, G.T.; Hu, H.J.; Chen, P. Ternary imides for hydrogen storage. *Adv. Mater.* **2004**, *16*, 1522. [[CrossRef](#)]
188. Xiong, Z.; Hu, J.; Wu, G.; Chen, P.; Luo, W.; Gross, K.; Wang, J. Thermodynamic and kinetic investigations of the hydrogen storage in the Li-Mg-N-H system. *J. Alloys Compd.* **2005**, *398*, 235–239. [[CrossRef](#)]
189. Ichikawa, T. Amides, Imides and Mixtures. In *Handbook of Hydrogen Storage: New Materials for Future Energy Storage*; Hirscher, M., Ed.; Wiley-VCH: Weinheim, Germany, 2010; Chapter 6; pp. 159–185. [[CrossRef](#)]
190. Paskevicius, M.; Jepsen, L.H.; Schouwink, P.; Cerny, R.; Ravnsbaek, D.B.; Filinchuk, Y.; Dornheim, M.; Besenbacher, F.; Jensen, T.R. Metal borohydrides and derivatives—Synthesis, structure and properties. *Chem. Soc. Rev.* **2017**, *46*, 1565–1634. [[CrossRef](#)] [[PubMed](#)]
191. Dematteis, E.M.; Vaunois, S.; Pistidda, C.; Dornheim, M.; Baricco, M. Reactive hydride composite of Mg₂NiH₄ with borohydrides eutectic mixtures. *Crystals* **2018**, *8*, 90. [[CrossRef](#)]
192. Callini, E.; Atakli, Z.O.K.; Hauback, B.C.; Orimo, S.; Jensen, C.; Dornheim, M.; Grant, D.; Cho, Y.W.; Chen, P.; Hjørvarsson, B.; et al. Complex and liquid hydrides for energy storage. *Appl. Phys. A Mater. Sci. Process.* **2016**, *122*, 353. [[CrossRef](#)]
193. Soulie, J.P.; Renaudin, G.; Cerny, R.; Yvon, K. Lithium Boro-hydride LiBH₄. Part 1. Crystal structure. *ChemInform* **2003**, *34*. [[CrossRef](#)]
194. Møller, K.; Sheppard, D.; Ravnsbæk, D.; Buckley, C.; Akiba, E.; Li, H.-W.; Jensen, T. Complex metal hydrides for hydrogen, thermal and electrochemical energy storage. *Energies* **2017**, *10*, 1645. [[CrossRef](#)]
195. Yang, J.B.; Zhou, X.D.; Cai, Q.; James, W.J.; Yelon, W.B. Crystal and electronic structures of LiNH₂. *Appl. Phys. Lett.* **2006**, *88*, 041914. [[CrossRef](#)]
196. Chater, P.A.; David, W.I.; Anderson, P.A. Synthesis and structure of the new complex hydride Li₂BH₄NH₂. *Chem. Commun. (Camb)* **2007**, 4770–4772. [[CrossRef](#)]
197. Wu, H.; Zhou, W.; Udovic, T.J.; Rush, J.J.; Yildirim, T. Structures and crystal chemistry of Li₂BNH₆ and Li₄BN₃H₁₀. *Chem. Mat.* **2008**, *20*, 1245–1247. [[CrossRef](#)]
198. Herbst, J.F.; Hector, L.G. Electronic structure and energetics of the quaternary hydride Li₄BN₃H₁₀. *Appl. Phys. Lett.* **2006**, *88*, 231904. [[CrossRef](#)]
199. Siegel, D.J.; Wolverton, C.; Ozolins, V. Reaction energetics and crystal structure of Li₄BN₃H₁₀ from first principles. *Phys. Rev. B* **2007**, *75*. [[CrossRef](#)]
200. Lim, K.L.; Kazemian, H.; Yaakob, Z.; Daud, W.R.W. Solid-State materials and methods for hydrogen storage: A critical review. *Chem. Eng. Technol.* **2010**, *33*, 213–226. [[CrossRef](#)]
201. SGTE Substance Database V 4.1. Available online: http://www.crct.polymtl.ca/fact/documentation/sgps_list.htm (accessed on 21 February 2020).
202. El Kharbachi, A.; Pinatel, E.; Nuta, I.; Baricco, M. A thermodynamic assessment of LiBH₄. *Calphad* **2012**, *39*, 80–90. [[CrossRef](#)]
203. Borgschulte, A.; Jones, M.O.; Callini, E.; Probst, B.; Kato, S.; Zuttel, A.; David, W.I.F.; Orimo, S. Surface and bulk reactions in borohydrides and amides. *Energy Environ. Sci.* **2012**, *5*, 6823–6832. [[CrossRef](#)]
204. Singer, J.P.; Meyer, M.S.; Speer, R.M.; Fischer, J.E.; Pinkerton, F.E. Determination of the phase behavior of (LiNH₂)_c(LiBH₄)_{1-c} quaternary hydrides through in situ x-ray diffraction. *J. Phys. Chem. C* **2009**, *113*, 18927–18934. [[CrossRef](#)]
205. Pinkerton, F.E.; Meisner, G.P.; Meyer, M.S.; Balogh, M.P.; Kundrat, M.D. Hydrogen desorption exceeding ten weight percent from the new quaternary hydride Li₃BN₂H₈. *J. Phys. Chem B* **2005**, *109*, 6–8. [[CrossRef](#)]

206. Chen, P.; Xiong, Z.T.; Luo, J.Z.; Lin, J.Y.; Tan, K.L. Interaction between lithium amide and lithium hydride. *J. Phys. Chem. B* **2003**, *107*, 10967–10970. [[CrossRef](#)]
207. Shaw, L.L.; Osborn, W.; Markmaitree, T.; Wan, X. The reaction pathway and rate-limiting step of dehydrogenation of the LiHN₂ + LiH mixture. *J. Power Sources* **2008**, *177*, 500–505. [[CrossRef](#)]
208. Miceli, G.; Cucinotta, C.S.; Bernasconi, M.; Parrinello, M. First principles study of the LiNH₂/Li₂NH transformation. *J. Phys. Chem. C* **2010**, *114*, 15174–15183. [[CrossRef](#)]
209. Hu, J.; Liu, Y.; Wu, G.; Xiong, Z.; Chua, Y.S.; Chen, P. Improvement of hydrogen storage properties of the Li-Mg-N-H system by addition of LiBH₄. *Chem. Mater.* **2008**, *20*, 4398–4402. [[CrossRef](#)]
210. Wang, J.; Liu, T.; Wu, G.; Li, W.; Liu, Y.; Araújo, C.M.; Scheicher, R.H.; Blomqvist, A.; Ahuja, R.; Xiong, Z. Potassium-Modified Mg(NH₂)₂/LiH system for hydrogen storage. *Angew. Chem. Int. Ed.* **2009**, *48*, 5828–5832. [[CrossRef](#)] [[PubMed](#)]
211. Pistidda, C.; Santoru, A.; Garroni, S.; Bergemann, N.; Rzeszutek, A.; Horstmann, C.; Thomas, D.; Klassen, T.; Dornheim, M. First direct study of the ammonolysis reaction in the most common alkaline and alkaline earth metal hydrides by in situ SR-PXD. *J. Phys. Chem. C* **2015**, *119*, 934–943. [[CrossRef](#)]
212. Jacobs, H.; Von Osten, E. Die Kristallstruktur einer neuen modifikation des kaliumamids, KNH₂. *Z. Nat. B* **1976**, *31*, 385–386. [[CrossRef](#)]
213. Wang, J.; Chen, P.; Pan, H.; Xiong, Z.; Gao, M.; Wu, G.; Liang, C.; Li, C.; Li, B.; Wang, J. Solid-Solid heterogeneous catalysis: The role of potassium in promoting the dehydrogenation of the Mg(NH₂)₂/LiH composite. *ChemSusChem* **2013**, *6*, 2181–2189. [[CrossRef](#)]
214. Wang, J.; Wu, G.; Chua, Y.S.; Guo, J.; Xiong, Z.; Zhang, Y.; Gao, M.; Pan, H.; Chen, P. hydrogen sorption from the Mg(NH₂)₂-KH system and synthesis of an amide-imide complex of KMg(NH)(NH₂). *ChemSusChem* **2011**, *4*, 1622–1628. [[CrossRef](#)]
215. Napolitano, E.; Dolci, F.; Campesi, R.; Pistidda, C.; Hoelzel, M.; Moretto, P.; Enzo, S. Crystal structure solution of KMg(ND)(ND₂): An ordered mixed amide/imide compound. *Int. J. Hydrog. Energy* **2014**, *39*, 868–876. [[CrossRef](#)]
216. Palvadeau, P.; Rouxel, J. L'amidure ternaire K₂Mg(NH₂)₄, l'imidure K₂Mg(NH)₂ et le nitrure double KMgN. *CR Seances Acad. Sci. Ser. C* **1968**, *266*, 1605–1607.
217. Palvadeau, P.; Rouxel, J. Preparation and structural characterization of magnesium and alkaline metal double amides—M₂mg(Nh₂)₄ Derivatives. *Bull. Soc. Chim. Fr.* **1970**, 480–485.
218. Santoru, A.; Garroni, S.; Pistidda, C.; Milanese, C.; Girella, A.; Marini, A.; Masolo, E.; Valentoni, A.; Bergemann, N.; Le, T.T.; et al. A new potassium-based intermediate and its role in the desorption properties of the K-Mg-N-H system. *Phys. Chem. Chem. Phys.* **2016**, *18*, 3910–3920. [[CrossRef](#)] [[PubMed](#)]
219. Santoru, A.; Pistidda, C.; Sorby, M.H.; Chierotti, M.R.; Garroni, S.; Pinatel, E.; Karimi, F.; Cao, H.; Bergemann, N.; Le, T.T.; et al. KNH₂-KH: A metal amide-hydride solid solution. *Chem. Commun. (Camb)* **2016**, *52*, 11760–11763. [[CrossRef](#)] [[PubMed](#)]
220. Durojaiye, T.; Hayes, J.; Goudy, A. Rubidium hydride: An exceptional dehydrogenation catalyst for the lithium amide/magnesium hydride system. *J. Phys. Chem. C* **2013**, *117*, 6554–6560. [[CrossRef](#)]
221. Hayes, J.; Durojaiye, T.; Goudy, A. Hydriding and dehydriding kinetics of RbH-doped 2LiNH₂/MgH₂ hydrogen storage system. *J. Alloys Compd.* **2015**, *645*, S496–S499. [[CrossRef](#)]
222. Li, C.; Liu, Y.; Gu, Y.; Gao, M.; Pan, H. Improved hydrogen-storage thermodynamics and kinetics for an RbF-Doped Mg (NH₂)₂-2 LiH system. *Chem. Asian J.* **2013**, *8*, 2136–2143. [[CrossRef](#)]
223. Li, C.; Liu, Y.F.; Ma, R.J.; Zhang, X.; Li, Y.; Gao, M.X.; Pan, H.G. Superior dehydrogenation/hydrogenation kinetics and long-term cycling performance of K and Rb cocatalyzed Mg(NH₂)₂-2LiH system. *ACS Appl. Mater. Interfaces* **2014**, *6*, 17024–17033. [[CrossRef](#)]
224. Santoru, A.; Pistidda, C.; Brighi, M.; Chierotti, M.R.; Heere, M.; Karimi, F.; Cao, H.; Capurso, G.; Chaudhary, A.L.; Gizer, G.; et al. Insights into the Rb-Mg-N-H System: An ordered mixed amide/imide phase and a disordered amide/hydride solid solution. *Inorg Chem.* **2018**, *57*, 3197–3205. [[CrossRef](#)]
225. Durojaiye, T.; Hayes, J.; Goudy, A. Potassium, rubidium and cesium hydrides as dehydrogenation catalysts for the lithium amide/magnesium hydride system. *Int. J. Hydrog. Energy* **2015**, *40*, 2266–2273. [[CrossRef](#)]
226. Hayes, J.; Goudy, A. Thermodynamics, kinetics and modeling studies of KH-RbH-and CsH-doped 2LiNH₂/MgH₂ hydrogen storage systems. *Int. J. Hydrog. Energy* **2015**, *40*, 12336–12342. [[CrossRef](#)]

227. Zhang, J.X.; Liu, Y.F.; Zhang, X.; Yang, Y.X.; Zhang, Q.H.; Jin, T.; Wang, Y.X.; Gao, M.X.; Sun, L.X.; Pan, H.G. Synthesis of CsH and its effect on the hydrogen storage properties of the Mg(NH₂)₂-2LiH system. *Int. J. Hydrog. Energy* **2016**, *41*, 11264–11274. [[CrossRef](#)]
228. Zhang, J.; Wang, Y.; Zhang, M.; Leng, Z.; Gao, M.; Hu, J.; Liu, Y.; Pan, H. Improved overall hydrogen storage properties of a CsH and KH co-doped Mg(NH₂)₂/2LiH system by forming mixed amides of Li-K and Cs-Mg. *RSC Adv.* **2017**, *7*, 30357–30364. [[CrossRef](#)]
229. Callister, W.D., Jr.; Rethwisch, D.G. *Materials Science and Engineering: An Introduction*, 1 ed.; John Wiley & Sons: Hoboken, NJ, USA, 2014.
230. Blomgren, G.E.; Vanartsdalen, E.R. Fused salts. *Annu. Rev. Phys. Chem.* **1960**, *11*, 273–306. [[CrossRef](#)]
231. Sundermeyer, W. Fused salts and their use as reaction media. *Angew. Chem. Int. Ed.* **1965**, *4*, 222. [[CrossRef](#)]
232. Habashi, F. *Handbook of Extractive Metallurgy*; Wiley VCH: Weinheim, Germany, 1997.
233. Harries, D.N.; Paskevicius, M.; Sheppard, D.A.; Price, T.E.C.; Buckley, C.E. Concentrating solar thermal heat storage using metal hydrides. *Proc. IEEE* **2012**, *100*, 539–549. [[CrossRef](#)]
234. Paskevicius, M.; Pitt, M.P.; Brown, D.H.; Sheppard, D.A.; Chumphongphan, S.; Buckley, C.E. First-Order phase transition in the Li₂B₁₂H₁₂ system. *Phys. Chem. Chem. Phys.* **2013**, *15*, 15825–15828. [[CrossRef](#)]
235. Paskevicius, M.; Ley, M.B.; Sheppard, D.A.; Jensen, T.R.; Buckley, C.E. Eutectic melting in metal borohydrides. *Phys. Chem. Chem. Phys.* **2013**, *15*, 19774–19789. [[CrossRef](#)]
236. Lee, J.Y.; Ravnsbæk, D.; Lee, Y.-S.; Kim, Y.; Cerenius, Y.; Shim, J.-H.; Jensen, T.R.; Hur, N.H.; Cho, Y.W. Decomposition reactions and reversibility of the LiBH₄-Ca(BH₄)₂ composite. *J. Phys. Chem. C* **2009**, *113*, 15080–15086. [[CrossRef](#)]
237. Liu, Y.; Reed, D.; Paterakis, C.; Contreras Vasquez, L.; Baricco, M.; Book, D. Study of the decomposition of a 0.62LiBH₄-0.38NaBH₄ mixture. *Int. J. Hydrog. Energy* **2017**, *42*, 22480–22488. [[CrossRef](#)]
238. Roedern, E.; Hansen, B.R.S.; Ley, M.B.; Jensen, T.R. Effect of eutectic melting, reactive hydride composites, and nanoconfinement on decomposition and reversibility of LiBH₄-KBH₄. *J. Phys. Chem. C* **2015**, *119*, 25818–25825. [[CrossRef](#)]
239. Javadian, P.; Jensen, T.R. Enhanced hydrogen reversibility of nanoconfined LiBH₄-Mg(BH₄)₂. *Int. J. Hydrog. Energy* **2014**, *39*, 9871–9876. [[CrossRef](#)]
240. Doroodian, A.; Dengler, J.E.; Genest, A.; Rosch, N.; Rieger, B. Methylguanidinium borohydride: An ionic-liquid-based hydrogen-storage material. *Angew. Chem. Int. Ed. Engl.* **2010**, *49*, 1871–1873. [[CrossRef](#)] [[PubMed](#)]
241. Li, S.; Gao, H.; Shreeve, J.M. Borohydride ionic liquids and borane/ionic-liquid solutions as hypergolic fuels with superior low ignition-delay times. *Angew. Chem. Int. Ed. Engl.* **2014**, *53*, 2969–2972. [[CrossRef](#)]
242. Yan, Y.; Rentsch, D.; Remhof, A. Controllable decomposition of Ca(BH₄)₂ for reversible hydrogen storage. *Phys. Chem. Chem. Phys.* **2017**, *19*, 7788–7792. [[CrossRef](#)] [[PubMed](#)]
243. Li, H.W.; Orimo, S.; Nakamori, Y.; Miwa, K.; Ohba, N.; Towata, S.; Zuttel, A. Materials designing of metal borohydrides: Viewpoints from thermodynamical stabilities. *J. Alloys Compd.* **2007**, *446*, 315–318. [[CrossRef](#)]
244. Liu, X.; Peaslee, D.; Sheehan, T.P.; Majzoub, E.H. Decomposition behavior of eutectic LiBH₄-Mg(BH₄)₂ and its confinement effects in ordered nanoporous carbon. *J. Phys. Chem. C* **2014**, *118*, 27265–27271. [[CrossRef](#)]
245. Ley, M.B.; Roedern, E.; Jensen, T.R. Eutectic melting of LiBH₄-KBH₄. *Phys. Chem. Chem. Phys.* **2014**, *16*, 24194–24199. [[CrossRef](#)]
246. Javadian, P.; Sheppard, D.A.; Buckley, C.E.; Jensen, T.R. Hydrogen storage properties of nanoconfined LiBH₄-NaBH₄. *Int. J. Hydrog. Energy* **2015**, *40*, 14916–14924. [[CrossRef](#)]
247. Dematteis, E.M.; Roedern, E.; Pinatel, E.R.; Corno, M.; Jensen, T.R.; Baricco, M. A thermodynamic investigation of the LiBH₄-NaBH₄ system. *RSC Adv.* **2016**, *6*, 60101–60108. [[CrossRef](#)]
248. Jensen, S.R.H.; Jepsen, L.H.; Skibsted, J.; Jensen, T.R. Phase diagram for the NaBH₄-KBH₄ system and the stability of a Na_{1-x}K_xBH₄ solid solution. *J. Phys. Chem. C* **2015**, *119*, 27919–27929. [[CrossRef](#)]
249. Dematteis, E.M.; Pinatel, E.R.; Corno, M.; Jensen, T.R.; Baricco, M. Phase diagrams of the LiBH₄-NaBH₄-KBH₄ system. *Phys. Chem. Chem. Phys.* **2017**, *19*, 25071–25079. [[CrossRef](#)]
250. Bardají, E.G.; Zhao-Karger, Z.; Boucharat, N.; Nale, A.; van Setten, M.J.; Lohstroh, W.; Röhm, E.; Catti, M.; Fichtner, M. LiBH₄-Mg(BH₄)₂: A physical mixture of metal borohydrides as hydrogen storage material. *J. Phys. Chem. C* **2011**, *115*, 6095–6101. [[CrossRef](#)]

251. Fang, Z.Z.; Kang, X.D.; Wang, P.; Li, H.W.; Orimo, S.I. Unexpected dehydrogenation behavior of $\text{LiBH}_4/\text{Mg}(\text{BH}_4)_2$ mixture associated with the in situ formation of dual-cation borohydride. *J. Alloys Compd.* **2010**, *491*, L1–L4. [[CrossRef](#)]
252. Lee, H.S.; Lee, Y.S.; Suh, J.Y.; Kim, M.; Yu, J.S.; Cho, Y.W. Enhanced desorption and absorption properties of eutectic $\text{LiBH}_4\text{-Ca}(\text{BH}_4)_2$ infiltrated into mesoporous carbon. *J. Phys. Chem. C* **2011**, *115*, 20027–20035. [[CrossRef](#)]
253. Ley, M.; Roedern, E.; Thygesen, P.; Jensen, T. Melting behavior and thermolysis of $\text{NaBH}_4\text{-Mg}(\text{BH}_4)_2$ and $\text{NaBH}_4\text{-Ca}(\text{BH}_4)_2$ composites. *Energies* **2015**, *8*, 2701–2713. [[CrossRef](#)]
254. Huot, J.; Cuevas, F.; Deledda, S.; Edalati, K.; Filinchuk, Y.; Grosdidier, T.; Hauback, B.C.; Heere, M.; Jensen, T.R.; Latroche, M.; et al. Mechanochemistry of metal hydrides: Recent advances. *Materials* **2019**, *12*, 2778. [[CrossRef](#)]
255. Hino, S.; Fonnelop, J.E.; Corno, M.; Zavorotynska, O.; Damin, A.; Richter, B.; Baricco, M.; Jensen, T.R.; Sorby, M.H.; Hauback, B.C. Halide substitution in magnesium borohydride. *J. Phys. Chem. C* **2012**, *116*, 12482–12488. [[CrossRef](#)]
256. Rude, L.H.; Groppo, E.; Arnbjerg, L.M.; Ravnsbæk, D.B.; Malmkjær, R.A.; Filinchuk, Y.; Baricco, M.; Besenbacher, F.; Jensen, T.R. Iodide substitution in lithium borohydride, $\text{LiBH}_4\text{-LiI}$. *J. Alloys Compd.* **2011**, *509*, 8299–8305. [[CrossRef](#)]
257. Olsen, J.E.; Karen, P.; Sørby, M.H.; Hauback, B.C. Effect of chloride substitution on the order-disorder transition in NaBH_4 and $\text{Na}_{11}\text{BD}_4$. *J. Alloys Compd.* **2014**, *587*, 374–379. [[CrossRef](#)]
258. Grove, H.; Rude, L.H.; Jensen, T.R.; Corno, M.; Ugliengo, P.; Baricco, M.; Sorby, M.H.; Hauback, B.C. Halide substitution in $\text{Ca}(\text{BH}_4)_2$. *RSC Adv.* **2014**, *4*, 4736–4742. [[CrossRef](#)]
259. Rude, L.H.; Filinchuk, Y.; Sørby, M.H.; Hauback, B.C.; Besenbacher, F.; Jensen, T.R. Anion substitution in $\text{Ca}(\text{BH}_4)_2\text{-CaI}_2$: Synthesis, structure and stability of three new compounds. *J. Phys. Chem. C* **2011**, *115*, 7768–7777. [[CrossRef](#)]
260. Ravnsbæk, D.B.; Rude, L.H.; Jensen, T.R. Chloride substitution in sodium borohydride. *J. Solid State Chem.* **2011**, *184*, 1858–1866. [[CrossRef](#)]
261. Arnbjerg, L.M.; Ravnsbæk, D.B.; Filinchuk, Y.; Vang, R.T.; Cerenius, Y.; Besenbacher, F.; Jørgensen, J.-E.; Jakobsen, H.J.; Jensen, T.R. Structure and dynamics for $\text{LiBH}_4\text{-LiCl}$ solid solutions. *Chem. Mater.* **2009**, *21*, 5772–5782. [[CrossRef](#)]
262. Zavorotynska, O.; Corno, M.; Pinatel, E.; Rude, L.H.; Ugliengo, P.; Jensen, T.R.; Baricco, M. Theoretical and experimental study of $\text{LiBH}_4\text{-LiCl}$ solid solution. *Crystals* **2012**, *2*, 144–158. [[CrossRef](#)]
263. Pinatel, E.R.; Corno, M.; Ugliengo, P.; Baricco, M. Effects of metastability on hydrogen sorption in fluorine substituted hydrides. *J. Alloys Compd.* **2014**, *615*, S706–S710. [[CrossRef](#)]
264. Corno, M.; Pinatel, E.; Ugliengo, P.; Baricco, M. A computational study on the effect of fluorine substitution in LiBH_4 . *J. Alloys Compd.* **2011**, *509*, S679–S683. [[CrossRef](#)]
265. Rude, L.H.; Filso, U.; D’Anna, V.; Spyratou, A.; Richter, B.; Hino, S.; Zavorotynska, O.; Baricco, M.; Sorby, M.H.; Hauback, B.C.; et al. Hydrogen-Fluorine exchange in $\text{NaBH}_4\text{-NaBF}_4$. *Phys. Chem. Chem. Phys.* **2013**, *15*, 18185–18194. [[CrossRef](#)]
266. Richter, B.; Ravnsbæk, D.B.; Sharma, M.; Spyratou, A.; Hagemann, H.; Jensen, T.R. Fluoride substitution in LiBH_4 ; destabilization and decomposition. *Phys. Chem. Chem. Phys.* **2017**, *19*, 30157–30165. [[CrossRef](#)]
267. Lukas, H.L.; Fries, S.G.; Sundman, B. *Computational Thermodynamics: The Calphad Method*; Cambridge University Press: Cambridge, UK, 2007.
268. Adams, R.M. *Borax to Boranes*; American Chemical Society: Washington, DC, USA, 1961; Volume 32, pp. 60–68.
269. Semenenko, K.N.; Chavgun, A.P.; Surov, V.N. Interaction of sodium tetrahydroborate with potassium and lithium tetrahydroborates. *Russ. J. Inorg. Chem.* **1971**, *16*, 271–273.
270. Skripov, A.V.; Solonin, A.V.; Rude, L.H.; Jensen, T.R.; Filinchuk, Y. Nuclear magnetic resonance studies of reorientational motion and Li diffusion in $\text{LiBH}_4\text{-LiI}$ solid solutions. *J. Phys. Chem. C* **2012**, *116*, 26177–26184. [[CrossRef](#)]
271. Huff, G.F. Method and composition for subjecting metals to reducing conditions. U.S. Patent No. 2,935,428, 3 May 1960.
272. Dematteis, E.M.; Baricco, M. Hydrogen Desorption in $\text{Mg}(\text{BH}_4)_2\text{-Ca}(\text{BH}_4)_2$ System. *Energies* **2019**, *12*, 3230. [[CrossRef](#)]

273. Dematteis, E.M.; Pistidda, C.; Dornheim, M.; Baricco, M. Exploring ternary and quaternary mixtures in the $\text{LiBH}_4\text{-NaBH}_4\text{-KBH}_4\text{-Mg}(\text{BH}_4)_2\text{-Ca}(\text{B}_4)_2$ system. *ChemPhysChem* **2019**, *20*, 1348–1359. [[CrossRef](#)] [[PubMed](#)]
274. Dematteis, E.M.; Santoru, A.; Poletti, M.G.; Pistidda, C.; Klassen, T.; Dornheim, M.; Baricco, M. Phase stability and hydrogen desorption in a quinary equimolar mixture of light-metals borohydrides. *Int. J. Hydrog. Energy* **2018**, *43*, 16793–16803. [[CrossRef](#)]
275. Milanese, C.; Garroni, S.; Girella, A.; Mulas, G.; Berbenni, V.; Bruni, G.; Suriñach, S.; Baró, M.D.; Marini, A. Thermodynamic and kinetic investigations on pure and doped $\text{NaBH}_4\text{-MgH}_2$ system. *J. Phys. Chem. C* **2011**, *115*, 3151–3162. [[CrossRef](#)]
276. Nakamori, Y.; Miwa, K.; Ninomiya, A.; Li, H.W.; Ohba, N.; Towata, S.I.; Zuttel, A.; Orimo, S.I. Correlation between thermodynamical stabilities of metal borohydrides and cation electronegativities: First-principles calculations and experiments. *Phys. Rev. B* **2006**, *74*. [[CrossRef](#)]
277. Liu, Y.; Heere, M.; Contreras Vasquez, L.; Paterakis, C.; Sørby, M.H.; Hauback, B.C.; Book, D. Dehydrogenation and rehydrogenation of a 0.62 $\text{LiBH}_4\text{-0.38NaBH}_4$ mixture with nano-sized Ni. *Int. J. Hydrog. Energy* **2018**, *43*, 16782–16792. [[CrossRef](#)]
278. Liu, Y. Low Melting Point Alkali Metal Borohydride Mixtures for Hydrogen Storage. Ph.D. Thesis, University Birmingham, Birmingham, UK, 2018.
279. Chaudhary, A.-L.; Li, G.; Matsuo, M.; Orimo, S.-i.; Deledda, S.; Sørby, M.H.; Hauback, B.C.; Pistidda, C.; Klassen, T.; Dornheim, M. Simultaneous desorption behavior of M borohydrides and Mg_2FeH_6 reactive hydride composites (M = Mg, then Li, Na, K, Ca). *Appl. Phys. Lett.* **2015**, *107*, 073905. [[CrossRef](#)]
280. Afonso, G.; Bonakdarpour, A.; Wilkinson, D.P. Hydrogen storage properties of the destabilized $\text{}_4\text{NaBH}_4/\text{}_5\text{Mg}_2\text{NiH}_4$ composite system. *J. Phys. Chem. C* **2013**, *117*, 21105–21111. [[CrossRef](#)]
281. Bergemann, N.; Pistidda, C.; Uptmoor, M.; Milanese, C.; Santoru, A.; Emmeler, T.; Puzskiel, J.; Dornheim, M.; Klassen, T. A new mutually destabilized reactive hydride system: $\text{LiBH}_4\text{-Mg}_2\text{NiH}_4$. *J. Energy Chem.* **2019**, *34*, 240–254. [[CrossRef](#)]
282. Javadian, P.; Zlotea, C.; Ghimbeu, C.M.; Lacroche, M.; Jensen, T.R. Hydrogen storage properties of nanoconfined $\text{LiBH}_4\text{-Mg}_2\text{NiH}_4$ reactive hydride composites. *J. Phys. Chem. C* **2015**, *119*, 5819–5826. [[CrossRef](#)]
283. Li, W.; Vajo, J.J.; Cumberland, R.W.; Liu, P.; Hwang, S.J.; Kim, C.; Bowman, R.C. Hydrogenation of magnesium nickel boride for reversible hydrogen storage. *J. Phys. Chem. Lett.* **2010**, *1*, 69–72. [[CrossRef](#)]
284. Vajo, J.J.; Li, W.; Liu, P. Thermodynamic and kinetic destabilization in $\text{LiBH}_4/\text{Mg}_2\text{NiH}_4$: Promise for borohydride-based hydrogen storage. *Chem. Commun. (Camb)* **2010**, *46*, 6687–6689. [[CrossRef](#)] [[PubMed](#)]
285. Bergemann, N.; Pistidda, C.; Milanese, C.; Emmeler, T.; Karimi, F.; Chaudhary, A.L.; Chierotti, M.R.; Klassen, T.; Dornheim, M. $\text{Ca}(\text{BH}_4)_2\text{-Mg}_2\text{NiH}_4$: On the pathway to a $\text{Ca}(\text{BH}_4)_2$ system with a reversible hydrogen cycle. *Chem. Commun. (Camb)* **2016**, *52*, 4836–4839. [[CrossRef](#)] [[PubMed](#)]
286. Paterakis, C.; Guo, S.; Heere, M.; Liu, Y.; Contreras, L.F.; Sørby, M.H.; Hauback, B.C.; Reed, D.; Book, D. Study of the $\text{NaBH}_4\text{-NaBr}$ system and the behaviour of its low temperature phase transition. *Int. J. Hydrog. Energy* **2017**, *42*, 22538–22543. [[CrossRef](#)]
287. Bogdanovic, B.; Schwickardi, M. Ti-Doped alkali metal aluminium hydrides as potential novel reversible hydrogen storage materials. *J. Alloys Compd.* **1997**, *253*, 1–9. [[CrossRef](#)]
288. Liu, J.; Zhang, W. Improvement on hydrogen storage properties of complex metal hydride. *Conf. Proc.* **2012**, 29–48.
289. Milanese, C.; Jensen, T.R.; Hauback, B.C.; Pistidda, C.; Dornheim, M.; Yang, H.; Lombardo, L.; Zuttel, A.; Filinchuk, Y.; Ngene, P.; et al. Complex hydrides for energy storage. *Int. J. Hydrog. Energy* **2019**, *44*, 7860–7874. [[CrossRef](#)]
290. Moysés Araújo, C.; Scheicher, R.H.; Ahuja, R. Thermodynamic analysis of hydrogen sorption reactions in Li-Mg-N-H systems. *Appl. Phys. Lett.* **2008**, *92*, 021907. [[CrossRef](#)]
291. Barkhordarian, G.; Klassen, T.; Dornheim, M.; Bormann, R. Unexpected kinetic effect of MgB_2 in reactive hydride composites containing complex borohydrides. *J. Alloys Compd.* **2007**, *440*, L18–L21. [[CrossRef](#)]
292. Reilly, J.J.; Wiswall, R.H. Reaction of hydrogen with alloys of magnesium and copper. *Inorg. Chem.* **1967**, *6*, 2220. [[CrossRef](#)]
293. Vajo, J.J.; Olson, G.L. Hydrogen storage in destabilized chemical systems. *Scr. Mater.* **2007**, *56*, 829–834. [[CrossRef](#)]

294. Vajo, J.J.; Skeith, S.L.; Mertens, F. Reversible storage of hydrogen in destabilized LiBH₄. *J. Phys. Chem. B* **2005**, *109*, 3719–3722. [[CrossRef](#)] [[PubMed](#)]
295. Dornheim, M.; Doppiu, S.; Barkhordarian, G.; Boesenberg, U.; Klassen, T.; Gutfleisch, O.; Bormann, R. Hydrogen storage in magnesium-based hydrides and hydride composites. *Scr. Mater.* **2007**, *56*, 841–846. [[CrossRef](#)]
296. Bösenberg, U.; Kim, J.W.; Gossler, D.; Eigen, N.; Jensen, T.R.; von Colbe, J.M.B.; Zhou, Y.; Dahms, M.; Kim, D.H.; Günther, R. Role of additives in LiBH₄-MgH₂ reactive hydride composites for sorption kinetics. *Acta Mater.* **2010**, *58*, 3381–3389. [[CrossRef](#)]
297. Bosenberg, U.; Vainio, U.; Pranzas, P.K.; von Colbe, J.M.; Goerigk, G.; Welter, E.; Dornheim, M.; Schreyer, A.; Bormann, R. On the chemical state and distribution of Zr- and V-based additives in reactive hydride composites. *Nanotechnology* **2009**, *20*, 204003. [[CrossRef](#)] [[PubMed](#)]
298. Deprez, E.; Justo, A.; Rojas, T.C.; López-Cartés, C.; Bonatto Minella, C.; Bösenberg, U.; Dornheim, M.; Bormann, R.; Fernández, A. Microstructural study of the LiBH₄-MgH₂ reactive hydride composite with and without Ti-isopropoxide additive. *Acta Mater.* **2010**, *58*, 5683–5694. [[CrossRef](#)]
299. Deprez, E.; Muñoz-Márquez, M.A.; Roldán, M.A.; Prestipino, C.; Palomares, F.J.; Minella, C.B.; Bösenberg, U.; Dornheim, M.; Bormann, R.; Fernández, A. Oxidation state and local structure of Ti-based additives in the reactive hydride composite $2\text{LiBH}_4 + \text{MgH}_2$. *J. Phys. Chem. C* **2010**, *114*, 3309–3317. [[CrossRef](#)]
300. Fan, M.; Sun, L.; Zhang, Y.; Xu, F.; Zhang, J.; Chu, H. The catalytic effect of additive Nb₂O₅Nb₂O₅ on the reversible hydrogen storage performances of LiBH₄-MgH₂/LiBH₄-MgH₂ composite. *Int. J. Hydrog. Energy* **2008**, *33*, 74–80. [[CrossRef](#)]
301. Kou, H.Q.; Sang, G.; Zhou, Y.L.; Wang, X.Y.; Huang, Z.Y.; Luo, W.H.; Chen, L.X.; Xiao, X.Z.; Yang, G.Y.; Hu, C.W. Enhanced hydrogen storage properties of LiBH₄ modified by NbF₅. *Int. J. Hydrog. Energy* **2014**, *39*, 11675–11682. [[CrossRef](#)]
302. Liu, B.H.; Zhang, B.J.; Jiang, Y. Hydrogen storage performance of LiBH_{4+1/2}MgH₂ composites improved by Ce-based additives. *Int. J. Hydrog. Energy* **2011**, *36*, 5418–5424. [[CrossRef](#)]
303. Sridechprasat, P.; Suttisawat, Y.; Rangsunvigit, P.; Kitiyanan, B.; Kulprathipanja, S. Catalyzed LiBH₄ and MgH₂ mixture for hydrogen storage. *Int. J. Hydrog. Energy* **2011**, *36*, 1200–1205. [[CrossRef](#)]
304. Wang, P.; Ma, L.; Fang, Z.; Kang, X.; Wang, P. Improved hydrogen storage property of Li-Mg-B-H system by milling with titanium trifluoride. *Energy Environ. Sci.* **2009**, *2*. [[CrossRef](#)]
305. Li, Y.; Izuhara, T.; Takeshita, H.T. Promotional effect of aluminum on MgH₂ + LiBH₄ hydrogen storage materials. *Mater. Trans.* **2011**, *52*, 641–646. [[CrossRef](#)]
306. Bellosta von Colbe, J.; Ares, J.-R.; Barale, J.; Baricco, M.; Buckley, C.; Capurso, G.; Gallandat, N.; Grant, D.M.; Guzik, M.N.; Jacob, I.; et al. Application of hydrides in hydrogen storage and compression: Achievements, outlook and perspectives. *Int. J. Hydrog. Energy* **2019**, *44*, 7780–7808. [[CrossRef](#)]
307. Broom, D.P.; Webb, C.J.; Fanourgakis, G.S.; Froudakis, G.E.; Trikalitis, P.N.; Hirscher, M. Concepts for improving hydrogen storage in nanoporous materials. *Int. J. Hydrog. Energy* **2019**, *44*, 7768–7779. [[CrossRef](#)]
308. Balde, C.P.; Hereijgers, B.P.; Bitter, J.H.; de Jong, K.P. Facilitated hydrogen storage in NaAlH₄ supported on carbon nanofibers. *Angew. Chem. Int. Ed. Engl.* **2006**, *45*, 3501–3503. [[CrossRef](#)]
309. Berube, V.; Chen, G.; Dresselhaus, M.S. Impact of nanostructuring on the enthalpy of formation of metal hydrides. *Int. J. Hydrog. Energy* **2008**, *33*, 4122–4131. [[CrossRef](#)]
310. Kim, H.; Karkamkar, A.; Autrey, T.; Chupas, P.; Proffen, T. Determination of structure and phase transition of light element nanocomposites in mesoporous silica: Case study of NH₃BH₃ in MCM-41. *J. Am. Chem. Soc.* **2009**, *131*, 13749–13755. [[CrossRef](#)]
311. Nielsen, T.K.; Bosenberg, U.; Gosalawit, R.; Dornheim, M.; Cerenius, Y.; Besenbacher, F.; Jensen, T.R. A reversible nanoconfined chemical reaction. *ACS Nano* **2010**, *4*, 3903–3908. [[CrossRef](#)]
312. Sabrina, S.; Kenneth, D.K.; Zhirong, Z.-K.; Eisa Gil, B.; Maximilian, F.; Bjørn, C.H. Small-Angle scattering investigations of Mg-borohydride infiltrated in activated carbon. *Nanotechnology* **2009**, *20*, 505702.
313. Zaluski, L.; Zaluska, A.; Strom-Olsen, J.O. Nanocrystalline metal hydrides. *J. Alloys Compd.* **1997**, *253*, 70–79. [[CrossRef](#)]
314. Nwakwuo, C.C.; Pistidda, C.; Dornheim, M.; Hutchison, J.L.; Sykes, J.M. Microstructural analysis of hydrogen absorption in 2NaH + MgB₂. *Scr. Mater.* **2011**, *64*, 351–354. [[CrossRef](#)]

315. Garroni, S.; Pistidda, C.; Brunelli, M.; Vaughan, G.B.M.; Surinach, S.; Baro, M.D. Hydrogen desorption mechanism of $2\text{NaBH}_4 + \text{MgH}_2$ composite prepared by high-energy ball milling. *Scr. Mater.* **2009**, *60*, 1129–1132. [[CrossRef](#)]
316. Mao, J.F.; Yu, X.B.; Guo, Z.P.; Liu, H.K.; Wu, Z.; Ni, J. Enhanced hydrogen storage performances of $\text{NaBH}_4\text{-MgH}_2$ system. *J. Alloys Compd.* **2009**, *479*, 619–623. [[CrossRef](#)]
317. Pistidda, C.; Napolitano, E.; Pottmaier, D.; Dornheim, M.; Klassen, T.; Baricco, M.; Enzo, S. Structural study of a new B-rich phase obtained by partial hydrogenation of $2\text{NaH} + \text{MgB}_2$. *Int. J. Hydrog. Energy* **2013**, *38*, 10479–10484. [[CrossRef](#)]
318. Pistidda, C.; Garroni, S.; Minella, C.B.; Dolci, F.; Jensen, T.R.; Nolis, P.; Bosenberg, U.; Cerenius, Y.; Lohstroh, W.; Fichtner, M.; et al. Pressure effect on the $2\text{NaH} + \text{MgB}_2$ hydrogen absorption reaction. *J. Phys. Chem. C* **2010**, *114*, 21816–21823. [[CrossRef](#)]
319. Heere, M.; Sorby, M.H.; Pistidda, C.; Dornheim, M.; Hauback, B.C. Milling time effect of Reactive hydride composites of NaF-NaH-MgB_2 investigated by in situ powder diffraction. *Int. J. Hydrog. Energy* **2016**, *41*, 13101–13108. [[CrossRef](#)]
320. Le, T.-T.; Pistidda, C.; Puszkiel, J.; Castro Riglos, M.V.; Karimi, F.; Skibsted, J.; GharibDoust, S.P.; Richter, B.; Emmeler, T.; Milanese, C.; et al. Design of a nanometric AlTi additive for MgB_2 -based reactive hydride composites with superior kinetic properties. *J. Phys. Chem. C* **2018**, *122*, 7642–7655. [[CrossRef](#)]
321. Mangan, M.A.; Kral, M.V.; Spanos, G. Correlation between the crystallography and morphology of proeutectoid Widmanstätten cementite precipitates. *Acta Mater.* **1999**, *47*, 4263–4274. [[CrossRef](#)]
322. Zhang, M.X.; Kelly, P.M. Edge-to-edge matching model for predicting orientation relationships and habit planes—The improvements. *Scr. Mater.* **2005**, *52*, 963–968. [[CrossRef](#)]
323. Bonatto Minella, C.; Pellicer, E.; Rossinyol, E.; Karimi, F.; Pistidda, C.; Garroni, S.; Milanese, C.; Nolis, P.; Baró, M.D.; Gutfleisch, O.; et al. Chemical state, distribution, and role of Ti- and Nb-based additives on the $\text{Ca}(\text{BH}_4)_2$ system. *J. Phys. Chem. C* **2013**, *117*, 4394–4403. [[CrossRef](#)]
324. Puszkiel, J.A.; Gennari, F.C.; Larochette, P.A.; Ramallo-López, J.M.; Vainio, U.; Karimi, F.; Pranzas, P.K.; Troiani, H.; Pistidda, C.; Jepsen, J.; et al. Effect of Fe additive on the hydrogenation-dehydrogenation properties of $2\text{LiH} + \text{MgB}_2/2\text{LiBH}_4 + \text{MgH}_2$ system. *J. Power Sources* **2015**, *284*, 606–616. [[CrossRef](#)]
325. Pranzas, P.K.; Bosenberg, U.; Karimi, F.; Munning, M.; Metz, O.; Minella, C.B.; Schmitz, H.W.; Beckmann, F.; Vainio, U.; Zajac, D.; et al. Characterization of hydrogen storage materials and systems with photons and neutrons. *Adv. Eng. Mater.* **2011**, *13*, 730–736. [[CrossRef](#)]
326. Gleiter, H. Nanostructured materials: Basic concepts and microstructure. *Acta Mater.* **2000**, *48*, 1–29. [[CrossRef](#)]
327. Berube, F.; Kaliaguine, S. Calcination and thermal degradation mechanisms of triblock copolymer template in SBA-15 materials. *Microporous Mesoporous Mater.* **2008**, *115*, 469–479. [[CrossRef](#)]
328. Berube, V.; Radtke, G.; Dresselhaus, M.; Chen, G. Size effects on the hydrogen storage properties of nanostructured metal hydrides: A review. *Int. J. Energy Res.* **2007**, *31*, 637–663. [[CrossRef](#)]
329. Fichtner, M. Properties of nanoscale metal hydrides. *Nanotechnology* **2009**, *20*. [[CrossRef](#)] [[PubMed](#)]
330. Stuhr, U.; Wipf, H.; Udovic, T.J.; Weissmuller, J.; Gleiter, H. The vibrational excitations and the position of hydrogen in nanocrystalline palladium. *J. Phys. Condens. Matter* **1995**, *7*, 219–230. [[CrossRef](#)]
331. Koch, C.C. Synthesis of nanostructured materials by mechanical milling: Problems and opportunities. *Nanostruct. Mater.* **1997**, *9*, 13–22. [[CrossRef](#)]
332. Zhang, D.L. Processing of advanced materials using high-energy mechanical milling. *Prog. Mater. Sci.* **2004**, *49*, 537–560. [[CrossRef](#)]
333. Suryanarayana, C. Mechanical alloying and milling. *Prog. Mater. Sci.* **2001**, *46*, 1–184. [[CrossRef](#)]
334. Isaacoff, B.P.; Brown, K.A. Progress in top-down control of bottom-up assembly. *Nano Lett* **2017**, *17*, 6508–6510. [[CrossRef](#)] [[PubMed](#)]
335. Thanh, N.T.; Maclean, N.; Mahiddine, S. Mechanisms of nucleation and growth of nanoparticles in solution. *Chem. Rev.* **2014**, *114*, 7610–7630. [[CrossRef](#)] [[PubMed](#)]
336. Norberg, N.S.; Arthur, T.S.; Fredrick, S.J.; Prieto, A.L. Size-Dependent Hydrogen storage properties of Mg nanocrystals prepared from solution. *J. Am. Chem. Soc.* **2011**, *133*, 10679–10681. [[CrossRef](#)] [[PubMed](#)]
337. Grammatikopoulos, P.; Steinhauer, S.; Vernieres, J.; Singh, V.; Sowwan, M. Nanoparticle design by gas-phase synthesis. *Adv. Phys. X* **2016**, *1*, 81–100. [[CrossRef](#)]

338. Kalidindi, S.B.; Jagirdar, B.R. Highly monodisperse colloidal magnesium nanoparticles by room temperature digestive ripening. *Inorg. Chem.* **2009**, *48*, 4524–4529. [[CrossRef](#)] [[PubMed](#)]
339. Vajo, J.J.; Salguero, T.T.; Gross, A.E.; Skeith, S.L.; Olson, G.L. Thermodynamic destabilization and reaction kinetics in light metal hydride systems. *J. Alloys Compd.* **2007**, *446*, 409–414. [[CrossRef](#)]
340. Kumar, A.; Jeon, K.W.; Kumari, N.; Lee, I.S. Spatially confined formation and transformation of nanocrystals within nanometer-sized reaction media. *Acc. Chem. Res.* **2018**, *51*, 2867–2879. [[CrossRef](#)]
341. Pacula, A.; Mokaya, R. Synthesis and high hydrogen storage capacity of zeolite-like carbons nanocast using as-synthesized zeolite templates. *J. Phys. Chem. C* **2008**, *112*, 2764–2769. [[CrossRef](#)]
342. Wang, H.; Gao, Q.; Hu, J. High hydrogen storage capacity of porous carbons prepared by using activated carbon. *J. Am. Chem. Soc.* **2009**, *131*, 7016–7022. [[CrossRef](#)]
343. Surrey, A.; Minella, C.B.; Fechler, N.; Antonietti, M.; Grafe, H.J.; Schultz, L.; Rellinghaus, B. Improved hydrogen storage properties of LiBH₄ via nanoconfinement in micro- and mesoporous aerogel-like carbon. *Int. J. Hydrog. Energy* **2016**, *41*, 5540–5548. [[CrossRef](#)]
344. de Jongh, P.E.; Eggenhuisen, T.M. Melt infiltration: An emerging technique for the preparation of novel functional nanostructured materials. *Adv. Mater.* **2013**, *25*, 6672–6690. [[CrossRef](#)] [[PubMed](#)]
345. Rouquerol, J.; Avnir, D.; Fairbridge, C.W.; Everett, D.H.; Haynes, J.M.; Pernicone, N.; Ramsay, J.D.F.; Sing, K.S.W.; Unger, K.K. Recommendations for the characterization of porous solids (Technical Report). *Pure Appl. Chem.* **1994**, *66*, 1739–1758. [[CrossRef](#)]
346. Liu, Y.X.; Deng, J.G.; Xie, S.H.; Wang, Z.W.; Dai, H.X. Catalytic removal of volatile organic compounds using ordered porous transition metal oxide and supported noble metal catalysts. *Chin. J. Catal.* **2016**, *37*, 1193–1205. [[CrossRef](#)]
347. Trinidad, J.; Marco, I.; Arruebarrena, G.; Wendt, J.; Letzig, D.; de Argandona, E.; Goodall, R. Processing of magnesium porous structures by infiltration casting for biomedical applications. *Adv. Eng. Mater.* **2014**, *16*, 241–247. [[CrossRef](#)]
348. Banerjee, A.; Chandran, R.B.; Davidson, J.H. Experimental investigation of a reticulated porous alumina heat exchanger for high temperature gas heat recovery. *Appl. Therm. Eng.* **2015**, *75*, 889–895. [[CrossRef](#)]
349. Lai, Q.; Paskevicius, M.; Sheppard, D.A.; Buckley, C.E.; Thornton, A.W.; Hill, M.R.; Gu, Q.; Mao, J.; Huang, Z.; Liu, H.K.; et al. Hydrogen storage materials for mobile and stationary applications: Current state of the art. *ChemSusChem* **2015**, *8*, 2789–2825. [[CrossRef](#)]
350. Mosegaard, L.; Moller, B.; Jorgensen, J.E.; Bosenberg, U.; Dornheim, M.; Hanson, J.C.; Cerenius, Y.; Walker, G.; Jakobsen, H.J.; Besenbacher, F.; et al. Intermediate phases observed during decomposition of LiBH₄. *J. Alloys Compd.* **2007**, *446*, 301–305. [[CrossRef](#)]
351. Ngene, P.; Adelhelm, P.; Beale, A.M.; de Jong, K.P.; de Jongh, P.E. LiBH₄/SBA-15 nanocomposites prepared by melt infiltration under hydrogen pressure: Synthesis and hydrogen sorption properties. *J. Phys. Chem. C* **2010**, *114*, 6163–6168. [[CrossRef](#)]
352. Peru, F.; Garroni, S.; Campesi, R.; Milanese, C.; Marini, A.; Pellicer, E.; Baro, M.D.; Mulas, G. Ammonia-free infiltration of NaBH₄ into highly-ordered mesoporous silica and carbon matrices for hydrogen storage. *J. Alloys Compd.* **2013**, *580*, S309–S312. [[CrossRef](#)]
353. Adelhelm, P.; de Jongh, P.E. The impact of carbon materials on the hydrogen storage properties of light metal hydrides. *J. Mater. Chem.* **2011**, *21*, 2417–2427. [[CrossRef](#)]
354. Ampoumogli, A.; Steriotis, T.; Trikalitis, P.; Bardaji, E.G.; Fichtner, M.; Stubos, A.; Charalambopoulou, G. Synthesis and characterisation of a mesoporous carbon/calcium borohydride nanocomposite for hydrogen storage. *Int. J. Hydrog. Energy* **2012**, *37*, 16631–16635. [[CrossRef](#)]
355. Comanescu, C.; Capurso, G.; Maddalena, A. Nanoconfinement in activated mesoporous carbon of calcium borohydride for improved reversible hydrogen storage. *Nanotechnology* **2012**, *23*. [[CrossRef](#)] [[PubMed](#)]
356. Lai, Q.W.; Wang, T.; Sun, Y.H.; Aguey-Zinsou, K.F. Rational design of nanosized light elements for hydrogen storage: Classes, synthesis, characterization, and properties. *Adv. Mater. Technol.* **2018**, *3*. [[CrossRef](#)]
357. Cahen, S.; Eymery, J.B.; Janot, R.; Tarascon, J.M. Improvement of the LiBH₄ hydrogen desorption by inclusion into mesoporous carbons. *J. Power Sources* **2009**, *189*, 902–908. [[CrossRef](#)]
358. Verdal, N.; Udovic, T.J.; Rush, J.J.; Liu, X.F.; Majzoub, E.H.; Vajo, J.J.; Gross, A.F. Dynamical perturbations of tetrahydroborate anions in LiBH₄ due to nanoconfinement in controlled-pore carbon scaffolds. *J. Phys. Chem. C* **2013**, *117*, 17983–17995. [[CrossRef](#)]

359. Fang, Z.Z.; Wang, P.; Rufford, T.E.; Kang, X.D.; Lu, G.Q.; Cheng, H.M. Kinetic-and thermodynamic-based improvements of lithium borohydride incorporated into activated carbon. *Acta Mater.* **2008**, *56*, 6257–6263. [[CrossRef](#)]
360. Plerdsranoy, P.; Wiset, N.; Milanese, C.; Laipple, D.; Marini, A.; Klassen, T.; Dornheim, M.; Utike, R.G. Improvement of thermal stability and reduction of LiBH₄/polymer host interaction of nanoconfined LiBH₄ for reversible hydrogen storage. *Int. J. Hydrog. Energy* **2015**, *40*, 392–402. [[CrossRef](#)]
361. Gross, A.F.; Vajo, J.J.; Van Atta, S.L.; Olson, G.L. Enhanced hydrogen storage kinetics of LiBH₄ in nanoporous carbon scaffolds. *J. Phys. Chem. C* **2008**, *112*, 5651–5657. [[CrossRef](#)]
362. Liu, X.F.; Peaslee, D.; Jost, C.Z.; Majzoub, E.H. Controlling the Decomposition pathway of LiBH₄ via confinement in highly ordered nanoporous carbon. *J. Phys. Chem. C* **2010**, *114*, 14036–14041. [[CrossRef](#)]
363. Suwarno Ngene, P.; Nale, A.; Eggenhuisen, T.M.; Oschatz, M.; Embs, J.P.; Remhof, A.; de Jongh, P.E. Confinement effects for lithium borohydride: Comparing silica and carbon scaffolds. *J. Phys. Chem. C Nanomater. Interfaces* **2017**, *121*, 4197–4205. [[CrossRef](#)]
364. Plerdsranoy, P.; Kaewsuwan, D.; Chanlek, N.; Utke, R. Effects of specific surface area and pore volume of activated carbon nanofibers on nanoconfinement and dehydrogenation of LiBH₄. *Int. J. Hydrog. Energy* **2017**, *42*, 6189–6201. [[CrossRef](#)]
365. Guo, L.L.; Li, Y.; Ma, Y.F.; Liu, Y.; Peng, D.D.; Zhang, L.; Han, S.M. Enhanced hydrogen storage capacity and reversibility of LiBH₄ encapsulated in carbon nanocages. *Int. J. Hydrog. Energy* **2017**, *42*, 2215–2222. [[CrossRef](#)]
366. Thiangviriya, S.; Utke, R. LiBH₄ nanoconfined in activated carbon nanofiber for reversible hydrogen storage. *Int. J. Hydrog. Energy* **2015**, *40*, 4167–4174. [[CrossRef](#)]
367. Liu, X.F.; Peaslee, D.; Jost, C.Z.; Baumann, T.F.; Majzoub, E.H. Systematic pore-size effects of nanoconfinement of LiBH₄: Elimination of diborane release and tunable behavior for hydrogen storage applications. *Chem. Mater.* **2011**, *23*, 1331–1336. [[CrossRef](#)]
368. Ugrnani, J.; Torres, F.J.; Palumbo, M.; Baricco, M. Hydrogen release from solid state NaBH₄. *Int. J. Hydrog. Energy* **2008**, *33*, 3111–3115. [[CrossRef](#)]
369. Ngene, P.; van den Berg, R.; Verkuijlen, M.H.W.; de Jong, K.P.; de Jongh, P.E. Reversibility of the hydrogen desorption from NaBH₄ by confinement in nanoporous carbon. *Energy Environ. Sci.* **2011**, *4*, 4108–4115. [[CrossRef](#)]
370. Martelli, P.; Caputo, R.; Remhof, A.; Mauron, P.; Borgschulte, A.; Zuttel, A. Stability and Decomposition of NaBH₄. *J. Phys. Chem. C* **2010**, *114*, 7173–7177. [[CrossRef](#)]
371. Ampoumogli, A.; Steriotis, T.; Trikalitis, P.; Giasafaki, D.; Bardaji, E.G.; Fichtner, M.; Charalambopoulou, G. Nanostructured composites of mesoporous carbons and boranates as hydrogen storage materials. *J. Alloys Compd.* **2011**, *509*, S705–S708. [[CrossRef](#)]
372. Chong, L.; Zeng, X.; Ding, W.; Liu, D.J.; Zou, J. NaBH₄ in “Graphene Wrapper”: Significantly enhanced hydrogen storage capacity and regenerability through nanoencapsulation. *Adv. Mater.* **2015**, *27*, 5070–5074. [[CrossRef](#)]
373. Filinchuk, Y.; Richter, B.; Jensen, T.R.; Dmitriev, V.; Chernyshov, D.; Hagemann, H. Porous and dense magnesium borohydride frameworks: Synthesis, stability, and reversible absorption of guest species. *Angew. Chem. Int. Ed. Engl.* **2011**, *50*, 11162–11166. [[CrossRef](#)]
374. Heere, M.; Zavorotynska, O.; Deledda, S.; Sorby, M.H.; Book, D.; Steriotis, T.; Hauback, B.C. Effect of additives, ball milling and isotopic exchange in porous magnesium borohydride. *RSC Adv.* **2018**, *8*, 27645–27653. [[CrossRef](#)]
375. Paskevicius, M.; Pitt, M.P.; Webb, C.J.; Sheppard, D.A.; Filsø, U.; Gray, E.M.; Buckley, C.E. In-Situ X-ray diffraction study of γ -Mg(BH₄)₂ decomposition. *J. Phys. Chem. C* **2012**, *116*, 15231–15240. [[CrossRef](#)]
376. Zavorotynska, O.; El-Kharbachi, A.; Deledda, S.; Hauback, B.C. Recent progress in magnesium borohydride Mg(BH₄)₂: Fundamentals and applications for energy storage. *Int. J. Hydrog. Energy* **2016**, *41*, 14387–14403. [[CrossRef](#)]
377. Lohstroh, W.; Heere, M. Structure and dynamics of borohydrides studied by neutron scattering techniques: A review. *J. Phys. Soc. Jpn.* **2020**, *89*. [[CrossRef](#)]
378. Chłopek, K.; Frommen, C.; Léon, A.; Zabara, O.; Fichtner, M. Synthesis and properties of magnesium tetrahydroborate, Mg(BH₄)₂. *J. Mater. Chem.* **2007**, *17*, 3496–3503. [[CrossRef](#)]

379. Dai, B.; Sholl, D.S.; Johnson, J.K. First-Principles study of experimental and hypothetical $\text{Mg}(\text{BH}_4)_2$ crystal structures. *J. Phys. Chem. C* **2008**, *112*, 4391–4395. [[CrossRef](#)]
380. Fichtner, M.; Zhao-Karger, Z.; Hu, J.; Roth, A.; Weidler, P. The kinetic properties of $\text{Mg}(\text{BH}_4)_2$ infiltrated in activated carbon. *Nanotechnology* **2009**, *20*. [[CrossRef](#)]
381. Clemenccon, D.; Davoisne, C.; Chotard, J.N.; Janot, R. Enhancement of the hydrogen release of $\text{Mg}(\text{BH}_4)_2$ by concomitant effects of nano-confinement and catalysis. *Int. J. Hydrog. Energy* **2019**, *44*, 4253–4262. [[CrossRef](#)]
382. Wahab, M.A.; Jia, Y.; Yang, D.J.; Zhao, H.J.; Yao, X.D. Enhanced hydrogen desorption from $\text{Mg}(\text{BH}_4)_2$ by combining nanoconfinement and a Ni catalyst. *J. Mater. Chem. A* **2013**, *1*, 3471–3478. [[CrossRef](#)]
383. Nale, A.; Catti, M.; Bardají, E.G.; Fichtner, M. On the decomposition of the 0.6LiBH₄-0.4Mg(BH₄)₂ eutectic mixture for hydrogen storage. *Int. J. Hydrog. Energy* **2011**, *36*, 13676–13682. [[CrossRef](#)]
384. Zhao-Karger, Z.; Witter, R.; Bardají, E.G.; Wang, D.; Cossement, D.; Fichtner, M. Altered reaction pathways of eutectic LiBH₄-Mg(BH₄)₂ by nanoconfinement. *J. Mater. Chem. A* **2013**, *1*, 3379. [[CrossRef](#)]
385. Kim, Y.; Reed, D.; Lee, Y.S.; Lee, J.Y.; Shim, J.H.; Book, D.; Cho, Y.W. Identification of the dehydrogenated product of Ca(BH₄)₂. *J. Phys. Chem. C* **2009**, *113*, 5865–5871. [[CrossRef](#)]
386. Ampoumogli, A.; Charalambopoulou, G.; Javadian, P.; Richter, B.; Jensen, T.R.; Steriotis, T. Hydrogen desorption and cycling properties of composites based on mesoporous carbons and a LiBH₄-Ca(BH₄)₂ eutectic mixture. *J. Alloys Compd.* **2015**, *645*, S480–S484. [[CrossRef](#)]
387. Javadian, P.; GharibDoust, S.P.; Li, H.-W.; Sheppard, D.A.; Buckley, C.E.; Jensen, T.R. Reversibility of LiBH₄ facilitated by the LiBH₄-Ca(BH₄)₂ eutectic. *J. Phys. Chem. C* **2017**, *121*, 18439–18449. [[CrossRef](#)]
388. Shannon, R.D. Revised effective ionic-radii and systematic studies of interatomic distances in halides and chalcogenides. *Acta Crystallogr. Sect. A* **1976**, *32*, 751–767. [[CrossRef](#)]
389. Wall, F. Rare earth elements. In *Critical Metals Handbook*; John Wiley & Sons: Hoboken, NJ, USA, 2014; pp. 312–339. [[CrossRef](#)]
390. Frommen, C.; Sørby, M.; Heere, M.; Humphries, T.; Olsen, J.; Hauback, B. Rare earth borohydrides—Crystal structures and thermal properties. *Energies* **2017**, *10*, 2115. [[CrossRef](#)]
391. Olsen, J.E.; Frommen, C.; Jensen, T.R.; Riktor, M.D.; Sørby, M.H.; Hauback, B.C. Structure and thermal properties of composites with RE-borohydrides (RE = La, Ce, Pr, Nd, Sm, Eu, Gd, Tb, Er, Yb or Lu) and LiBH₄. *RSC Adv.* **2014**, *4*, 1570–1582. [[CrossRef](#)]
392. Olsen, J.E.; Frommen, C.; Sørby, M.H.; Hauback, B.C. Crystal structures and properties of solvent-free LiYb(BH₄)₄-xCl_x, Yb(BH₄)₃ and Yb(BH₄)₂-xCl_x. *RSC Adv.* **2013**, *3*, 10764–10774. [[CrossRef](#)]
393. Frommen, C.; Heere, M.; Riktor, M.D.; Sørby, M.H.; Hauback, B.C. Hydrogen storage properties of rare earth (RE) borohydrides (RE = La, Er) in composite mixtures with LiBH₄ and LiH. *J. Alloys Compd.* **2015**, *645*, S155–S159. [[CrossRef](#)]
394. Ley, M.B.; Ravnsbæk, D.B.; Filinchuk, Y.; Lee, Y.-S.; Janot, R.; Cho, Y.W.; Skibsted, J.; Jensen, T.R. LiCe(BH₄)₃Cl, a new lithium-ion conductor and hydrogen storage material with isolated tetranuclear anionic clusters. *Chem. Mater.* **2012**, *24*, 1654–1663. [[CrossRef](#)]
395. Sato, T.; Miwa, K.; Nakamori, Y.; Ohoyama, K.; Li, H.-W.; Noritake, T.; Aoki, M.; Towata, S.-I.; Orimo, S.-I. Experimental and computational studies on solvent-free rare-earth metal borohydrides R(BH₄)₃ (R = Y, Dy, and Gd). *Phys. Rev. B* **2008**, *77*, 104–114. [[CrossRef](#)]
396. Ravnsbæk, D.B.; Filinchuk, Y.; Černý, R.; Ley, M.B.; Haase, D.R.; Jakobsen, H.J.; Skibsted, J.; Jensen, T.R. Thermal polymorphism and decomposition of Y(BH₄)₃. *Inorg. Chem.* **2010**, *49*, 3801–3809. [[CrossRef](#)] [[PubMed](#)]
397. Frommen, C.; Aliouane, N.; Deledda, S.; Fonnelop, J.E.; Grove, H.; Lieutenant, K.; Llamas-Jansa, I.; Sartori, S.; Sørby, M.H.; Hauback, B.C. Crystal structure, polymorphism, and thermal properties of yttrium borohydride Y(BH₄)₃. *J. Alloys Compd.* **2010**, *496*, 710–716. [[CrossRef](#)]
398. Ley, M.B.; Paskevicius, M.; Schouwink, P.; Richter, B.; Sheppard, D.A.; Buckley, C.E.; Jensen, T.R. Novel solvates M(BH₄)₃S(CH₃)₂ and properties of halide-free M(BH₄)₃ (M = Y or Gd). *Dalton Trans.* **2014**, *43*, 13333–13342. [[CrossRef](#)] [[PubMed](#)]
399. Humphries, T.D.; Ley, M.B.; Frommen, C.; Munroe, K.T.; Jensen, T.R.; Hauback, B.C. Crystal structure and in situ decomposition of Eu(BH₄)₂ and Sm(BH₄)₂. *J. Mater. Chem. A* **2015**, *3*, 691–698. [[CrossRef](#)]
400. Ley, M.B.; Jørgensen, M.; Cerny, R.; Filinchuk, Y.; Jensen, T.R. From M(BH₄)₃ (M = La, Ce) borohydride frameworks to controllable synthesis of porous hydrides and ion conductors. *Inorg. Chem.* **2016**, *55*, 9748–9756. [[CrossRef](#)]

401. GharibDoust, S.P.; Ravnsbæk, D.B.; Černý, R.; Jensen, T.R. Synthesis, structure and properties of bimetallic sodium rare-earth (RE) borohydrides, $\text{NaRE}(\text{BH}_4)_4$, RE = Ce, Pr, Er or Gd. *Dalton Trans.* **2017**, *46*, 13421–13431. [[CrossRef](#)]
402. Sharma, M.; Didelot, E.; Spyratou, A.; Lawson Daku, L.M.; Cerny, R.; Hagemann, H. Halide free $\text{M}(\text{BH}_4)_2$ (M = Sr, Ba, and Eu) synthesis, structure, and decomposition. *Inorg. Chem.* **2016**, *55*, 7090–7097. [[CrossRef](#)]
403. Wegner, W.; Jaron, T.; Grochala, W. Polymorphism and hydrogen discharge from holmium borohydride, $\text{Ho}(\text{BH}_4)_3$, and $\text{KHo}(\text{BH}_4)_4$. *Int. J. Hydrog. Energy* **2014**, *39*, 20024–20030. [[CrossRef](#)]
404. Grinderslev, J.B.; Moller, K.T.; Bremholm, M.; Jensen, T.R. Trends in synthesis, crystal structure, and thermal and magnetic properties of rare-earth metal borohydrides. *Inorg. Chem.* **2019**, *58*, 5503–5517. [[CrossRef](#)]
405. Richter, B.; Grinderslev, J.B.; Moller, K.T.; Paskevicius, M.; Jensen, T.R. From metal hydrides to metal borohydrides. *Inorg. Chem.* **2018**, *57*, 10768–10780. [[CrossRef](#)] [[PubMed](#)]
406. Heere, M.; Payandeh Gharib Doust, S.H.; Frommen, C.; Humphries, T.D.; Ley, M.B.; Sorby, M.H.; Jensen, T.R.; Hauback, B.C. The influence of LiH on the rehydrogenation behavior of halide free rare earth (RE) borohydrides (RE = Pr, Er). *Phys. Chem. Chem. Phys.* **2016**, *18*, 24387–24395. [[CrossRef](#)] [[PubMed](#)]
407. Wegner, W.; Jaron, T.; Grochala, W. Preparation of a series of lanthanide borohydrides and their thermal decomposition to refractory lanthanide borides. *J. Alloys Compd.* **2018**, *744*, 57–63. [[CrossRef](#)]
408. Payandeh GharibDoust, S.; Heere, M.; Nervi, C.; Sorby, M.H.; Hauback, B.C.; Jensen, T.R. Synthesis, structure, and polymorphic transitions of praseodymium(iii) and neodymium(iii) borohydride, $\text{Pr}(\text{BH}_4)_3$ and $\text{Nd}(\text{BH}_4)_3$. *Dalton Trans.* **2018**, *47*, 8307–8319. [[CrossRef](#)] [[PubMed](#)]
409. West, A.R. *Solid State Chemistry and Its Applications*; John Wiley & Sons: Hoboken, NJ, USA, 2014.
410. Cerny, R.; Schouwink, P. The crystal chemistry of inorganic metal borohydrides and their relation to metal oxides. *Acta Crystallogr. Sect. B Struct. Sci. Cryst. Eng. Mater.* **2015**, *71*, 619–640. [[CrossRef](#)]
411. GharibDoust, S.P.; Brighi, M.; Sadikin, Y.; Ravnsbæk, D.B.; Černý, R.; Jensen, T.; Skibsted, J. Synthesis, structure and Li Ion conductivity of $\text{LiLa}(\text{BH}_4)_3\text{X}$, X = Cl, Br, I. *J. Phys. Chem. C* **2017**, *121*, 19010–19021.
412. GharibDoust, S.P.; Heere, M.; Sorby, M.H.; Ley, M.B.; Ravnsbaek, D.B.; Hauback, B.C.; Cerny, R.; Jensen, T.R. Synthesis, structure and properties of new bimetallic sodium and potassium lanthanum borohydrides. *Dalton Trans.* **2016**, *45*, 19002–19011. [[CrossRef](#)]
413. Lee, Y.-S.; Ley, M.B.; Jensen, T.R.; Cho, Y.W. Lithium ion disorder and conduction mechanism in $\text{LiCe}(\text{BH}_4)_3\text{Cl}$. *J. Phys. Chem. C* **2016**, *120*, 19035–19042. [[CrossRef](#)]
414. Brighi, M.; Schouwink, P.; Sadikin, Y.; Cerny, R. Fast ion conduction in garnet-type metal borohydrides $\text{Li}_3\text{K}_3\text{Ce}_2(\text{BH}_4)_{12}$ and $\text{Li}_3\text{K}_3\text{La}_2(\text{BH}_4)_{12}$. *J. Alloys Compd.* **2016**, *662*, 388–395. [[CrossRef](#)]
415. Schouwink, P.; Ley, M.B.; Tissot, A.; Hagemann, H.; Jensen, T.R.; Smrcok, L.; Cerny, R. Structure and properties of complex hydride perovskite materials. *Nat. Commun.* **2014**, *5*, 5706. [[CrossRef](#)]
416. Møller, K.T.; Jørgensen, M.; Fogh, A.S.; Jensen, T.R. Perovskite alkali metal samarium borohydrides: Crystal structures and thermal decomposition. *Dalton Trans.* **2017**, *46*, 11905–11912. [[CrossRef](#)] [[PubMed](#)]
417. Schouwink, P.; Didelot, E.; Lee, Y.S.; Mazet, T.; Cerny, R. Structural and magnetocaloric properties of novel gadolinium borohydrides. *J. Alloys Compd.* **2016**, *664*, 378–384. [[CrossRef](#)]
418. Roedern, E.; Lee, Y.-S.; Ley, M.B.; Park, K.; Cho, Y.W.; Skibsted, J.; Jensen, T.R. Solid state synthesis, structural characterization and ionic conductivity of bimetallic alkali-metal yttrium borohydrides $\text{MY}(\text{BH}_4)_4$ (M = Li and Na). *J. Mater. Chem. A* **2016**, *4*, 8793–8802. [[CrossRef](#)]
419. Jaron, T.; Wegner, W.; Fijalkowski, K.J.; Leszczynski, P.J.; Grochala, W. Facile formation of thermodynamically unstable novel borohydride materials by a wet chemistry route. *Chem. A Eur. J.* **2015**, *21*, 5689–5692. [[CrossRef](#)]
420. Ravnsbæk, D.B.; Ley, M.B.; Lee, Y.-S.; Hagemann, H.; D’Anna, V.; Cho, Y.W.; Filinchuk, Y.; Jensen, T.R. A mixed-cation mixed-anion borohydride $\text{NaY}(\text{BH}_4)_2\text{Cl}_2$. *Int. J. Hydrog. Energy* **2012**, *37*, 8428–8438. [[CrossRef](#)]
421. Jaroń, T.; Grochala, W. Probing Lewis acidity of $\text{Y}(\text{BH}_4)_3$ via its reactions with MB_4 (M = Li, Na, K, NMe_4). *Dalton Trans.* **2011**, *40*, 12808–12817. [[CrossRef](#)]
422. Sadikin, Y.; Stare, K.; Schouwink, P.; Ley, M.B.; Jensen, T.R.; Meden, A.; Černý, R. Alkali metal-yttrium borohydrides: The link between coordination of small and large rare-earth. *J. Solid State Chem.* **2015**, *225*, 231–239. [[CrossRef](#)]
423. Jaroń, T.; Wegner, W.; Grochala, W. $\text{M}[\text{Y}(\text{BH}_4)_4]$ and $\text{M}_2\text{Li}[\text{Y}(\text{BH}_4)_{6-x}\text{Cl}_x]$ (M = Rb, Cs): New borohydride derivatives of yttrium and their hydrogen storage properties. *Dalton Trans.* **2013**, *42*, 6886–6893. [[CrossRef](#)]

424. Heere, M.; GharibDoust, S.P.; Sorby, M.H.; Frommen, C.; Jensen, T.R.; Hauback, B.C. In situ investigations of bimetallic potassium erbium borohydride. *Int. J. Hydrog. Energy* **2017**, *42*, 22468–22474. [[CrossRef](#)]
425. Wegner, W.; Jaron, T.; Grochala, W. MYb(BH₄)₄ (M = K, Na) from laboratory X-ray powder data. *Acta Cryst. C* **2013**, *69*, 1289–1291. [[CrossRef](#)]
426. Gennari, F.C. Mechanochemical synthesis of erbium borohydride: Polymorphism, thermal decomposition and hydrogen storage. *J. Alloys Compd.* **2013**, *581*, 192–195. [[CrossRef](#)]
427. Heere, M.; GharibDoust, S.P.; Brighi, M.; Frommen, C.; Sørby, M.; Černý, R.; Jensen, T.; Hauback, B. Hydrogen sorption in erbium borohydride composite mixtures with LiBH₄ and/or LiH. *Inorganics* **2017**, *5*, 31. [[CrossRef](#)]
428. Thangadurai, V.; Kaack, H.; Weppner, W.J.F. Novel fast lithium ion conduction in Garnet-type Li₅La₃M₂O₁₂ (M = Nb, Ta). *J. Am. Ceram. Soc.* **2003**, *86*, 437–440. [[CrossRef](#)]
429. Marks, S.; Heck, J.G.; Habicht, M.H.; Ona-Burgos, P.; Feldmann, C.; Roesky, P.W. [Ln(BH₄)₂(THF)₂] (Ln = Eu, Yb)—A highly luminescent material. Synthesis, properties, reactivity, and NMR studies. *J. Am. Chem. Soc.* **2012**, *134*, 16983–16986. [[CrossRef](#)]
430. Wegner, W.; van Leusen, J.; Majewski, J.; Grochala, W.; Kogerler, P. Borohydride as magnetic superexchange pathway in late lanthanide borohydrides. *Eur. J. Inorg. Chem.* **2019**, *2019*, 1776–1783. [[CrossRef](#)]
431. Payandeh, S.; Asakura, R.; Avramidou, P.; Rentsch, D.; Łodziana, Z.; Černý, R.; Remhof, A.; Battaglia, C. Nido-Borate/Closo-Borate mixed-anion electrolytes for all-solid-state batteries. *Chem. Mater.* **2020**. [[CrossRef](#)]
432. Roedern, E.; Kuhnel, R.S.; Remhof, A.; Battaglia, C. Magnesium ethylenediamine borohydride as solid-state electrolyte for magnesium batteries. *Sci. Rep.* **2017**, *7*, 46189. [[CrossRef](#)]
433. Burankova, T.; Roedern, E.; Maniadaki, A.E.; Hagemann, H.; Rentsch, D.; Łodziana, Z.; Battaglia, C.; Remhof, A.; Embs, J.P. Dynamics of the coordination complexes in a solid-state mg electrolyte. *J. Phys. Chem. Lett.* **2018**, *9*, 6450–6455. [[CrossRef](#)]
434. Le Ruyet, R.; Berthelot, R.; Salager, E.; Florian, P.; Fleutot, B.; Janot, R. Investigation of Mg(BH₄)(NH₂)-based composite materials with enhanced Mg₂₊ ionic conductivity. *J. Phys. Chem. C* **2019**, *123*, 10756–10763. [[CrossRef](#)]



© 2020 by the authors. Licensee MDPI, Basel, Switzerland. This article is an open access article distributed under the terms and conditions of the Creative Commons Attribution (CC BY) license (<http://creativecommons.org/licenses/by/4.0/>).